Space Science Reviews (2023) 219:20
https://doi.org/10.1007/s11214-023-00964-0

SPECIAL COMMUNICATION

Results from InSight Robotic Arm Activities

M. Golombek[1] · T. Hudson[1] · P. Bailey[1] · N. Balabanska[1] · E. Marteau[1] · C. Charalambous[2] · M. Baker[3] · M. Lemmon[4] · B. White[5] · R.D. Lorenz[6] · T. Spohn[7,8] · J. Maki[1] · P. Kallemeyn[5] · J.B. Garvin[9] · C. Newman[10] · K. Hurst[1] · N. Murdoch[11] · N. Williams[1] · W.B. Banerdt[1] · P. Lognonné[12] · P. Delage[13] · R. Lapeyre[14] · E. Gaudin[14] · C. Yana[14] · N. Verdier[14] · M. Panning[1] · A. Trebi-Ollennu[1] · K. Ali[1] · A. Mittelholz[15] · C. Johnson[16,17] · B. Langlais[18] · N. Warner[19] · J. Grant[3] · I.J. Daubar[20] · V. Ansan[18] · C. Vrettos[21] · A. Spiga[22] · D. Banfield[23] · A. Gomez[24] · P. Mishra[1] · R. Dotson[25] · C. Krause[26] · G. Sainton[11] · T. Gabsi[11]

Received: 14 September 2022 / Accepted: 1 March 2023 / Published online: 20 March 2023

Abstract
The InSight lander carried an Instrument Deployment System (IDS) that included an Instrument Deployment Arm (IDA), scoop, five finger "claw" grapple, forearm-mounted Instrument Deployment Camera (IDC) requiring arm motion to image a target, and lander-mounted Instrument Context Camera (ICC), designed to image the workspace, and to place the instruments onto the surface. As originally proposed, the IDS included a previously built arm and flight spare black and white cameras and had no science objectives or requirements, or expectation to be used after instrument deployment (90 sols). During project development the detectors were upgraded to color, and it was recognized that the arm could be used to carry out a wide variety of activities that would enable both geology and physical properties investigations. During surface operations for two martian years, the IDA was used during major campaigns to image the surface around the lander, to deploy the instruments, to assist the mole in penetrating beneath the surface, to bury a portion of the seismometer tether, to clean dust from the solar arrays to increase power, and to conduct a surface geology investigation including soil mechanics and physical properties experiments. No other surface mission has engaged in such a sustained and varied campaign of arm and scoop activities directed at such a diverse suite of objectives. Images close to the surface and continuous meteorology measurements provided important constraints on the threshold friction wind speed needed to initiate aeolian saltation and surface creep. The IDA was used extensively for almost 22 months to assist the mole in penetrating into the subsurface. Soil was scraped into piles and dumped onto the seismometer tether six times in an attempt to bury

This is a Special Communication linked to the topical collection on the Insight mission published in Space Science Reviews. In addition to invited review papers and topical collections, Space Science Reviews publishes unsolicited Special Communications. These are papers linked to an earlier topical volume/collection, report-type papers, or timely papers dealing with a strong space-science-technology combination (such papers summarize the science and technology of an instrument or mission in one paper).

Extended author information available on the last page of the article

the tether and ∼ 30% was entrained in the wind and dispersed downwind 1-2 m, darkening the surface. Seven solar array cleaning experiments were conducted by dumping scoops of soil from 35 cm above the lander deck during periods of high wind that dispersed the sand onto the panels that kicked dust off of the panels into suspension in the atmosphere, thereby increasing the power by ∼15% during this period. Final IDA activities included an indentation experiment that used the IDA scoop to push on the ground to measure the plastic deformation of the soil that complemented soil mechanics measurements from scoop interactions with the surface, and two experiments in which SEIS measured the tilt from the arm pressing on the ground to derive near surface elastic properties.

Keywords Mars · Arm activities · InSight mission · Soil mechanics · Geology · Eolian activity

1 Introduction

The InSight (Interior Exploration using Seismic Investigations, Geodesy and Heat Transport) mission was a NASA Discovery Program mission to investigate the internal structure of Mars and the differentiation of the terrestrial planets (Banerdt et al. 2020). The spacecraft carried a seismometer (Seismic Experiment for Interior Structure, SEIS, Lognonné et al. 2019), heat flow probe (Heat Flow and Physical Properties Package, HP^3, Spohn et al. 2018) and a precision tracking system (Rotation and Interior Structure Experiment, RISE, Folkner et al. 2018) to measure the size and state of the core, mantle and crust (Fig. 1). After landing in November 2018, the lander operated on the surface for about four Earth years (about two Mars years or 1442 sols) recording marsquakes and impacts and tracking the precession and nutation of the spin axis. The spacecraft also carried a meteorology package, a magnetometer, and an Instrument Deployment System (IDS) that included an Instrument Deployment Arm (IDA), scoop, five finger "claw" grapple, arm-mounted Instrument Deployment Camera (IDC), lander-mounted Instrument Context Camera (ICC), motor controller and control software (Trebi-Ollennu et al. 2018).

At conception, the InSight Instrument Deployment Arm (IDA, Trebi-Ollennu et al. 2018) was to be an arm from the Mars Surveyor 2001 Lander mission (Bonitz et al. 2000) that was not flown and the IDC and ICC would be spare Navigation and Hazard black and white engineering cameras from the Mars Science Laboratory (MSL) mission. In the original Discovery mission proposal to NASA (September 2010), the function of the IDS was to simply deploy the instruments and the cameras were to image the surface to aid in their deployment. This resulted in a requirement to last for at least 100 sols, which was the time allotted for deployment (Trebi-Ollennu et al. 2018). There was little expectation that the arm or the IDC would be used after instrument deployment. Any science that could be conducted with the cameras was considered ancillary science that would not interfere with the main science requirements or objectives of the mission and there were no science requirements associated with the IDS (beyond deploying the instruments). During the phase A study, a preliminary analysis of the project design and plan was completed. The resulting Concept Study Report that was submitted to NASA as the step 2 proposal included a surface geology investigation to use surface images to characterize the geology of the landing site and relate it to orbital remote sensing data used primarily to select the landing site (e.g., Golombek et al. 2017).

After InSight was selected as a Discovery project (August 2012, the start of phase B) and the process for selecting locations to place the instruments on the surface was better understood, it was recognized that identifying different surface materials on the surface of Mars

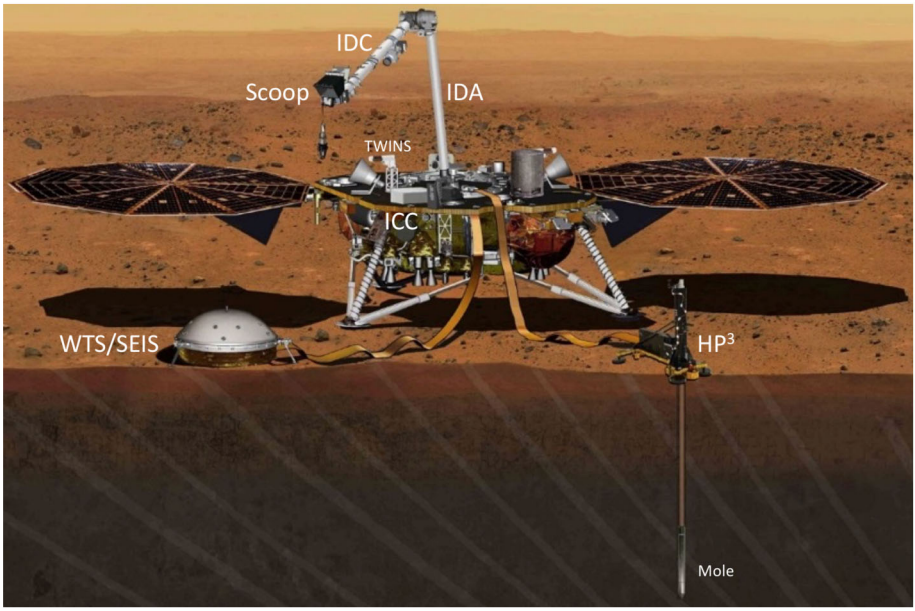

Fig. 1 Artist's perspective view of the InSight lander looking north showing the instruments and the arm (IDA) labeled. The IDA is mounted on the southwestern edge of the lander deck and is shown with the grapple hanging below the arm. The ICC is mounted on the lander beneath the deck oriented to look at the deployment workspace to the south. The SEIS/WTS and HP^3 and mole are deployed in the workspace with tethers extending to the lander. The western TWINS boom for measuring wind speed and direction is labeled. The lander controlled its azimuth during landing so the workspace and instruments are to the south

would be vastly improved with color images. There was also concern that InSight would be the first lander on Mars without color cameras, and black and white images after landing could negatively affect public perception of the Mars exploration program and NASA. In June 2014, additional resources were made available by NASA to replace the single-channel greyscale detectors on the IDC and ICC with red/green/blue (RGB) Bayer-pattern color versions (Maki et al. 2018). It was also recognized that measuring the atmospheric opacity could be done with the IDC and that this was important for managing spacecraft power and monitoring the performance of the solar panels (Sect. 3.2). In addition, testing showed that the IDC color camera could obtain a complete color panorama of the surroundings, including the spacecraft, which would be important for public relations and outreach. Because of the importance of these two measurements, both were elevated to project requirements.

It was also recognized during project development that the arm could perform a variety of other activities that would enable a more robust geology investigation, study near surface physical properties and surface-atmosphere aeolian interactions as described in Golombek et al. (2018a). However, there was no expectation that any of them would be done as these investigations remained ancillary to the main objectives of the mission and were designated as goals (and not requirements). Activities enabled by the arm and scoop included investigating soil mechanics and determining physical and elastic properties of near surface materials via scraping, indentation, scooping and piling experiments.

During the design and development phase (phase C) of the mission, the IDA was modified to better deploy the instruments. These modifications included replacing the composite arm tubes with titanium to better carry the load of the instruments, shortening the upper

arm by 25 mm to avoid interference with the SEIS tether, and minor changes to cables and motors. Although the inherited arm included a scoop at the end, it had no defined function for the InSight mission. Nevertheless, it was left on the arm as insurance against potentially unforeseen circumstances that might require direct interaction with the surface. Testing during this phase also revealed a flaw in the design of the joint motor armatures that resulted in potential wire breakage at low temperatures (≤ -70 °C). As budget and schedule would not allow new motors to be built, it was decided to use electric heaters on the joint motors to keep them above -60 °C on Mars through the end of deployment operations. However, this would require significant amounts of energy, and could not be continued indefinitely without affecting the operation of other instruments, as dust on the solar panels was expected to progressively reduce available energy during the mission. Thus, the survival of the IDA could not be guaranteed after the first 100 sols allocated to deploy the instruments.

The events and information obtained during surface operations (e.g., Banerdt et al. 2020) resulted in the IDA accomplishing almost all of the additional activities described above, including major campaigns to assist the mole in penetrating beneath the surface (Spohn et al. 2022a,b), to bury a portion of the seismometer tether, to clean dust from the solar arrays to increase power, and to conduct soil mechanics and physical properties experiments. Although other surface missions have used arms with scoops to scrape, pile and scoop near-surface materials (e.g., Moore et al. 1987; Arvidson et al. 2009), no other Mars surface mission has engaged in such a sustained and varied campaign of arm and scoop activities directed at such a diverse suite of objectives.

The intent of this paper is to document and provide an overview of arm activities and results accomplished by the IDA, which will be important for future space missions that plan to conduct experiments on and with planetary soils and regolith. The paper begins with a short description of the Instrument Deployment System (IDS) (Sect. 2), including the cameras and robotic arm, and then discusses the major imaging campaigns completed by the lander (Sect. 3). This is followed by the instrument site selection and deployment operations (Sects. 4 and 5) and a review of the geology investigation enabled by the imaging (Sect. 6). A summary of how the IDA helped with HP^3 mole recovery operations to assist the mole to penetrate beneath the surface is provided in Sect. 7. This is followed in Sect. 8 by a description of how repeat high-resolution IDC images documented motion of fine-grained materials that, along with measured local meteorology during wind vortices, constrained the threshold friction wind speed needed to move particles by the wind. Section 9 describes how the arm was used to scrape, scoop and dump soil onto a portion of the SEIS tether in an attempt to reduce instrument noise. During these soil dumps, it was observed that soil was entrained and dispersed in a downwind direction. Solar array cleaning experiments are described in Sect. 10, in which soil was dumped adjacent to the solar panels to disperse wind-blown sand onto the solar panels to reduce the dust cover and improve the energy generated. The last IDA activities possible near the end of the mission, before reduced power disallowed arm movement, including physical and elastic properties experiments, are described in Sect. 11. Finally, calibration of the arm was conducted in the JPL testbed to better determine forces imparted on the soil during IDA interactions with the surface from motor currents (Sect. 12).

2 IDS Design and Operations

The Instrument Deployment System (IDS) refers to the subsystem of the lander used in the instrument deployment activity, and consists of a four degree-of-freedom robotic arm, scoop, five finger "claw" grapple, motor controller, Instrument Deployment Camera (IDC)

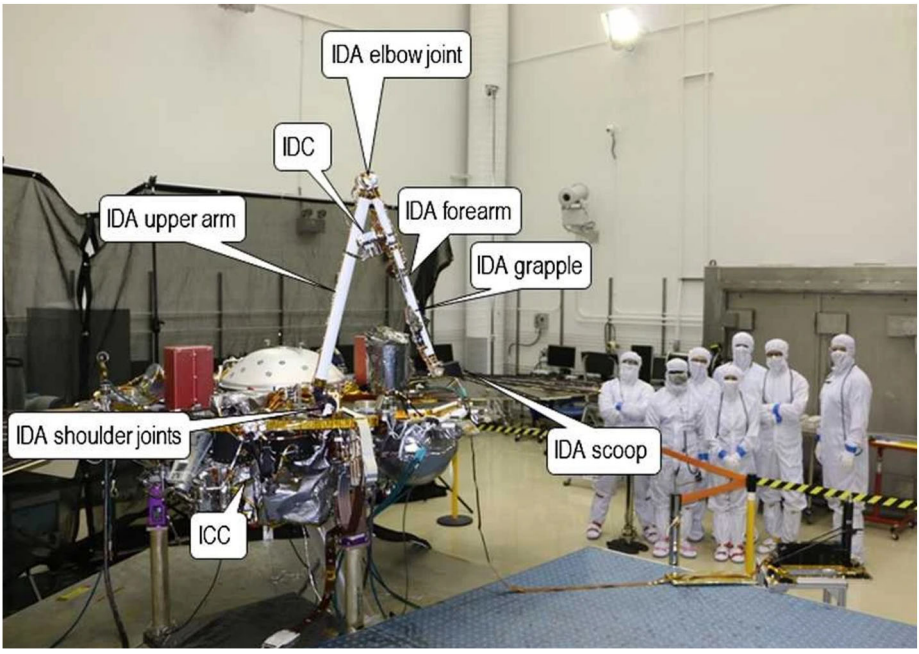

Fig. 2 Labeled elements of the IDS on the InSight lander before launch, Note the HP^3 to the right, the SEIS tether and white field joint on ground to the left and the white dome-shaped WTS on the lander deck. The IDA is mounted to the lander deck at the shoulder joint which provides azimuthal and elevation motion. The elbow and wrist each provide one degree of freedom motion. The IDC is mounted near the IDA elbow and looks down the arm towards the scoop attached to the IDA forearm. The grapple used to pick up the instruments is shown stowed (against the arm). Most science imaging occurred with the grapple in the stowed configuration, mostly out of the field of view of the IDC

attached to the forearm of the robotic arm, Instrument Context Camera (ICC) mounted on the lander, and control software (Trebi-Ollennu et al. 2018). Figure 2 shows a labeled view of the IDS components on the Insight lander.

The IDA is a four degree-of-freedom robotic arm, refurbished from the Mars Surveyor Lander mission (Bonitz et al. 2000), with titanium links and shoulder azimuth, shoulder elevation, elbow, and wrist joints (joints 1 through 4 respectively). It has a reach of 1.8 meters and can lift a 9 kg (33 N) payload at a distance of 1.65 m on Mars (Trebi-Ollennu et al. 2020). Each joint is actuated by a brushed DC motor, and contains an encoder at the joint input shaft, a potentiometer at the joint output load shaft, and two mechanical hardstops, as well as a dust seal to prevent motor and gearbox contamination (Trebi-Ollennu et al. 2018). In addition, each joint has a temperature sensor and heater and the IDA is designed to withstand expected environmental temperatures from $-110°$ to $+70$ °C, in a CO_2 atmosphere, with pressure as low as 667 Pa, except for the motors, which were limited to the range -60 °C to $+70$ °C. For the first 550 sols of the mission there was sufficient power to enable the arm heaters to keep the joint motors above -60 °C at night. The IDA was still being used for mole recovery (Sect. 7) at that time and there was concern that the motors might not survive the nighttime cold or be available for other activities. After sol 550, the joint motors were no longer heated at night and experienced much colder temperatures (> -90 °C) (Banfield et al. 2020). Even so, there was no observed degradation of the arm or impediment to IDA operations through the rest of the mission ($\sim$1442 sols).

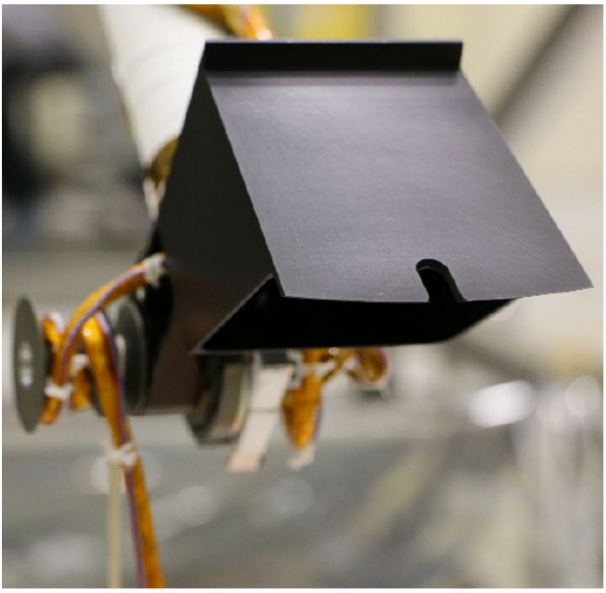

Fig. 3 The scoop at the end of the IDA. Note the blade on the tip of the scope with semicircle cut out and the second blade on the bottom. The width of the scoop is 7.5 cm and it holds a volume of 250 cm^3. Note attachment to the wrist joint, which provides one degree of freedom motion

Joints 1 through 4 can generate 35, 120, 65, and 10.5 N-m of torque respectively, and the IDA end effector exerts an average force of about 80 N (Trebi-Ollenu et al. 2020) in the z-direction when pressing on the ground. Joint encoders provide less noisy and more accurate relative readings, whereas the resolvers provide a more accurate absolute joint angle value estimate (Bailey et al. 2020). The IDA positioning accuracy requirement is close to 1 cm (Bailey et al. 2020). Because the IDA actuators were not designed to hold a heavy load in an outstretched pose while not powered, the possibility of the IDA actuators backdriving under a heavy load such as the 9.5 kg WTS once the actuators are powered off in between motions was considered during instrument deployment (Trebi-Ollennu et al. 2020). The IDA also experienced some deflection in the links under its own weight and the weight of a payload (Bailey et al. 2020), which is computed and compensated for by flight software (Ali 2021).

On the end of the IDA is the IDA end-effector, which contains a five finger "claw" grapple and a scoop (Fig. 3). The grapple is used to deploy instruments by grasping and lifting up instruments from the lander's deck and placing them onto the martian surface. The five fingers of the grapple are opened by a single high output paraffin (HOP) actuator, such that power must only be applied to open the fingers, and closing the fingers happens passively by cooling in the ambient temperature (Trebi-Ollennu et al. 2020). The grapple hangs on an umbilical cable from the IDA and can be placed in a stowed or unstowed configuration. When the grapple is unstowed, it hangs freely in the IDC field of view, allowing imaging of the grappled instruments (but obscuring everything beyond it). When the grapple is in a stowed configuration, it is held in place against the IDA forearm and out of the IDC field of view (Sorice et al. 2021) by closing the grapple fingers around a restraint ball located on the IDA forearm (Imken et al. 2020). After instrument deployment activities were completed, the grapple was placed in a stowed configuration for the remainder of the mission, during IDS activities such as the HP^3 mole recovery operations, SEIS tether burial, and solar array cleaning.

The scoop is attached at the end of the IDA (Fig. 3) and contains a chamber created by the four panels of the scoop in which soil can be scooped, and two blades on the sides of the

chamber, one on the front tip and a second at the bottom (Imken et al. 2020). The longest, bottom panel of the scoop is approximately 7.5 cm wide across the bottom blade and 10 cm long, and the scoop chamber can be roughly characterized as a box with dimensions 7.5 cm $\times$ 5 cm $\times$ 4.5 cm, attached to a half of a box of the same size, giving the chamber a volume of 250 cm^3. The scoop can be used for scraping, tamping, and scooping soil into the scoop chamber, allowing the IDA to carry soil acquired from the martian surface and move it in the arm workspace (Trebi-Ollennu et al. 2018).

Two color cameras, the arm-mounted IDC and lander-mounted ICC, are included in the IDS. Both cameras are spare engineering cameras (Navcam and Hazcam) from the Mars Science Laboratory (MSL) mission (Maki et al. 2012), which were upgraded from grayscale to color (Maki et al. 2018). Red, green, and blue bandpasses for both cameras are centered at approximately 450, 550, and 620 nm, respectively, to enable distinguishing gray basaltic material from reddish dust (Golombek et al. 2018a; Maki et al. 1999). The IDC is a 1 megapixel camera mounted near the elbow of the IDA and has a field of view (FOV) of 45° $\times$ 45° and an instantaneous FOV (IFOV) of 0.82 mrad/pixel, while the ICC is mounted on the underside of the lander deck and has a field of view of the workspace of 124° $\times$ 124° and an IFOV of 2.1 mrad/pixel (Maki et al. 2018). The IDC must be relatively close to the imaging target to obtain pixel resolutions of $\sim$1 mm (Bailey et al. 2020) and can be moved to imaging locations through IDA motion. The IDC can be used to capture stereo frames by moving the shoulder joint of the IDA a specified offset between images (Maki et al. 2019; Bailey et al. 2020), thus using only a single camera to produce stereo image pairs, which are processed into products that enable localization in the workspace (Maki et al. 2018; Abarca et al. 2019). In addition to localization with stereo, IDC images were also used for the fiducial localization during instrument deployment (Bailey et al. 2020, Sect. 5.7). While the ICC was not used in instrument localization as it has a fish-eye lens (Bailey et al. 2020), it has played a role in atmospheric observations and context gathering.

Additional IDS hardware components include the IDA motor controller (MC). The MC provides low-level motor control and interfaces with the IDA flight software (FSW) on the lander Command and Data Handling computer (Trebi-Ollennu et al. 2020). The IDA FSW interfaces with the MC to provide motion control, fault sensing and recovery, collision prevention, and IDA state telemetry, and allows ground operators to command the IDA using high-level commands (Ali 2021). IDS activities are specified by sequences of commands, which can be single motions or more complicated tasks such as motor calibrations. Sequences are developed by IDS ground operators and uplinked for each tactical plan involving IDS activities. IDA motion can be commanded by specifying a goal position in terms of relative or absolute joint angles or Cartesian coordinates, or a direction and duration of motion for the specified motors (Trebi-Ollennu et al. 2018).

The IDA motion commands provide an optional guarded motion capability, which allows a move command to execute a motion until contact is made. A guarded motion will not safe the IDA upon detecting an overcurrent or torque event, allowing the IDS to command a motion driving the IDA into the martian surface (Ali 2021). Although the IDA retains blade scraping capabilities using a single command (Trebi-Ollennu et al. 2018) as heritage from the Phoenix lander robotic arm (Bonitz et al. 2008), these commands were not used to interact with the surface in IDS activities. Scrapes, tamps, and scoops were instead performed using sequences of IDA motion commands, utilizing the guarded motion command capability for contact with the surface. IDS sequences for these activities were developed by the IDS uplink team and assessed using simulation, image products, and ground tools, including a mission-specific version of the Robot Sequencing and Visualization Program (RSVP) software tool that provides an interface for assembling sequences of IDA commands and motion simulation (Hartman et al. 2005).

Table 1 Image summary, Sols 0-1442[a]

Total number of IDC images	4089
Total number of ICC images	2594
Total number of all images	6683

[a]sol 1436 is the last sol an image was returned

3 InSight Imaging

IDC and ICC images have supported a large number of mission activities, including terrain reconnaissance, instrument deployment and localization, lander and instrument hardware inspection, atmospheric observations, meteor searches, and general mission operations support. Because the IDC is attached to the forearm of the IDA, all IDC imaging required moving the arm to point the camera at an intended target. Furthermore, the resolution of the images could be varied for targets relatively close to the lander by changing the arm pose to get the camera closer to the target. As an example, images of the workspace acquired during instrument site selection (Sect. 4) were acquired with the arm above and below the deck, which changed the resolution of the mosaics by a factor of ∼4.

Because the arm has single degree of freedom elbow and wrist joints (Trebi-Ollennu et al. 2018), traditional stereo images where the camera field of view could be centered at the same point (so called "toe in") could not be obtained, but instead side-by-side images using rotation of the shoulder joint were used to get stereo (Maki et al. 2019; Abarca et al. 2019). This creates camera pointing uncertainties that had to be corrected using several methods to create tiepoints between the images and a bundle adjustment process. Testing using a full-scale model of the lander and cameras in the JPL testbed (Sect. 5.2) showed that digital elevation models (DEMs) and orthophotos produced met the demanding requirements for instrument site selection (Maki et al. 2019) (Sect. 4). Details of the image and data processing can be found in Abarca et al. 2019).

As of Sol 1436 (the last sol an image was returned), a total of 6,683 InSight IDC and ICC images have been acquired as part of the InSight surface mission (Table 1). Representative IDC image acquisition types are shown in Table 2. The IDC observations listed in Table 2 are grouped into general categories, along with the sol (or sol range) that the images were acquired. Because images were often acquired for multiple purposes, the categories in Table 2 are provided as a representative list only and are not exclusive or exhaustive. ICC images were also acquired throughout the mission for operational context to include views of the robotic arm in various configurations and to acquire regular atmospheric opacity (tau) images (Sect. 3.2). All of the raw IDC and ICC images have been delivered to the NASA Planetary Data System (PDS) archive imaging node (Maki et al. 2022), along with a set of calibrated color images (Maki et al. 2021).

3.1 Panoramas

IDC panoramas of the surface were acquired by moving the robotic arm around the lander to create a 360-degree azimuthal field of regard. These panoramas serve as a main source of data for geologic investigations (Golombek et al. 2018a, 2020a). IDC panoramas were acquired at camera heights ∼1.5 to 2 meters above the surface and have an angular resolution of 0.82 mrad/pixel (Maki et al. 2018; Abarca et al. 2019). Notable panoramas include the first panorama (sol 14), morning and evening panoramas, and the final panorama (sol 1211). Panoramas of the top lander deck were acquired several times, notably on sol 10 (with the instruments on the deck), sols 106 and 133 (without instruments on the deck), sol 578 (showing dust accumulation), and sol 1211 (final deck panorama). Images of the terrain

Table 2 IDC image categories, Sols 0-1442

Observation category	Sols (or sol range)	Notes
Panorama/terrain	10,14,100,107,134,160, 168,1047	Various panorama types, including stereo
Lander Above Deck	12,58,96,106,133,149,584, 578,918,1136,1211,1238	Includes camera calibration target, solar panels
Workspace Imaging	12,16,58,227,230,243	Various panorama types, including stereo
Lander Below Deck	10,14,18,137,1211	Includes footpads
SEIS grapple, deployment, tether adjustment and localization	20-73	Various sols during this period
HP^3 grapple, deploy, tether inspection, localization	74-94	Various sols during this period
HP^3 mole assistance	240-775	Various sols during this period
Sunrise	145,1198	Includes time series
Sunset	101,102,145,1198	Includes time series
Meteor search	126-593	Various sols during this period
Soil Mechanics/Scoop	802-1288	Various sols during this period
Change detection	298-400, 1239-1436	Various sols during these periods

in front of the lander (instrument workspace) were acquired numerous times during the deployment and operation of the SEIS and HP^3 instruments during the initial 90 sols of the mission. Workspace images were generally acquired as stereo pairs, with the stereo baseline generated by rotating the shoulder joint of the IDA to create IDC left/right image and were used during the instrument site selection activity (Maki et al. 2018; Abarca et al. 2019) (Sect. 4). Images of the area below the lander were acquired on several occasions, most notably on sols 14, 18, and 1211. Below deck imaging required careful planning and movement of the robotic arm due to the proximity of the ground and later instruments and tethers near the lander. IDC images of the area below the lander show pits excavated by the lander engines (Golombek et al. 2020a).

A large collection of IDC images from sol ∼20 through sol 94 are related to the deployment of the SEIS and HP^3 instrument onto the surface, including post-deployment documentation and localization of the instrument tether/cables (Sect. 5). Many of the IDC images acquired from sols ∼240 to ∼755 were dedicated to the deployment of the HP^3 mole (Spohn et al. 2022b) (see Sect. 7.2). Soil mechanics experiments were also conducted at different times from sols ∼802 to ∼1288.

3.2 Optical Depth

The aerosol optical depth of the atmosphere was important to the project for both operational and scientific reasons. First, the optical depth strongly modifies the fraction of incoming solar radiation that reaches the surface to power the InSight solar panels. While solar panel output was monitored directly, knowledge of the atmosphere's changing state was used to determine whether changes in power output were related to meteorology or to problems with the solar panels (primarily the increasing dust coating). Second, changes in optical depth signal changes in the atmospheric dust load or in cloudiness, which are useful parameters for interpreting the meteorology (Banfield et al. 2020). Third, optical depth is among the

indicators for seasonally varying atmospheric conditions that affect the level of seismic noise (Knapmeyer et al. 2021).

Unlike prior rovers and landers, which measured optical depth via direct solar imaging that determines atmospheric transmission (e.g., Lemmon et al. 2015), InSight's lack of solar imaging capability required the inference of optical depth from sky images. Wolfe (2016) used contemporaneous sky and solar images from the Mars Exploration Rover *Opportunity* to validate a technique for retrieving optical depth. Sky images were used to determine the radiance profile with angle above the horizon for constant scattering angle from the Sun. Scattering angles from 75-105° were found to be useful when the Sun was 15-35° above the horizon, for optical depths from 0.4-1.7.

InSight originally used IDC images of the sky at southwestern or southern aims (IDC tau) for measuring optical depth in the morning or evening, respectively; but then generally relied on ICC measurements (ICC tau) for most of the mission. During the first 180 sols, the method was adapted for use with ICC images and validated against IDC measurements. The ICC field of view looking south includes the appropriate angles for morning or evening taus in summer or winter; the challenge was to show that the ICC calibration was sufficiently well known, given the alignment of a gradient in its spatial response with the necessary gradient in sky brightness. Validation included both a set of contemporaneous optical depth measurements and an IDC panorama across the ICC FOV while ICC images were taken. ICC measurements were imprecise early in the mission due to the dust coating from landing, but had uncertainties comparable to IDC measurements ($\sigma = 0.08$-0.12) as dust on the ICC optics reached a quasi-steady state. After sol 180, ICC measurements were made every 2-3 sols at times in the morning or afternoon to keep the Sun at the right elevation angle and fit into the plan with other activities.

Tau images were calibrated to radiance and then analyzed to determine optical depth. First, a swath of the sky at near-constant scattering angle was selected; it was verified that no portion of the arm or scoop was within that swath (this was manually checked as well). Discrete ordinates radiative transfer calculations (Stamnes et al. 1988) were used to match the normalized sky brightness gradient, where the normalization removed many effects of dust on the optics. Optical depth results were reported to the lander's engineering team several times a week throughout the mission (e.g., see Sect. 10.1).

Optical depth followed established seasonal patterns but with year-to-year variability due to the timing and location of regional dust storms. Landing occurred at areocentric solar longitude (L_s) ~296°, shortly after local (northern) winter solstice (at $L_s = 270°$), and close to the middle of the 'dusty season' that spans roughly northern fall and winter. The optical depth was initially just below 1, then increased rapidly from about sol 40 ($L_s \sim 320°$) during a large regional dust storm, spiking at ~2 around sol 52 before declining back to seasonal values by around sol 150 (Viúdez-Moreiras et al. 2020). A regional storm at this general time is common on Mars, but varies in size from year to year, with this being a particularly large occurrence. Low optical depths (0.5-0.6) were seen throughout northern spring and summer, $L_s = 0$-$180°$ (Banfield et al. 2020). Clouds commonly appeared in images around northern summer solstice ($L_s = 90°$). Optical depth subsequently increased to ~1.4 with the occurrence of northern fall dust storms. The second Mars year then repeated approximately what was seen in the first, except for weaker mid-winter dust storm activity and a brief regional dust storm that affected InSight at $L_s \sim 150°$, prior to the main dust storm season.

During the first 180 sols, cross-sky imaging surveys were used to measure the sky radiance at a wide range of angles from the Sun for the retrieval of aerosol properties (e.g., Lemmon et al. 2004). The surveys comprised 5 IDC images above the southern horizon. Due to the scattering angles sampled, the constraints on the dust size distribution have been

weak. However, the retrievals from such sequences have been used to validate the optical depth retrieval from the smaller set of angles used in the IDC-tau or ICC-tau measurements. Such surveys were done on sols 122, 128, and 175, and 1157 (Sect. 11.2).

3.3 Dust Devils

With convective vortices detected by meteorology being common at the site (Banfield et al. 2020; Spiga et al. 2021: Lorenz et al. 2021a), images were used to try to find active dust devils (vortices made visible by having lifted dust into them from the surface) or dust devil tracks (darker lines and whirls on the surface, produced by the removal of bright dust; see also Sect. 10.2.2). Dedicated imaging was done with sets of 3 or 6 IDC or ICC images taken near the mid-sol peak of vortex activity about 12 times over sols 23-108. Such sets were compared by differencing and rationing to look for evidence of motion. No active dust devils were detected. Further, no active dust devils were seen in similar comparisons of ICC images from similar local times on different sols, although several faint dust devil tracks on the surface were detected (Banerdt et al. 2020; Charalambous et al. 2021a; Sect. 8).

3.4 Astronomical Images

Imaging of the night sky was done primarily for meteor searches. IDC night images were acquired on sols 126, 176, 234, and 593. ICC night images were obtained 26 times over sols 254-552. Each set comprised 4 images totaling 20 minutes exposure duration.

Meteor searches were performed as part of the mission's focus on impacts and to constrain the small end of the size distribution of potential impactors (Daubar et al. 2018). Some observations were coordinated with predicted meteor streams, but the majority were attempts to measure the background meteor flux (e.g., Domokos et al. 2007). IDC searches were determined to be much more sensitive than ICC ones, due primarily to the ability to aim above the dusty horizon and secondarily to greater intrinsic sensitivity. The ICC's wider FOV only partially compensated for its lower sensitivity. No meteors were detected in any of the search images. Meteor searches were halted when it was determined that sensitivity estimates had been overly optimistic (Lemmon et al. 2020) and the chances of detecting a statistically significant sample of background meteors was negligible.

There was serendipitous value to the night images, however. Sky light was detectable at midnight, suggesting the possibility of airglow, which is a faint emission of light produced by photochemical reactions in the upper atmosphere (Banfield et al. 2020). The sols 126 and 176 meteor searches were also timed such that multiple bright stars appeared in the IDC FOV, to measure flux versus elevation angle for comparison to IDC and ICC tau measurements.

3.5 Structure-from-Motion DEMs

High-resolution DEMs were derived from multiple IDC images with small offsets using Structure-from-Motion (SfM) methods (e.g., Pavlis and Mason 2017). Individual DEMs were generated from overlapping IDC images typically arranged in $n \times n + 1$ arrays using 5 to 58 frames with typical ground resolution of $\sim$2.0 mm (Garvin et al. 2019). A single intrinsic camera model parameterizing focal length, center of distortion, skew, radial distortion, and decentering distortion was estimated from 48 overlapping IDC images acquired on sol 16. The image processing steps consisted of: (1) image alignment, (2) dense tiepoint

matching/filtering, (3) three-dimensional reconstruction to a DEM surface, and (4) orthorectification. DEM generation was computed from a dense point cloud over a uniform grid with sample spacing equivalent to the average resolution of the images (Garvin et al. 2019). This process was utilized to produce DEMs in support of science, HP^3 anomaly resolution (Spohn et al. 2022b), soil mechanics experiments, and to evaluate the local morphology and stratigraphy (Garvin et al. 2019; Spohn et al. 2022b).

4 Instrument Site Selection

After landing and getting the spacecraft in a fully operational configuration, the highest priority was determining where to place the instruments on the surface in the workspace. Instrument placement was based on the spacecraft tilt, workspace topography (relief and roughness), surface characteristics (soils, rocks, etc.), and instrument placement requirements. The process of site selection was carried out by the Instrument Site Selection Working Group (ISSWG). The ISSWG was composed of six subgroups: (1) geologists, (2) physical property scientists, (3) arm and deployment engineers, (4) Multi-mission Image Processing Laboratory (MIPL) personnel, and instrument representatives for (5) SEIS and (6) HP^3. The lander controlled its orientation during landing and the arm is attached to the southern edge of the deck, so the workspace where the instruments could be placed was just to the south of the lander (Fig. 1). The available workspace is limited to a roughly crescent shaped area reachable by the arm extending out to ~2 m away from the lander and ~2 m to either side (Fig. 4). Instrument placement requirements for SEIS (Lognonné et al. 2019) and HP^3 (Spohn et al. 2018) include surface slope, roughness and relief, rocks, load bearing soil, tether geometry, and the desire to be away from the lander (and each other) to reduce noise or interference (Tables 3 and 4). Before landing, preferred instrument locations placed both instruments as far as possible away from the lander (particularly the feet, to avoid noise) and from each other and with SEIS to the west (to avoid crossing tethers). These locations were used as starting points for the site selection process.

Initial ICC images after landing showed dust was on the lens, which made initial workspace mapping difficult. After the arm was deployed, dust-free IDC images of the spacecraft, solar panels, and stereo images of the surrounding terrain were acquired. The first IDC mosaic of the workspace acquired with the arm above the lander was available to the team two weeks after landing on 10 December 2018. Stereo images were processed to create orthoimage and DEM mosaics with 2 mm per elevation postings (Fig. 4a) (Abarca et al. 2019). Analysis of the workspace showed it to be particularly benign with a sandy, granule-rich and pebbly surface, few rocks, and low slopes (Golombek et al. 2020a,b) that met all of the instrument deployment requirements over most of the deployment area. Preliminary instrument locations selected were both near their pre-landing preferred locations.

A higher resolution workspace stereo mosaic was acquired with the arm below the lander deck (and the IDC closer to the surface) and was available to the team on 14 December 2018. Individual frames had a pixel scale of 0.5 mm, and the DEM from these instruments had 1 mm per elevation postings (Abarca et al. 2019) (Fig. 4b). The preliminary instrument locations met (by a large margin) all instrument deployment requirements in the higher resolution data (Fig. 4c). In addition to meeting all deployment requirements, all the "desirements" were also met except for two, which were waived because they were judged to have little impact, at the selected locations (Tables 3 and 4). The instrument placement locations (Fig. 4c) were certified, approved by the instrument Principal Investigators and selected by the project on 17 December 2018.

Table 3 SEIS and WTS deployment requirements and desirements, and primary and secondary ISSWG subgroups who evaluated them. Requirements are numbered 01–14, 27, 28; desirements are numbered 15–26

Requirement ID	Constraint	Primary	Secondary
SEIS-01	SEIS footplane tilt $< 15°$	SEIS	Depl/IDS[a] Geology
SEIS-02	SEIS footplane tilt $< 12°$ for negative pitch slopes	SEIS	Depl/IDS Geology
SEIS-03	WTS footplane tilt $< 15°$	SEIS	Depl/IDS Geology
SEIS-04	No rocks > 3 cm high under SEIS for tilts $\leq 11°$	SEIS	Depl/IDS Geology
SEIS-05	No rocks > 2 cm high under SEIS for $11° <$ tilts $\leq 13°$	SEIS	Depl/IDS Geology
SEIS-06	No rocks ≥ 1 cm high under SEIS for $13° <$ tilts $\leq 15°$	SEIS	Depl/IDS Geology
SEIS-07	No rock or relief > 3 cm high, or > 1 cm low, under WTS skirt over 1 cm length scale	Geology	SEIS Depl/IDS
SEIS-08	No rock > 3 cm in height within 5 cm of the front face of Load Shunt Assembly	Depl/IDS	Geology SEIS
SEIS-09	SEIS footpatch roughness $< \pm 2$ cm vertical relief in 3 cm diameter circle centered on each foot	SEIS	Geology Depl/IDS
SEIS-10	WTS footpatch roughness $< \pm 3$ cm vertical relief	Geology	SEIS Depl/IDS
SEIS-11	SEIS placed on load-bearing soil	Geology	Physical Properties
SEIS-12	SEIS footplane < 1.5 cm higher than the center of the WTS footplane	Depl/IDS	SEIS
SEIS-14	SEIS not to exceed WTS do not exceed envelope	Depl/IDS	SEIS
SEIS-27	LSA can be separated	Depl/IDS	SEIS waived
SEIS-28	No rock or relief > 6 cm above or > 9 cm below WTS footplane under skirt	Geology	Depl/IDS SEIS
SEIS-15	SEIS footplane tilt $< 11°$	SEIS	Depl/IDS
SEIS-16	All three SEIS feet placed on the same material type	Geology	SEIS
SEIS-17	SEIS on terrain with positive pitch	Depl/IDS waived	SEIS waived
SEIS-18	Avoid HP^3 engineering tether (ET) contact with SEIS tether or WTS	Depl/IDS	SEIS
SEIS-19	No rock > 1 cm height under or within 5 cm in the tether direction of Pinning Mass (PM) or Field Joint (FJ)	Depl/IDS	Geology SEIS waived
SEIS-20	Avoid Field Joint (FJ) being placed in or in front of a hole > 1 cm deep, or in front of a rock > 1 cm in height	Depl/IDS	Geology SEIS waived
SEIS-21	Pinning Mass (PM) should be upright (not tilted more than 15 deg.) and clear of rocks or other obstacles	Depl/IDS	SEIS Geology waived
SEIS-22	No obstacles > 3 cm height within a 18 cm (along tether vector) by 24 cm (cross tether) rectangle centered on the Pinning Mass of Pinning Mass (PM)	Depl/IDS	SEIS Geology
SEIS-23	Plane of tether up to the heat-formed bend is lower than the SEIS footplane	Depl/IDS waived	SEIS waived
SEIS-24	Deploy SEIS as far away as possible from the lander	SEIS	Depl/IDS
SEIS-25	SEIS ≥ 1 m away from HP^3 (as far as possible from HP^3)	SEIS	HP^3
SEIS-26	Entire base of Pinning Mass in contact with the ground is achievable	Depl/IDS	SEIS

[a]Depl/IDS are arm and deployment engineers

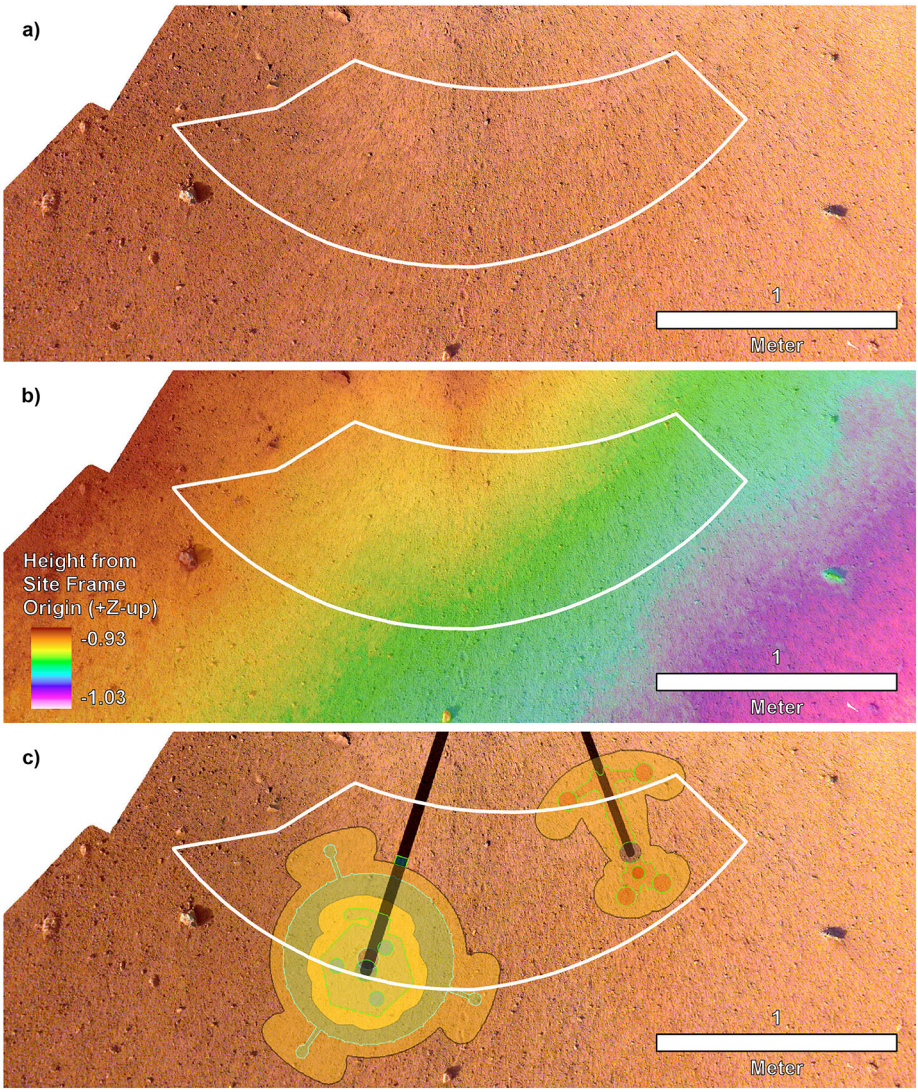

Fig. 4 (a) The first IDC image mosaic created of the workspace at 1 mm/pixel with the deployment area outlined in white. (b) High-resolution DEM produced from the second mosaic of the workspace at 1 mm per elevation posting and the deployment area outlined in white. Note that the deployment area has a total relief measured in centimeters. (c) Locations selected for the instruments with black lines to the instrument grapple points. SEIS and WTS are to the left and HP^3 is to the right. North is up for all

5 Instrument Deployment

5.1 Introduction

The main function of the IDS was to deploy the science instruments to the ground, record their state, and complete any support activities required to get them fully operational in the first 90 sols after landing (Imken et al. 2020). The instruments were deployed within that

Table 4 HP^3 deployment requirements and desirements, and primary and secondary ISSWG subgroups who evaluated them. Requirements are numbered 01–06; desirements are numbered 07–15

Requirement ID	Constraint	Primary	Secondary
HP3-01	HP3 footplane tilt $< 15°$ of horizontal	HP^3	Depl/IDS[a] Geology
HP3-02	No rocks > 3 cm high or relief > 3 cm high under HP3	HP^3	Depl/IDS Geology
HP3-03	HP3 footpatch roughness $< \pm 1.5$ cm	HP^3	Depl/IDS Geology
HP3-04	HP3 placed on load bearing soil	Geology	Physical Properties
HP3-05	Mole egress clear of rocks > 1.5 cm diameter	HP^3	Geology
HP3-06	No partially buried rocks near the HP3 that could be blocking the subsurface path of the mole.	Geology	HP^3
HP3-07	HP3 away from lander and other sources of thermal noise (e.g., rocks)	HP^3	none
HP3-09	HP3 should be $\geqslant 0.9$ m away from SEIS and WTS shadow	HP^3	SEIS
HP3-10	Mole egress clear of rocks > 0.5 cm diameter	HP^3, waived	Geology waived
HP3-11	HP3 feet clear of stones > 2 cm diameter (to prevent sliding)	HP^3	Geology
HP3-12	HP3 on flat (enough) terrain with all 4 feet in contact with the ground, to avoid rocking during mole hammering cycles	HP^3	Geology
HP3-13	It should be checked that there are no line-of-sight obstacles obstructing the ICC field of view	Depl/IDS	HP^3
HP3-15	It is desired to image all four feet of the HP3 SSA using the IDC	Depl/IDS, waived	HP^3, waived
HP3-16	The tether should not be routed over (sharp) surface stones due to wind action over the course of the mission	Depl/IDS	Geology HP^3
HP3-17	HP3 and SEIS engineering tethers should not touch	Depl/IDS	HP^3

[a]Depl/IDS are arm and deployment engineers

time and HP^3 began hammering on sol 92. The three primary deployments for the mission were the SEIS deployment, WTS deployment (over the SEIS), and the HP^3 deployment (Trebi-Ollennu et al. 2018, 2020). Each deployment was split into 4 parts with Go No-Go decisions made on the ground between each. The four steps of the deployment were: 1) align IDA grapple over the grapple hook of the instrument on the deck, 2) open the grapple and hook onto the instrument, 3) lift the instrument off of the deck and carry it all the way to contact with the surface at the commanded location, and 4) open the grapple and back off with IDA (Fig. 5). After each of the deployments, a number of other activities were carried out including localizing each instrument (discussed in detail in the next section), verifying hardware state of tethers or other hardware components, and manipulating actuatable hardware such as the SEIS pinning mass of the Load Shunt Assembly (LSA) (Lognonné et al. 2019).

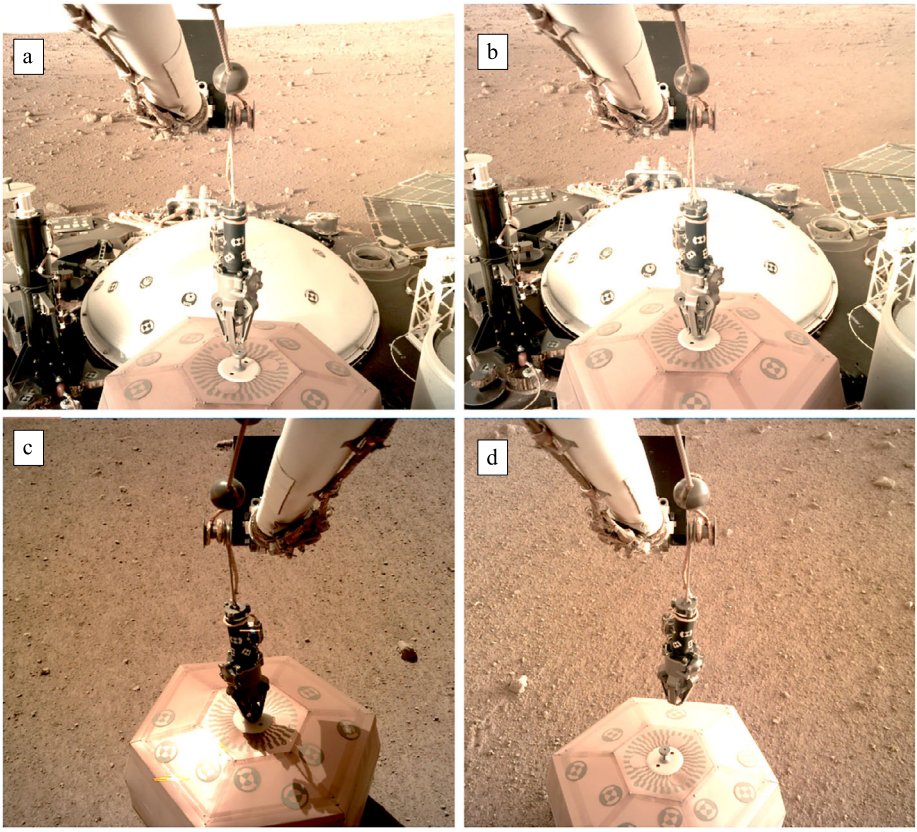

Fig. 5 IDC images showing the four steps of deployment of SEIS. a) Aligning the IDA grapple over the grapple hook of SEIS on the deck. b) Grapple closed around the SEIS grapple hook. c) The instrument moved to the surface, d) The grapple unhooked from SEIS and moved above by the IDA. Note fiducial marks on the WTS (white dome) in a) and b) and on SEIS used to localize them after deployment

5.2 Pre-Landing Testing Campaigns

InSight IDS integrated system testing was completed in a JPL testbed comprising a full-scale replica of the lander, with a full set of IDS electronics and hardware, including an engineering model arm, motor controller, IDC, and ICC (see also Sect. 12). The testbed included a full set of lander electronics that simulated the software environment. This allowed the replica lander to be operated with the same commanding and sequencing used in flight operations. The testbed lander was located in a sandbox made from crushed garnet under a set of lights that mimic the light spectrum on the martian surface. The lander was tilted to match various test configurations using stacks of cinderblocks combined with piles or pits of the garnet (e.g., see Sect. 12).

Prior to landing, the entire deployment phase was carefully tested and characterized to ensure that the team would be able to deploy the instruments as accurately as possible. This campaign involved attempting to deploy all three instruments to all parts of the workspace. Testing included deployment on surfaces up to 15° in lander roll and pitch as well as workspace slope. During these tests, a crane would be used with a constant force

spring attached to the wrist of the IDA to mimic martian gravity. Motion tracking of the fiducial markers on the lander and instrument were used to understand the instrument positions with respect to the IDA's base reference frame. Additionally, grids were used to characterize the amount of error and consistency achievable under different deployment conditions. Other contingency activities such as needing to re-grapple an instrument, pull on the pinning mass to open the Load Shunt Assembly, and imaging were all thoroughly tested in the testbed prior to landing and many of these activities were used during surface operations. The results of this testing provided the knowledge and modeling necessary to be able to deploy the payloads relatively quickly, safely and accurately (Imken et al. 2020).

5.3 Post-Landing Deployment Phase Campaign

Once InSight landed, testing quickly focused on verifying activities for the specific post-landing environment. After landing, InSight had a total tilt between three and four degrees along a southeast heading based on Inertial Measurement Unit readings for pitch and roll of the lander (e.g., Golombek et al. 2020b). In the testbed, the lander deck was tilted along the same heading to within $\pm 0.25^{\circ}$ of the actual tilt on Mars. In addition, the surface was sculpted to match the workspace on Mars. All the major deployment activities were first run in the testbed using the same sequences that were used on Mars. As a result, staffing included both tactical planning and future planning. After each successful execution on Mars, the testbed state would be updated with the latest localization and imaging results. For instance, after the SEIS was deployed, and the Tether Storage Box (TSB) and LSA opened, all three were made to match what was seen in the images to test the pinning mass adjustment and were used to determining how far to pull on the pinning mass to achieve the desired LSA state. A combination of careful recreation of the surface, instrument location and state, and testing, resulted in dry runs that very closely mirrored the actual executions on Mars, ultimately resulting in successful deployment.

5.4 SEIS Deployment

SEIS was the first instrument to be deployed. It was a complicated deployment due to the heavy tether and the non-rigid grapple cable (Sorice et al. 2020). The SEIS was successfully deployed into the workspace between sols 19 to 25 as shown in Fig. 5. All executions were nominal, and initial localization showed that the instrument was in a position that met requirements. After SEIS deployment, a number of different activities were executed to verify the state of the SEIS. From sols 26 to 36, the SEIS science team performed leveling and checkout activities while the IDS team imaged the hardware (Trebi-Ollennu et al. 2020). On sol 37, the SEIS TSB was opened allowing the rest of the tether to fall to the ground and it was imaged to verify its state. On sol 40, the SEIS LSA was opened to isolate the SEIS from the thermal noise of the tether. However, the LSA did not have a visible separation, so a complicated contingency procedure called pinning mass adjustment was performed, in which the scoop of the IDA was used to pull on the LDA grapple hook located 1/3 of the tether length closest to SEIS (Fig. 6). This was executed on sols 56-59. Although several attempts were necessary, the LSA was eventually opened to an acceptable amount to continue with further deployments. In the final checkouts, the SEIS team confirmed that the hardware reconfigurations on the SEIS reduced the noise from the lander on the SEIS by an order of magnitude.

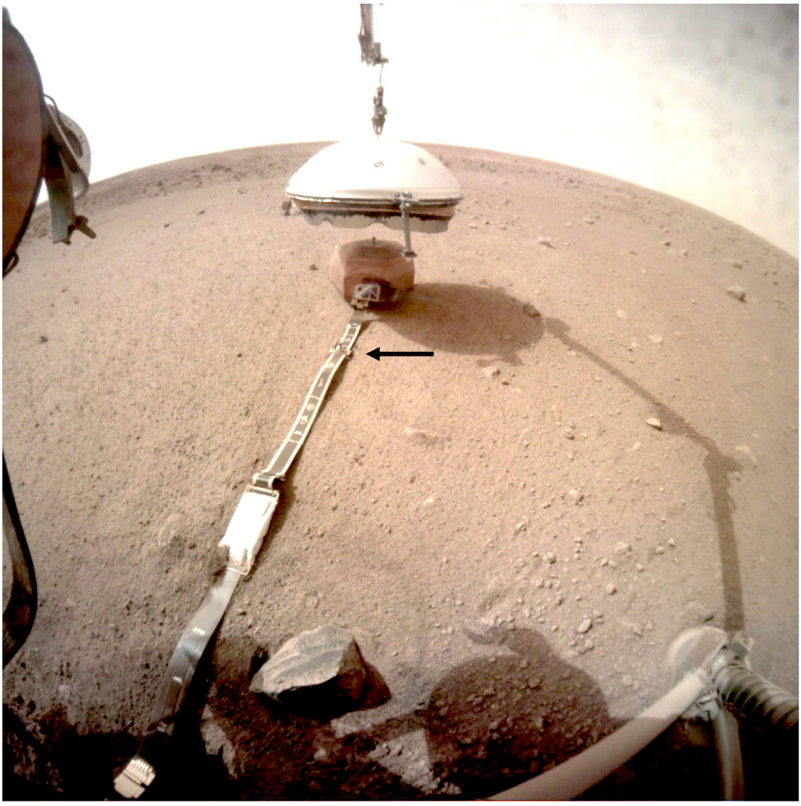

Fig. 6 ICC image showing the WTS being lowered over SEIS on sol 66. Note location of the pinning mass (arrow), which is the ball on a post on the tether near SEIS that was later adjusted by the scoop on the IDA

5.5 WTS Deployment

After deployment of the SEIS, the WTS was deployed to shield the SEIS from environmental noise. Although the WTS was technically a more straightforward deployment than SEIS, as there was no tether weighing part of it down, it had to be placed over the SEIS without any contact. If any part of the SEIS, including the now expanded LSA, had been in contact with the WTS, it would have transmitted wind and thermal noise back into the SEIS. As a result, the error bounds for the WTS deployment were very tight (Trebi-Ollennu et al. 2020) and relied on accurate SEIS localization. The WTS was successfully deployed between sols 64 and 70 (Fig. 6). Subsequently, there was an additional alignment move to adjust the grapple so that extra slack wouldn't cause it to scrape across the WTS. After letting go of the WTS, localization results showed that the WTS was almost perfectly aligned over the SEIS. It took a few sols for the WTS skirt to completely unfold. After recalibration, the WTS resulted in another order of magnitude decrease in noise for the SEIS.

5.6 HP^3 Deployment

The HP^3 was deployed last. Although HP^3 also had a tether that connected it to the lander, it was carried internally and did not tilt the instrument during deployment. However, as the

tether remained in tension when it pulled out of its storage compartment, it did cause the HP^3 to stay aligned radially and sometimes had jolts as the tether was pulled out. Despite these complications, the HP^3 was successfully deployed, between sols 74 and 83. Once again localization results showed that it was deployed as expected. The mole was deployed on sol 87, and sol 92 was the first attempt at hammering into the martian subsurface. With this hammering, the deployment phase was completed. However due to lack of progress by the mole, the next portion of the mission was characterized by mole recovery as discussed later (Sect. 7).

5.7 IDS Deployed Instrument Localization

After deploying the instruments on the martian surface, it was important to determine an accurate estimate of their locations (Bailey et al. 2020). From a science perspective, precisely knowing the relative position between the instruments (e.g., Brinkman et al. 2022) and the lander was necessary to be able to interpret science results and identify noise in the data captured by the instruments (Golombek et al. 2020b). Besides the science benefit, instrument localization also was required to continue with the rest of instrument deployment (and eventual moving of the HP^3). From a safety perspective, the information from localizing the instruments was fed into the IDA's collision modeling to ensure that no inadvertent contact was made. In addition, these positions were necessary for several precise operations such as the adjustment of the SEIS pinning mass, the WTS deployment, and the HP^3 re-grappling and re-deployment. The requirements on the localization were to know the position within 1.5 cm and 1.5°.

The primary localization method used was monocular fiducial localization (Bailey et al. 2020). Fiducial localization consisted of capturing images of fiducial markers placed on each instrument and the WTS (e.g., Fig. 5), which were scanned with respect to their local frame. The two types of fiducials used on the instruments were single point fiducials and two-dimensional bar codes (Olson 2011). Four single point fiducials are needed to be in an image frame to localize the instrument. However, two-dimensional bar codes are able to provide a full 6 degree of freedom pose from a single fiducial (Olson 2011). These fiducials were compared against a metrology map of the fiducials to determine the frame transformation from the IDA frame to the instrument frame (Bailey et al. 2020). After calculating the pose using fiducial localization, a final check was done using the grapple (Trebi-Ollennu et al. 2020). In this check, the IDA grapple was lined up over the calculated instrument pose and moved 2 cm vertically capturing a picture at each pose. This position and motion confirmed the cross-range and gravity-oriented errors, but to get the final radial axis this activity was executed late in the day so the sun cast long shadows to confirm alignment. Based on the grapple localization and other close contact operations like the pinning mass adjustments, the errors in the localization were characterized. The full identification of error sources and performance are discussed in Bailey et al. (2020), but ultimately the refined localization values allowed for successful localization of the instruments. Lastly, workspace orthophotos created from IDC stereo image mosaics (e.g., Sect. 4) were also used to determine the location of the instruments in the IDA, site, and cartographic frames for use by the science community and agreed to within 1-2 cm with the fiducial results (Golombek et al. 2020b).

6 Geology Investigation

Geology investigations were by far the greatest beneficiary of upgrading the black and white detectors to color and elevating the surface panorama to a requirement during development. Color is central to identifying different geological materials and obtaining a

complete panorama provided the means to place the surface observations of the landing site in a broader context with the remote sensing observations obtained during landing site selection (Golombek et al. 2017). Without these changes and restricting the IDS to only image the workspace and place the instruments, the geology investigation would have been severely limited. Instead, color panoramas and images of the spacecraft, the surface beneath the spacecraft, the immediate area around the spacecraft, the instruments and interactions with the surface, disturbed and scraped areas, and piles produced from scooping and dumping soil enabled a much richer geology investigation that successfully addressed all of the geology and physical properties goals outlined prior to landing (Golombek et al. 2018a). In this section, the geology of the landing site is summarized and related to the different IDC images enabled by the IDA arm motions with references to full length papers with more details and to other sections of the paper.

The lander is located in western Elysium Planitia on the western side of a quasi-circular depression (Golombek et al. 2020a,b), interpreted to be a degraded ~27 m diameter impact crater (Warner et al. 2020; Grant et al. 2020). This depression, informally named Homestead hollow, has a smooth, sandy, granule- and pebble-rich surface and is adjacent to slightly rockier and rougher terrain to the west (Fig. 7). The panorama shows impact craters in various stages of degradation ranging from circular hollows with little relief to fresh secondary craters from Corinto that are less than ~2.5 Ma (Golombek et al. 2017). Images near the lander show some rocks are dark gray and appear very fine grained, consistent with aphanitic, dark mafic rocks (basalts). Rock abundance is low with fractional coverage of a few % (Golombek et al. 2020a, 2021). No obvious aeolian bedforms (e.g., dunes or ripples) have been identified close to the lander, but some are associated with relatively fresh impact craters >50 m away (Fig. 7). They are bright, covered with dust (Maki et al. 2021), indicating relative inactivity (see also Sect. 8). HP^3 radiometer measurements of the surface (Mueller et al. 2021) yield a thermal inertia dominated by sand and not affected by rocks (Golombek et al. 2020a; Piqueux et al. 2021; Grott et al. 2021). Stereo panoramas enable measurements of rock size and shape that indicate an impact origin for the hollow that was degraded and mostly filled by mass wasting and aeolian activity that transported sand from ejecta into the crater (Golombek et al. 2021; Grant et al. 2020, 2022; Weitz et al. 2020). The Homestead hollow surface has a crater retention age of ~400-700 Myr (Warner et al. 2020).

Stereo images beneath the lander reveal pits produced by the retrorockets that show steep sides with pebbles and granules cemented in a finer grained matrix indicating duricrust (hardened soil) that is 10-20 cm thick (Golombek et al. 2020a; Spohn et al. 2022b) (similar to the walls of the exposed pit around the mole; Sect. 7). Images near the lander show radial striations in the soil indicating dispersal of unconsolidated sand and removal of bright dust by the landing rockets (Golombek et al. 2020a; Warner et al. 2022) (Fig. 7). The shallow stratigraphy consists of surficial dust, over thin unconsolidated sand, underlain by a variable thickness duricrust, with poorly sorted, unconsolidated sand with rocks beneath (Golombek et al. 2020a; Warner et al. 2022). Surface observations and shallow seismic results (Lognonné et al. 2020; Brinkman et al. 2022) are consistent with expectations made from remote sensing data prior to landing (Golombek et al. 2020c), indicating an impact-fragmented regolith 3-10 m thick overlying coarse ejecta blocks that grade into fractured basaltic lava flows (Golombek et al. 2017, 2018a, 2020c; Warner et al. 2017, 2022). The basalts, ~170 m thick beneath the lander (Pan et al. 2020), are Hesperian to Early Amazonian in age (Warner et al. 2017, 2022), with a low-velocity zone at 30 to 75 m depth that may be a sedimentary layer sandwiched within the basalts (Hobiger et al. 2021). Beneath the basalts are weak Noachian sedimentary rocks that filled this portion of the northern plains (Pan et al. 2017, 2020). The plains on which InSight landed can be considered a type example of Early Amazonian to Hesperian lava plains on Mars, which cover vast portions of its

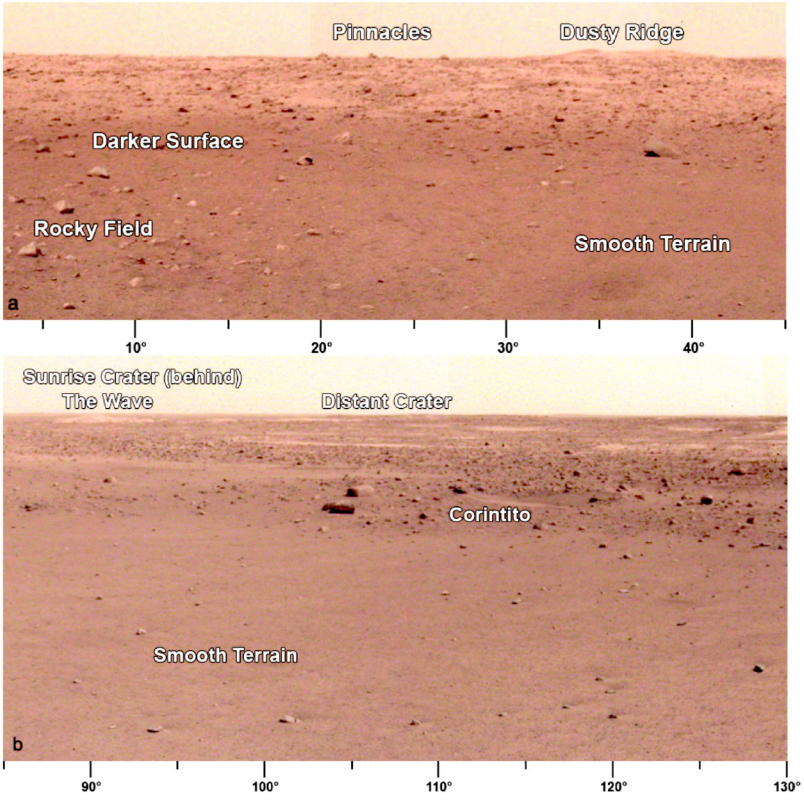

Fig. 7 Portion of a panorama around the InSight lander. a) Area to the north-northeast of the lander (azimuths below image) shows a darker surface, where dust was removed within 20 m of the lander. Rockier surface is to the west (Rocky field), and smooth terrain of Homestead hollow is to the east. The Pinnacles rocks and Dusty Ridge (a bright eolian bedform) on the southern edge of a degraded impact crater, are located about 50 m north of the lander. b) East-southeast (azimuths below image) of the lander shows smooth terrain to the edge of Homestead hollow and rougher and rockier terrain beyond. The Corinto secondary crater (Corintito) is on the edge of the hollow and $<$2.5 Ma (Golombek et al. 2020a). Circular soil filled depressions (hollows) are in the distance, and bright eolian bedforms (The Wave) and Sunrise crater rim are on the horizon about 400 m away. The rim of Distant crater, a larger (460 m diameter), relatively fresh crater to the east-southeast is $\sim$2.4 km away

surface (e.g., Lunae, Sinai, Solis, Syria, Thaumasia, Syrtis Major, Hesperia, Malea Plana, Warner et al. 2022).

7 Mole Recovery Operations

7.1 Introduction

The Heat Flow and Physical Properties Package (HP^3) was designed to measure the temperature and thermal conductivity profile down to a depth of 3–5 m along with related physical properties. The temperatures would have been measured using sensors in a Kapton science tether that a small penetrator – nicknamed the mole – would have pulled down into the subsurface (Spohn et al. 2018). At the end of February 2019, following successful deployment

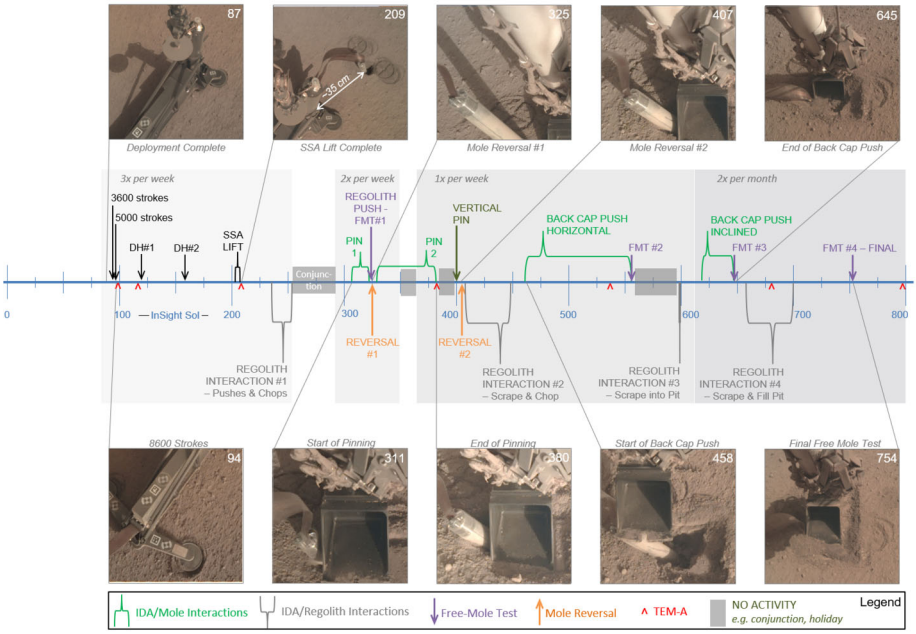

Fig. 8 This linear timeline shows key periods (braces) and events (arrows and carets) of the mole recovery activity using the IDA from the end of SSA deployment (sol 87) to the final free-mole test (sol 764). Callout figures with sol numbers in the upper right show selected full-frame views from the IDC. Shaded background regions indicate changes in operational cadence

of the HP^3 Support Structure Assembly (SSA), the team commanded the mole to start hammering. It soon became clear that the mole had failed to penetrate to the target depth of 70 cm (tip depth) for the first hammering session. The team tried for almost a full martian year (22 months) to diagnose the anomaly and assist the mole in penetrating deeper. A complete chronological narrative of the mole recovery activities can be found in Spohn et al. (2022b), and key lessons learned applicable to the design and operation of the mole penetration are detailed in Spohn et al. (2022a). The mole eventually penetrated to a final tip depth of about 40 cm aided by force applied using the scoop at the end of the robotic arm. This final configuration of the mole has the back cap 1-2 cm below the surface, which enabled thermal conductivity measurements that were unaffected by direct solar or atmospheric exposure of the mole (Grott et al. 2021).

Throughout the mole recovery activities executed over 22 months (March 2019 to January 2021), the IDA and IDC were used extensively to gain information about the current state of the mole, SSA, and Science Tether (ST); and the IDA end effectors (grapple and scoop) were used to interact with HP^3 hardware and the regolith (Sorice et al. 2021) (Fig. 8).

7.2 Imaging

The IDC images provided a major source of data in the anomaly resolution process. In the first two months of the anomaly, the IDC was positioned in various viewing geometries to gain as much information as possible before interacting directly with the hardware. Static image mosaics of the HP^3 SSA and surroundings were acquired during normal illumination conditions, typically during the mid-afternoon for the best lighting and thermal conditions.

Attempts to understand the situation below the SSA, prior to its removal, motivated the acquisition of 'long shadow' images taken with the sun low on the horizon, though these images ultimately did not provide much useful information. A further combination of IDC position and lighting conditions allowed imaging of the "SSA window", a vertical slit ∼1 cm wide in the lander-facing side of the SSA's central tube. Through this window the ST was seen to be in an unexpected configuration, with contrast-stretching of images revealing the depth-encoding markings on the edges of the science tether (in a nominal configuration the ST edges would not be visible through this opening).

During 'diagnostic hammering' activities (consisting of ∼200 hammer strokes, as opposed to the 3000+ strokes during the first two penetration attempts), the IDC was used to capture both wide-view and SSA-window closeups of the support structure while the mole attempted to penetrate. The IDC was used to create low-frame-rate 'movies' of the activities. The IDC was not designed for rapid image acquisition, and the shortest time between frames using auto exposure was on the order of ∼33 s. By selecting a fixed exposure time (adjusted for each activity depending on the time of day), rather than auto-exposure, the frame rate could be improved somewhat.

While the SSA was still covering the mole, the movies provided some limited information about the system dynamics; to wit: mole hammer strokes caused the SSA and science tether (seen through the window) to slightly shift position, but with no significant penetration from the 198 hammer strokes of each hammering. However, the sequences developed to acquire IDC movies were used extensively after SSA removal to capture mole behavior any time it was commanded to hammer.

7.3 Removing the SSA

After the anomaly response team determined that no further information could be gathered while the SSA was covering the mole, the decision was made to use the IDA to remove the SSA. However, the off-nominal position of the science tether and the lack of penetration itself suggested that the ST might be snagged within the support structure, motivating a plan which would lift the SSA away from the mole in stages. This required the recovery team to assess whether the removal process was proceeding without the mole being extracted by the lift of the SSA.

The first step was to re-grapple the SSA grapple hook, a procedure that was not part of the nominal deployment plan (similar to most of mole recovery activities). Testing was carried out in the InSight testbed at JPL (Sect. 5.5) after it had been reconfigured to reflect the geometry of the hardware on Mars (Sorice et al. 2021). The execution on Mars consisted of grapple stow release, coarse positioning, fine positioning, grappling, and tensioning (removing the slack in the flexible grapple cable) without lift. All steps required post-facto verification consisting of IDC and ICC images, along with telemetry about IDA joint angles.

Once grappled, the lift proceeded through three stages: (1) lift of the SSA by 12 cm to raise it above the predicted top-level of the mole back cap; (2) lift of the SSA by an additional 13 cm (total lift of 25 cm) to tension the ST and pull a small amount of it through the SSA's Tether Length Monitor (TLM); and (3) a final additional lift of 29 cm (total lift of 54 cm) followed immediately by IDA moves to bring the SSA closer to the lander and lower it to the surface. The successful completion of steps (1) and (2) provided evidence that the mole and science tether were not in fact snagged within the SSA. The IDC could not see the mole or ST during the first lift, and the mole was only barely visible at the end of the second, but evidence that the mole and ST were moving freely (without snags) came from ICC images,

IDA joint current telemetry, and tether extraction from the tether storage compartment in the SSA as reported by the TLM.

A significant concern about the lift procedure was that the IDA would need to hold the SSA in an elevated position for 3 sols at the end of both lifts to allow ground-in-the-loop verification of the preceding activity. Though the SSA is quite light without the mole inside (∼2.1 kg), the IDA had not been designed for long-term support of a cantilevered load, and the chances of a safing event delaying the lift timeline were considered. The testbed was used to verify the IDA's ability to statically support the SSA using a modified weight model.

After the SSA had been successfully removed, the IDA was used for three classes of mole recovery activities: characterization of the mole via IDC imaging, interacting with the soil, and directly assisting the mole.

7.4 Characterizing the Pit

Characterization of the unexpected pit around the mole after the SSA was moved was performed with sequences of image mosaics during various times of day (differing illumination states), and these mosaics were used to create coarse and fine (Structure-from-Motion) elevation models (Sect. 3.5) of the pit and surrounding regolith (Garvin et al. 2019; Spohn et al. 2022b). Such image sets were captured following the exposure of the pit, after each regolith-interaction activity, after each major mole-assist activity, and after the two mole reversal events.

Various lines of evidence, culminating with the discovery of the pit after SSA removal, suggested that the root cause of the mole's failure to penetrate was either an obstacle in front of the mole (largely ruled out by the subsequent penetration), or a lack of friction with the regolith. In an attempt to better understand the mechanical properties of the unexpectedly cohesive regolith, and in the hopes of increasing friction against the mole hull, the IDA scoop was used several times to interact with the surface. These interactions were of three types: vertical 'pushes' against the regolith with the flat back-surface of the scoop, vertical 'chops' of the regolith near the pit walls using the scoop's tip, and approximately horizontal 'scrapes' of the loose, ∼1-cm-thick unconsolidated surface layer.

7.5 Interaction with the Soil

A flat push on sol 240, five months after the anomaly occurred, was the first regolith interaction of the mission. The action on Mars was preceded by an extensive testing campaign at JPL, wherein IDA motion sequences were developed, the behavior of the IDA when pushing against the surface was characterized, and the magnitude of the force that could be applied by the IDA at this location (∼40 N at most) was estimated. The result of the push next to the pit was a cm indentation of the unconsolidated layer, but no effect on the pit was observed.

Further interactions attempting to collapse the walls of the pit were executed with the vertical 'chops' with the scoop tip (Marteau et al. 2021). The first set of four chops occurred on sols 243, 250, and 253. These were largely unsuccessful at making any significant changes to the pit, though one of the sol 243 chops did break off a 1 cm by 1 cm wedge of regolith that fell into the pit. One other chop occurred on sol 420 after the second mole reversal event, again with the goal of collapsing more material around the mole body. A small amount of consolidated material was broken off in this attempt, but the pit walls otherwise remained largely unchanged.

The last type of regolith interaction, the scrapes, were intended to fill the pit with soil. After developing and testing the sequences in the testbed, a small few-cm scrape test was

conducted away from the pit on Mars on sol 417 to provide data for anticipated future activities. Further scrapes, which were longer and actually brought material into the pit, were executed on sols 598, 673, and 700. These were successful in bringing loose material into the pit, and in fact the very first full scrape brought in enough material that the mole was nearly fully obscured.

The previously described activities of imaging (IDC movies, in particular), SSA lift, and regolith interaction were not part of the requirements or testing baselined for the IDA. However, the most unusual and unanticipated activity of the IDA was its use in directly assisting the mole with penetration.

7.6 Assisting the Mole

Four techniques were used to assist the mole with the IDA. The first to be employed, which provided substantial success, was known as 'pinning.' In a pinning activity, the edge of the IDA scoop was brought into contact and pre-loaded horizontally against the cylindrical body of the mole. To enable this, the testbed was used to investigate various geometries by which the IDA could safely approach the mole without encountering interference with the support structure, the ST, or the mole itself. After trying several approaches, it was determined that the best approach angle was by moving the scoop from right to left as seen by the IDC (west to east).

This additional external force from pinning was expected to increase friction on the mole hull, providing some portion of the friction that had been expected to come from unconsolidated soil (see Wippermann et al. 2020; Spohn et al. 2022a). This external application of force was successful in resisting the natural rebound of the mole mechanical system and allowing the mole to penetrate. In the two pinning campaigns (see Spohn et al. 2022b), the mole made downward progress every time it hammered while pinned by the IDA scoop. The first campaign (sols 302–318) resulted in the mole penetrating 5 cm (measured along the mole body) and ruled out the presence of an obstructing stone, thus revealing lack of sufficient regolith friction due to the cohesion of the duricrust to be the true root-cause of the mole's failure to penetrate after it left the support structure (Fig. 8).

The second technique employed was a variation on the regolith 'push' maneuver described above. This was employed at the end of both pinning campaigns when the mole back cap was too close to the surface for lateral pinning to remain a viable option due to risk of a side-swipe of the science tether by the pre-loaded scoop. The rationale was that pushing on the regolith with the scoop adjacent to the pit would transfer pressure through the regolith and increase the friction experienced by the portion of the mole embedded in regolith at the bottom of the pit. This expectation proved to be incorrect: a combination of the IDA's limited force-application ability and the consolidated nature of the subsurface pit-forming layer likely contributed to this method not providing much friction on the mole body. Both times this near-pit push was attempted, the result was a mole reversal event, where the rebound of the mole was uncompensated and resulted in self-extraction.

The third method, termed 'back cap push', required the most careful positioning of the IDA and scoop (Fig. 8). In this technique, either the scoop tip or its left side edge (as seem from the lander) would be pre-loaded against the back cap of the mole, providing direct resistance to the mole's rebound. This method had been previously considered, but was deprioritized due to numerous potential risks. The mole was inclined from vertical, preventing the IDA, with its limited degrees of freedom, from directly following its progress as it penetrated. The back cap of the mole has many irregular features which precluded a slip-free contact between the mole and any available surface of the scoop. This potential for slip

posed a risk to the science tether, which as in the side-load pinning action, could be damaged by a side-swipe from the pre-loaded scoop. Finally, the whole process required many command cycles of positioning and verification for each hammering sequence, representing a significant burden on InSight's operations team.

Following the second reversal event, the anomaly response team concluded that the risks were acceptable and began the back cap push campaign extending from sol 454 to sol 645. This consisted of 12 separate sequences of a slight IDA retraction, positioning of the scoop, pre-load, and hammering while preloaded. The first nine of these were performed with the scoop's back edge in a horizontal configuration. Once the mole was too close to the surface to permit this geometry to be used further, three more pushes were conducted with the scoop at a slightly inclined angle. These inclined-scoop pushes allowed the scoop to follow the mole as far as ∼2 cm below the original surface until the regolith surrounding the pit impeded the scoop from going any further. The back-cap push activities were successful, allowing recovery from the second mole reversal event and enabling the mole to penetrate to a back-cap depth of ∼2 cm below the original regolith surface.

The fourth and final method of IDA assistance was employed in concert with interleaved scrape and 'tamp' activities. Tamping was simply the application of the 'push'-type of regolith interaction in which the back of the scoop was pressed onto the loose material brought into the pit by the scrapes. Three scrapes were conducted after the last back-cap push activity, on sols 673 and 700, with a tamp following the first, and a persistent pre-load push after the second. The final configuration of the last tamp/push (sol 734) was maintained for the final free mole test, conducted on sol 754 (Fig. 8). In this final test, the mole in the pit was covered by scraped and tamped soil and the scoop was positioned such that it would prevent any mole rebound and extraction. The test was unsuccessful and the mole did not penetrate further, as revealed by the motion of the science tether. Motion of soil particles within the scoop coinciding with the hammering indicated that the mole was attempting to rebound but was held in place by the scoop (see Spohn et al. 2022b). This concluded the mole recovery activity.

7.7 Shallow Subsurface Properties

The penetration record of the mole, the thermal conductivity and diffusivity measurements, and seismic data recorded during the hammerings were used to derive a model of the properties of the first 40 cm of the martian soil at the landing site (Spohn et al. 2022b and Fig. 22 therein) that are consistent with the shallow stratigraphy derived by the geology investigation (Golombek et al. 2020a and Fig. 9 therein; Warner et al. 2022 and Fig. 28 therein). Accordingly, a duricrust of about 20 cm thickness is found underneath a one-centimeter-thick unconsolidated sand and dust layer. Beneath the duricrust a sand layer of about ten-centimeter thickness is found followed by a layer of a sand mixed with gravel, possibly consisting of debris from a small impact crater.

The penetration resistance of the sand/gravel layer is best constrained and was found to be 5.3 MPa while the duricrust has a 7 to 18 times smaller penetration resistance (Spohn et al. 2022b). Applying cone penetration theory, the resistance of the duricrust was used to estimate a cohesion of 2–15 kPa depending on the assumed internal friction angle of the duricrust. Pushing the scoop with its blade into the surface and chopping off a piece of duricrust provided another estimate of the cohesion of about 6 kPa (Marteau et al. 2021, 2022). Soil cohesion estimates were obtained from the experiments performed on sols 240 and 250 in which the scoop was pushed down near an open pit that formed around the HP^3 mole during initial hammerings. By applying three-dimensional slope stability analysis

with measurements of robotic arm forces at the scoop and images, a cohesion of 5.8 kPa was estimated assuming an internal friction angle of 30° (Marteau et al. 2021, 2022; Spohn et al. 2022b). The density of the topmost sand layer is estimated to be 1200 kg/m^3, while that of the duricrust is 950-1100 kg/m^3, followed by 1300-1500 kg/m^3 for the sand layer underneath, and by 1600 kg/m^3 for the deepest sand/gravel layer (Spohn et al. 2022b). The thermal conductivity increases from 14 mW/m K to 34 mW/m K through the one-centimeter sand/dust layer, maintains the latter value in the duricrust and the sand layer underneath, and then increases to 64 mW/m K in the sand/gravel layer below (Grott et al. 2021; Spohn et al. 2022b).

The hammerings of the mole were recorded by SEIS and the signals could be used to derive a P-wave velocity of 119^{+40}_{-19} m/s and a S-wave velocity of 63^{+11}_{-7} m/s (Brinkman et al. 2022) representative of the entire regolith layer to 40 cm depth. These values are in reasonable agreement with previous lab estimations conducted on Earth on various regolith simulants (Delage et al. 2017, 2022) and initial seismic results (Lognonné et al. 2020). Together with a representative density of 1211^{+149}_{-113} kg/m^3 (Grott et al. 2021), the elastic moduli were calculated from the seismic velocities. The shear, bulk and Young's moduli were found to be $4.47^{+2.0}_{-0.83}$ MPa, $7.79^{+1.60}_{-1.55}$ MPa, and $11.48^{+5.91}_{-2.23}$ MPa, respectively, and the Poisson ratio to be $0.29^{+0.12}_{-2.23}$ (Brinkman et al. 2022).

8 Aeolian Change

It was recognized prior to landing that InSight offered a unique opportunity to study active sediment transport because of the prospect of continuous, high-frequency meteorological data that could be used to correlate aeolian surface changes with the winds that produced them (e.g., Golombek et al. 2018a). What was unexpected is that the IDC on the IDA would be positioned close enough to the ground for extended periods, which enabled detailed analysis of individual particle motion and helped constrain the threshold friction wind speed needed to initiate the observed motion (Charalambous et al. 2021a; Baker et al. 2021).

Between sols 298–400, the IDA was positioned with the scoop placed on the surface over the HP^3 mole and pit (see Sect. 7). This stationary positioning allowed the IDC to remain deployed at the closest possible proximity to the surface (a height of 0.65 m). As described in Charalambous et al. (2021a), this specific setup permitted a consistent and extensive aeolian change-detection experiment with sufficient resolution (0.53 mm/pixel) to identify individual grains that moved. In this position, the camera could effectively resolve grains as small as ∼1 mm in diameter (coarse sand) – the smallest possible so far during InSight's operations.

Overall, these observations revealed a highly stable surface at Homestead hollow, which although dominated by fine material, only very intermittently experienced localized and low-flux aeolian changes and is consistent with inferences made from the local geologic setting (Golombek et al. 2020a; Grant et al. 2020, 2022; Warner et al. 2020). The occurrence of these aeolian changes is correlated to the passage of daytime convective vortices (Charalambous et al. 2021a; Baker et al. 2021). The identified surface changes in Charalambous et al. (2021a) caused by vortices were preferentially located in areas of higher surface roughness and downwind of roughness elements such as rocks and deployed instruments which locally enhance grain detachment. Other sites on Mars have reported increased aeolian activity due to strong regional and local slope winds and related effects that contribute to sustained strong winds that promote sediment transport (e.g., Baker et al. 2018b, Newman et al. 2022). In comparison, saltation at InSight appears multidirectional, short-lived,

and sporadic as aeolian changes are vortex-dominated (Charalambous et al. 2021a). While there have been observations of sporadic saltation at InSight, it is unlikely to be sustained in contrast to some other sites on Mars (Charalambous et al. 2021a). These observations have led to the conclusion that the net sediment flux into and out of Homestead hollow is likely close to zero in the modern era. Ongoing saltation at Homestead hollow appears to be confined within the paths of transient vortices, which is consistent with the general paucity of modern bedforms seen from orbit and the surface, and vortices, unlike free-stream winds, do not generate ripples or dunes (Golombek et al. 2018a, 2020a; Grant et al. 2020; Warner et al. 2020).

Images acquired from the ICC and orbital cameras implied that ongoing surface changes at Homestead hollow are chiefly confined within surface dust devil tracks (Charalambous et al. 2021a; Perrin et al. 2020). This was consistent with the observation that all aeolian changes detected from the lander correlated with the passage of daytime convective wind vortices (Charalambous et al. 2021a; Baker et al. 2021). The IDC's unique position thus enabled analysis of small-scale particle dynamics during such vortex encounters, providing insight into the mechanisms responsible for surface darkening and track formation across Elysium Planitia and other plains regions. Low-albedo dust devil tracks are hypothesized to form when lifting or redistribution of fine dust particles reveal coarser (and generally darker) underlying grains (e.g., Greeley et al. 2006; Reiss and Lorenz 2016). Nonetheless, the forces responsible for lifting fines within martian vortices are still poorly-understood.

Examination of vortex-induced particle motion occurring in close proximity to the lander instruments (i.e., the IDC and wind sensor) allows us to confidently correlate atmospheric conditions with surface changes. Comparison between lander data and transport models suggest that grain mobilization is promoted by the increased stress during vortex encounters caused by, for instance, the vertical pressure gradient within the core and the drag force of quickly rotating winds that can be further enhanced by the vector sum with strong background winds (Baker et al. 2021; Charalambous et al. 2021a). Furthermore, dominant stresses and modes of transport may vary with particle size. For example, vertical pressure gradients are thought to be more effective on finer particles (Balme and Hagermann 2006; Greeley and Iversen 1985; Greeley et al. 2003), whereas horizontal drag forces may be responsible for surface creep of coarser particles. While dust can become suspended in the atmosphere, coarser particles are more likely to move via saltation (parabolic hops meters long) across the surface or due to impact or drag-induced rolling. Rolling has also been proposed as a potential mechanism of mobilization of low-mass dust aggregates (Sullivan et al. 2008).

One particularly interesting detection of vortex-induced surface activity occurred on sol 385, while the IDC was positioned close to the surface. Aeolian changes on this sol included dust lifting with widespread pebble and rock dust-coating removal, saltation of fine sand and surface creep of very coarse sand (1 mm, up to 3 mm in diameter), similar to motion observed at other landing sites (e.g., Baker et al. 2018a). The identification of saltation and surface creep during this event was possible because of the unique position of the IDA close to the surface. Charalambous et al. (2021a,b) report concurrent seismic and magnetic signatures observed during this vortex event (and other encounters) associated with ground tilt acceleration and perturbations in the magnetic field strength, consistent with charged-particle motion. Through the combined analysis of seismic data, atmospheric measurements, and surface and orbital images, they identify the trajectory and surface modification of a dust devil encounter on sol 385, which included a pressure drop of 5.5 Pa with a peak wind speed of 31 m/s, the second strongest during the first 400 sols of InSight's surface operations. Another notable example occurred on sol 127-128, which included orbital and surface images of dark dust devil tracks that were produced (Banerdt et al. 2020).

The InSight landing site in Elysium Planitia is a regolith-covered, Hesperian-Early Amazonian smooth basaltic lava plain that is representative of many other plains regions on Mars that share a similar geomorphic evolution and geologic history, with comparable morphologic and sedimentologic characteristics (Golombek et al. 2006a, 2018a, 2020a; Warner et al. 2017, 2022). Most importantly, these sites have common surface-alteration processes, such as impacts, mass wasting, and winds that change the surface slowly (e.g., Golombek et al. 2006b, 2014; Sweeney et al. 2018). Observations of wind-induced motion of sand and dust at the InSight landing site provide a lens into the transport mechanisms of such dusty plains where in-situ data is not available, and provide a proxy on the degree of ongoing aeolian activity at these sites.

9 Tether Burial

9.1 Rationale for Tether Burial

The best seismic measurements require near-perfect isolation of the seismometer from its environment. However, in practice it is necessary to connect a cable, or tether, to supply electric power and transmit commands and data. A tether will inevitably transmit unwanted mechanical vibrations from outside the seismometer. Field tests on Earth demonstrate that buried tethers generate significantly less noise from winds interacting with the tether, lander induced noise transmitted through the tether, and by the thermal stresses generated in the tether (Lognonné et al. 1996). Burying the tether not only isolates it from temperature fluctuations and wind, but the friction of the soil also anchors it to the ground. On Mars, SEIS measurements are often interrupted by "glitches," which are step functions in acceleration caused by thermally-driven stick-slip events in the suspension of one component, or multiple components of the supporting systems, which results in a small tilt of the sensor assembly (Kim et al. 2021; Scholz et al. 2020). The orientation and direction of a large family of glitches suggests that they are associated with the tether. Due to the large number of such glitches present in the SEIS data (e.g., Lognonné et al. 2020; Scholz et al. 2020), the project decided to attempt to bury the tether during the extended mission.

9.2 IDA Tether Burial Activities

To bury the SEIS tether, the IDA needed to excavate soil into the scoop, position it above the tether, and then dump it onto the tether. Because of the harder duricrust under the thin unconsolidated top layer, the scoop was not able to easily dig deeply into the soil to acquire scoopfuls of soil. As a result, a sequence of IDA motions was designed to scrape soil from the top few cm of unconsolidated soil with the tip of the scoop to create a pile of material that could then be more easily scooped. This was accomplished by using a "press-and-pull" approach, attempting to press the scoop into the soil two to three cm and performing a scraping motion. Scrapes were commanded by first placing the IDA directly above the expected scrape starting point and by lowering it down to hover closely above the expected terrain contact point. The IDA scoop was moved downward until reaching contact with the terrain via a guarded motion, before pulling the scoop in the direction towards the lander to create the pile. Subsequent IDA motions slid the scoop into the side of the pile and then rotated the wrist joint to excavate the soil in the scoop.

To dump the soil at the correct location on the tether, the operations team had to position the scoop above the tether (Fig. 9), accounting for the motion of the soil as it fell from the

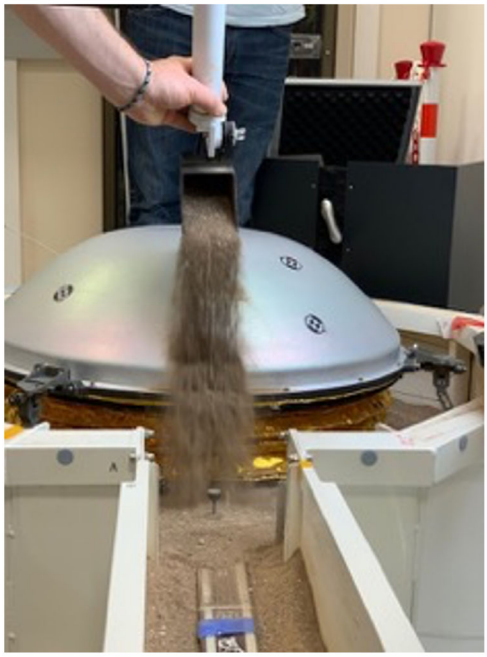

Fig. 9 Dump test on the WTS and SEIS tether in CNES testbed, using a hand-held three dimensional model scoop. Note the ball on the post of the pinning mass of the tether upon which soil is being dumped

scoop onto the tether. There were two techniques for dumping soil on the tether. The first poured soil directly on the tether. The second poured the soil on the dome of the WTS so it slid off onto the tether close to the WTS. Dumping soil on the WTS was carried out to reduce the chance of soil pushing against the WTS skirt and potentially breaking its seal with the ground.

9.3 Testbed Activities to Support Tether Burial

To help in designing the IDA sequences to effectively bury the tether, two testbeds were used, one at CNES (Centre National d'Études Spatiales, France), and the other at JPL (see Sect. 5.2). The tests at CNES used the SEIS qualification model, the tether flight spare, and the WTS qualification model with Mars Mojave Simulant (Peters et al. 2008) (Fig. 9). A three-dimensional printed scoop was mounted to a rod and manipulated by hand to mimic the scoop at the end of the IDA. Test dumps were conducted at CNES and recorded with two webcams. Tests addressed the rotation axis of the arm and scoop as it dumped the soil, how to arrange the piles to effectively cover the length of the tether, the effect of wind on the dispersion of the soil, and the best height of the scoop when dumping the soil. A compound motion of the arm was selected to have the scoop rotate around its tip as this produced a taller, steeper pile. The IDA made three separate motions during the dump. First, the IDA moved the scoop around its tip until the scoop back was nearly horizontal. Then, it moved the scoop past horizontal by a few milliradians. Finally, the IDA moved to rotate the scoop the remainder of the way around its tip, until the scoop back was nearly vertical. The height of the dump was set to 45 cm above the ground, except over the WTS where it was set to 55 cm above the ground. Tests also showed that less soil was dispersed when winds were low and that the soil could be dumped to bury the tether without risk to the SEIS.

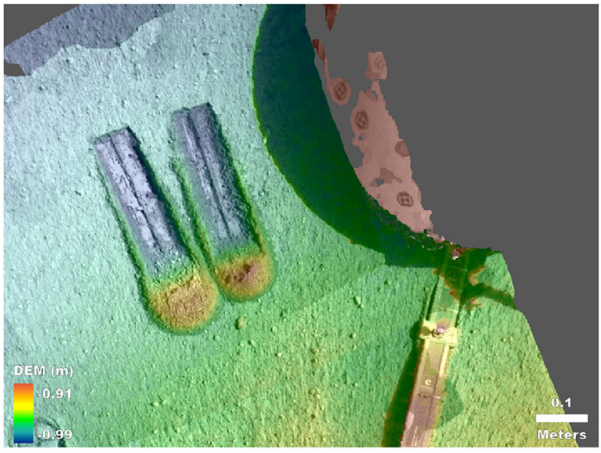

a

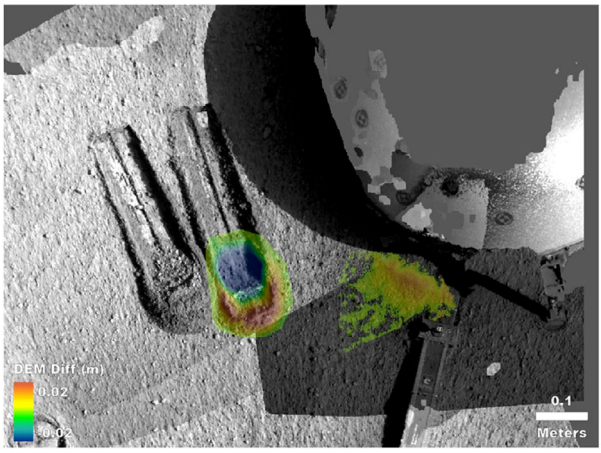

b

Fig. 10 DEMs showing how volumes of scoops and piles were determined. a) IDC DEM produced from stereo pair after scrapes on sols 802 and 803. Note ridges of material on the sides and bulldozed piles at the ends of the scrapes. The slopes of the bulldozed soil piles are between 42°±2.7° whereas the slopes of the walls created by the vertical sides of the scoop are between 54.7°±6.6°. b) IDC differenced DEM from sol 816 (after the scoop) minus sol 803 (before the scoop) showing differences where the scoop removed soil (left) and where soil was added in a pile after the dump (right). The differenced volume of the scoop trough (-214.4 cm^3) minus the scoop ridge (121.5 cm^3) yields a scoop volume of 92.9 ±8.4 cm^3. The increase in volume of the pile on the tether is 61.7±12.3 cm^3. The difference between the volume of the soil in the scoop and the volume of soil in the pile is 31.2 ±20.7 cm^3, which is an estimate of the volume of material dispersed by the wind (∼31% of the scoop). The slope of the pile on the tether is 24.1°± 6.1°

9.4 Volumes and Dispersal of Soil During the Dumps

Six scoops of soil were dumped on the tether from sols 816 to 877 to bury a portion of the SEIS tether within 30 cm of the WTS. Each scoop was preceded by one or more 40 cm long and 5 cm deep scrapes of soil that created piles of soil up to 5 cm high at their ends. All scrapes and scoops were carried out in the area between the WTS and the HP^3 mole (Fig. 10). After creating a pile, the soil was excavated into the scoop (Fig. 11), and the IDA was moved over the WTS or tether and was dumped from an altitude of 45 or 55 cm (Fig. 12). The first two scrapes were carried out on sols 802 and 803 (Fig. 10) and the first scoop and dump were carried out on sol 816 (Fig. 11). The first dump was on the edge of the WTS to cover the portion of the tether closest to the WTS. Figure 12 shows that the soil dumped on the WTS cleaned the dust off as it slid down the side and fell to the ground. Note the soil deposited on the flat edge of the WTS (with screws) and the pile of soil deposited on the ground, in a position corresponding to the length of the cleaned portion of the WTS. The cleaned portion of the WTS is white (its original color) in contrast to the yellowish brown, dusty (Maki et al. 2021) coating elsewhere on the WTS. Adjacent to the cleaned portion

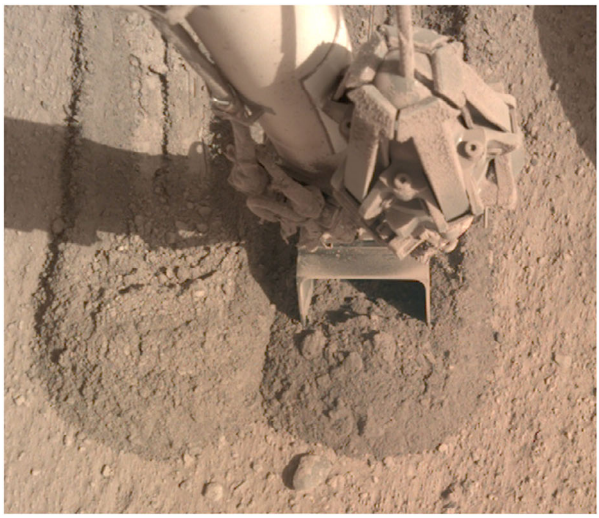

a

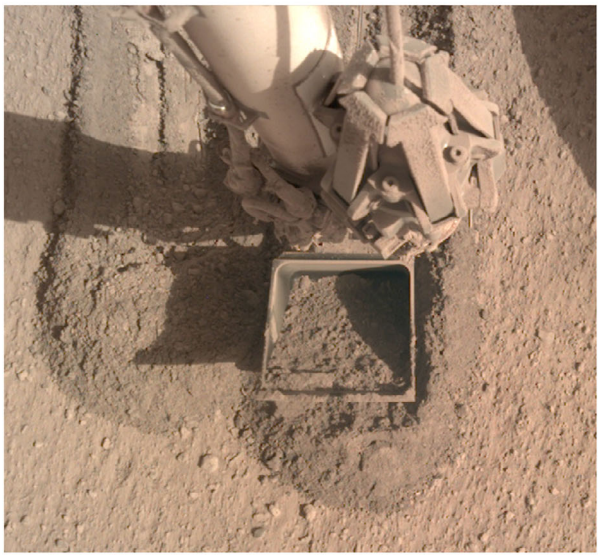

b

Fig. 11 IDC images showing (a) excavating soil into the scoop, and (b) the scoop filled with soil on sol 816. Note clods of soil in the scoop. (a) IDC image D000M0816_668978122EDR_F0000_0900M4. (b) IDC image D000M0816_allowbreak 668978338EDR_F0000_0901M2

of the WTS are darker brown areas covered by the brownish soil that did not dislodge the dust. The dust is composed of fine-grained particles (~1-5 μm) that are suspended and transported in the atmosphere (e.g., Lemmon et al. 2004, 2015) and slowly fall out coating the surface (producing the dusty WTS surface). The brownish soil is composed dominantly of sand size particles (Golombek et al. 2020a; Piqueux et al. 2021) that are too large to go into suspension.

Some soil that was dumped out of the scoop at 55 cm height was dispersed to the west by the wind. Figure 13 shows an image produced by differencing ICC images acquired before and after the first soil dump overlain on the ICC image acquired after the dump (Charalambous et al. 2021a). Dark areas are zones in which dark soil has been added and/or in which light dust has been removed. The differenced image shows a dark semi-elliptical

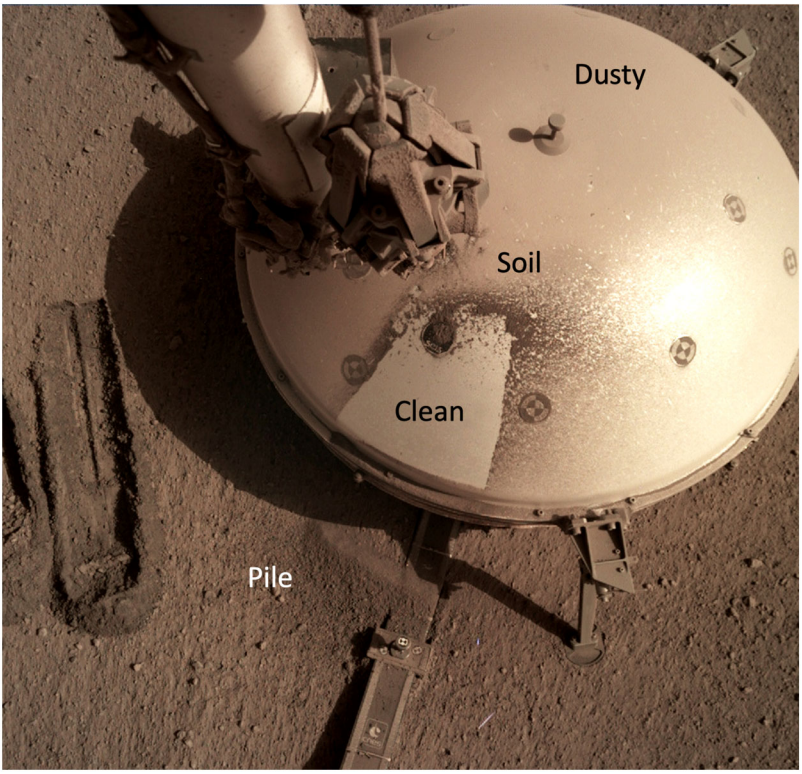

Fig. 12 IDC image of the WTS after the first dump of soil on the SEIS tether on sol 816. Note dusty surface of the WTS (dusty) away from the dump location and that the dust has been removed by the soil (clean). Some of the dark soil has been left on the WTS at the edges of where the dump occurred (soil). Note the scrapes in the soil (left) used to scoop the soil for the dump. The image also shows the SEIS tether (extending to the bottom of the image, with the Pinning Mass post and the end of the IDA and stowed grapple (dusty). IDC image number D001L0816_668979588EDR_F0505_0080M1

area on the ground that extends from the pile of dumped soil adjacent to the WTS about 0.8 m to the west. Small dark spots extend to the south. A light line extends to the west from the WTS leg. Although the wind sensors were not recording during the dump, recent measurements indicated winds were dominantly oriented to the west at this time, so the light line was from soil being blocked by the WTS leg, thereby leaving a light, dust covered line on the surface. Note that dispersal of soil by the wind was also observed on sol 417, when residual soil in the scoop was dumped onto the surface near the HP^3 mole. Differenced ICC images showed a dark streak that extended >1 m to the southwest, a direction in agreement with measured winds of $\sim$10 m/s from the northeast.

The volume of soil in the scoop and in the pile was determined by co-registering and differencing before and after IDC DEMs. However, before and after DEMs contain small vertical offsets and tilts relative to each other, in addition to true changes in surface shape. To isolate true surface volume changes, the regions encompassing surface changes for each activity were individually outlined in a map-projected geographic information system (GIS). A buffered zone of 10 cm was defined around each outlined region where no surface changes occurred, and the buffers were locally trimmed to exclude portions of DEMs that contained significant artifacts such as at image seams, shadow boundaries, and the tall Pinning Mass.

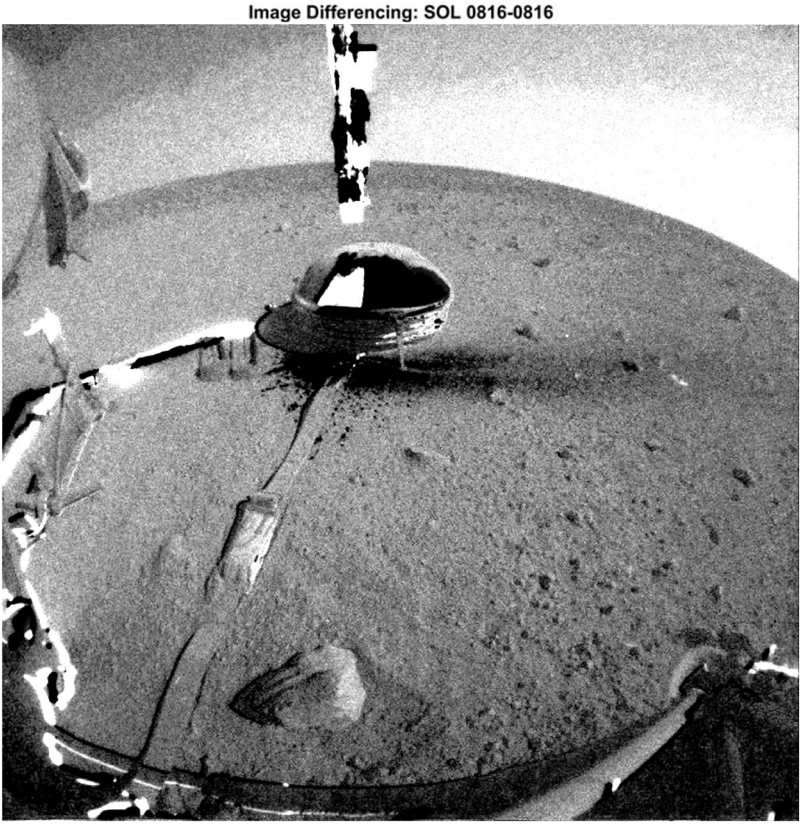

Fig. 13 Image of the workspace created by differencing ICC images acquired before and after the first soil dump on the tether on sol 816 overlain on the sol 816 ICC image. The white area on the WTS is where the dust has been removed by the soil that was dumped on it and slid to the ground. The dark areas are where dark soil has been deposited (pile and WTS). Notice dark area to the right is where soil has been dispersed by the wind. These dark areas are produced by either dark soil being deposited on the surface and/or where soil has impacted the surface and removed the bright dust. The long axis of the darkened area on the surface is ~0.8 m. ICC images are looking south, so areas to the right are to the west, so the soil was entrained and dispersed by winds from the east to the west. Note small individual dark spots on the surface south of the WTS are 1-2 mm in diameter

DEM elevations within the buffered zones were subtracted (after – before), and a two dimensional linear regression was performed on that uncorrected DEM difference to calculate the artificial planar tilt between them. This calculated tilt was then subtracted from the uncorrected DEM difference to produce a corrected volume change map. For each scrape, scoop, or pile, the positive-valued pixels were integrated to produce the total volume gained in raised portions of the surface, primarily at ends of scrapes, edges of scoops, and piles on the tether. Similarly, the negative-valued pixels were integrated to produce the total volume removed mostly in the troughs produced by the scooping. The difference between these integrated volume gains versus integrated volume losses is a measure of the net volume change resulting from material being excavated into the scoop. Comparing a scoop's volume with the volume of the pile yields the volume of material dispersed by the wind. Errors were empirically estimated by performing similar positive-pixel versus negative-pixel integrations

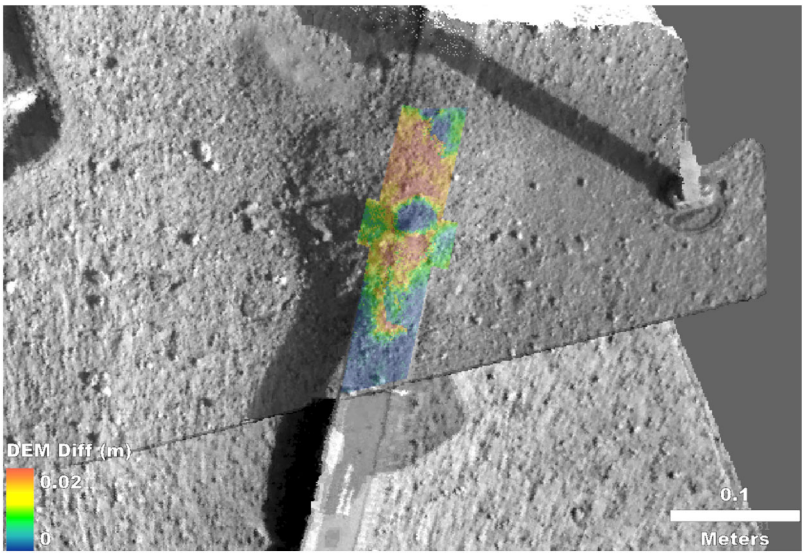

Fig. 14 IDC differenced DEM (sol 877 minus sol 788) showing soil deposited on the SEIS tether after six dumps. Note circular blue spot in the middle of the tether length is an artifact over the pinning mass. Smoothing out that artifact indicates that 93% of the measured area of the tether is covered by 1 cm, 69% is covered by 1.5 cm, 50% is covered by 1.75 cm, and 30% of the tether is covered by 2 cm of soil

in the surrounding unaffected buffered zone, which if perfectly aligned should be zero, and scaling those values by the ratio of areas for each activity's outline versus its surrounding buffer. Due to the effectiveness of the applied correction for offsets and tilts, the differences between any respective positive versus negative noise estimate was ≤ 1 cm^3, so they are reported here as a single $\pm$ value. The errors are generally around 10%.

Figure 10a shows the DEM produced after the scrapes on sols 802 and 803. Differencing this DEM with a DEM produced after the scoop and dump using the method described, shows the changes in surface topography (Fig. 10b). During the motion to excavate soil into the scoop (Fig. 11), the scoop dug down below the surface creating a depressed trough surrounded by a ridge on three sides (Fig. 10b). By differencing the volume of the scoop trough (-214.4 cm^3) and the scoop ridge (121.5 cm^3) results in a scoop volume of 92.9 ± 8.4 cm^3 (Fig. 14). Figure 11b shows that the scoop is partially filled with soil (a full scoop holds $\sim$250 cm^3). The volume of the pile dumped on the tether, obtained by subtracting the post dump DEM from the pre-dump DEM, is 61.7 ± 12.3 cm^3 (Fig. 14). The difference between the volume of the soil in the scoop and the volume of soil in the pile is 31.2 ± 20.7 cm^3, and provides an estimate of the volume of material dispersed by the wind ($\sim$31% of the volume of soil in the scoop). It is possible that the porosity of the soil in the surface pile is higher than that in the scoop due to additional air pockets produced from dumping. If so, this might slightly increase the volume of dispersed soil. The average thickness of the dispersed soil if deposited uniformly over a half ellipse with axes of 80 cm by 10 cm is 124 μm. The average thermal inertia of the surface is 185 J m^{-2} K^{-1} s$^{-1/2}$, which corresponds to fine to very fine sand size particles $<$140 μm (Piqueux et al. 2021). As a result, the volume of dispersed soil could be a uniform layer of less than 1 fine sand grain thickness. However, the pixel darkness (Fig. 13) varies from around 50% (close to) to around 15% (far from) the darkness of the pile of soil, suggesting that the thickness of soil varies by a factor of three. This suggests the layer thickness is much less than the diameter of one sand particle at the far edge of the

Table 5 Tether scoop and burial pile volumes

Sequence #/Target/Hit Date (UTC/Sol)	Sol of scoop and dump	Scoop volume cm^3	Pile volume cm^3	Dispersed volume cm^3	Dispersed percentage %
1/A/A 2021-03-14	816	92.9 ±8.4	61.7 ±12.3	31.2 ±20.7	33.6
2/A/A 2021-04-18	850	86.8 ±8.3	56.9 ±16.1	29.9 ±24.4	33.4
3/PM/C 2021-04-24	856	83.7 ±10.5	65.3 ±6.7	18.4 ±17.2	22.0
4/PM/PM 2021-05-01	863	118.7 ±12.2	64.4 ±25.6	54.3 ±37.8	45.7
5/PM/PM 2021-05-08	870	78.4 ±9	65.5 ±9	12.9 ±18	16.5
6/PM/PM 2021-05-15	877	103.4 ±10.2	75.7 ±7	27.7 ±17.2	26.8

half ellipse, which would require that individual particles are spaced out by a factor of 3 at the far end.

The first four soil dumps on the tether occurred in the mid to late afternoon at 15:00 to 17:00 local mean solar time (LMST) when winds (e.g., Banfield et al. 2020; Baker et al. 2021) were dominantly from the east-northeast with moderate to low speeds of 1-5 m/s (Fig. 15). This was done to minimize the soil dispersed by the wind and to concentrate the soil on the pile burying the tether. The dispersal of soil during these dumps was generally similar to that observed during the first dump ($\lesssim$1 m long). The last two tether burial dumps were moved to 11:20-11:30 LMST when winds were expected to be higher and from the east-southeast. These dumps occurred with winds of 5-10 m/s from 140°-160° azimuth (measured clockwise from north) and produced much larger dispersion of soil ($\sim$1.5-2 m long) towards the west-northwest (Fig. 15). This was done to see if the soil dispersion scales with the wind speed, which it clearly does. In addition, it confirmed that the azimuth of the observed dark ellipses produced by the dispersion of soil is always downwind from the measured wind direction.

The volumes of soil scooped, piled on the surface, and dispersed are shown in Table 5. Scoop volumes varied from $\sim$78 cm^3 to 119 cm^3. Scoop volumes during solar array cleaning experiments (Sect. 10) varied from 86-156 cm^3. Volumes of piles on the tether varies from 56 cm^3 to 76 cm^3. Dispersed soil volumes varied from 12 cm^3 to $\sim$55 cm^3, and averaged about 30% of the scoop volume. The largest dark area due to soil dispersal occurred on the 5th dump, which covered an area of $\sim$2 m by 0.4 m. For the dispersed soil volume of 12.9 cm^3, the average thickness of soil would be $\sim$10 µm. Given that this is about 14 times less than the average particle diameter, individual fine to very fine sand grains must be substantially dispersed, suggesting that individual sand grains darken a much larger area than their intrinsic size. After all six soil dumps, the thickness of soil on top of a little more than a 20 cm length of the tether was measured by differencing DEMs before and after all of the dumps (Fig. 14). Results indicate that 93% of the measured area of the tether is covered by $>$1 cm, 69% is covered by $>$1.5 cm, 50% is covered by $>$1.75 cm, and 30% of the tether is covered by at least 2 cm of soil.

A numerical model was developed to estimate the dispersion of soil by the wind shown in the differenced ICC images (Verdier et al. 2023). The effects of gravity, buoyancy and wind drag on the particles was implemented in a computational fluid dynamics model. The drag from the wind should carry finer and lighter particles farther than larger and heavier ones. Model simulations show that for a one-meter drop, particles transported by the wind range from 200 to 100 microns (i.e., fine sand) in winds of about 5 m/s, which agrees with thermophysical estimates of the dominant particle size of the soil.

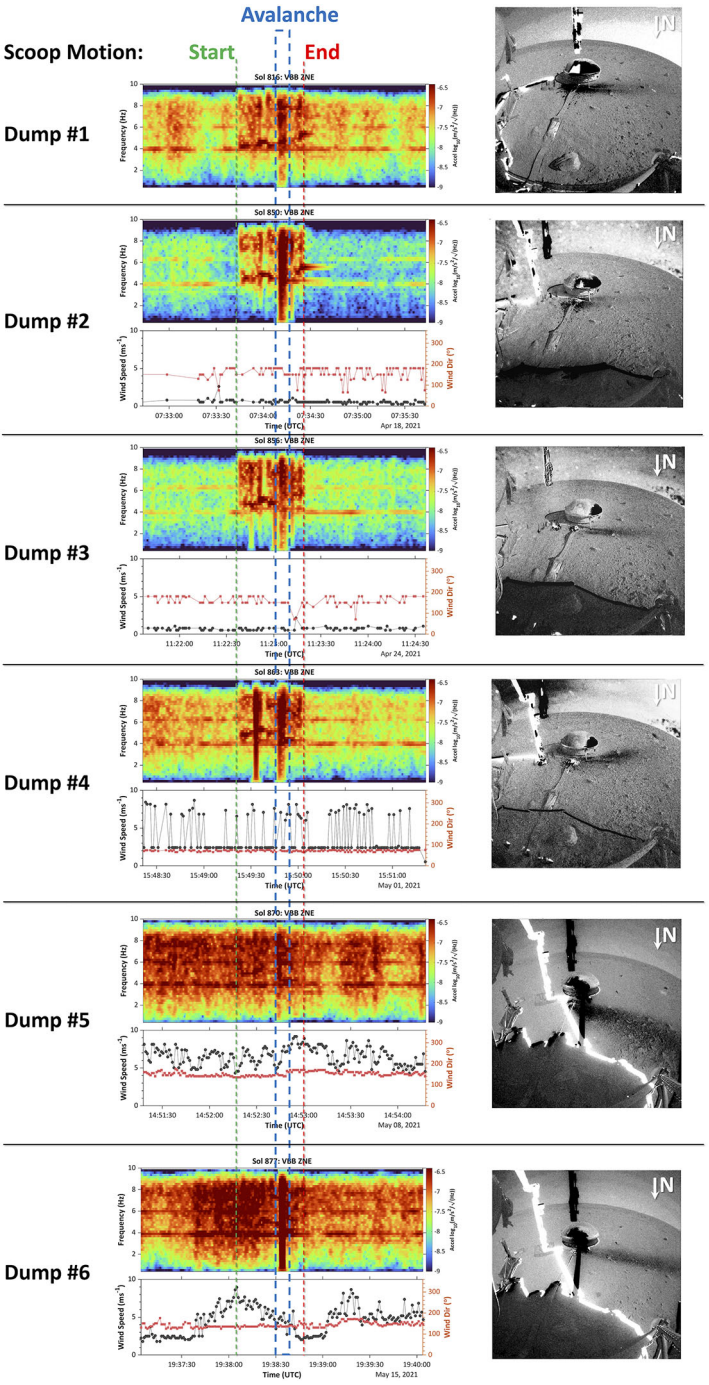

Fig. 15 Summary of six tether burial dumps showing SEIS acceleration frequency response with the start, end and main avalanche indicated, wind speed and direction, and before-after differenced ICC images showing darker areas of the pile and dispersed soil

9.5 Soil Mechanics Properties from Tether Burial Activities

The IDA scraping activities created several piles of regolith as well as walls parallel to the direction of the scrapes on the relatively flat ground surface that can be used to investigate soil mechanical parameters (Marteau et al. 2022, 2023). Elevation profiles were extracted from the digital elevation models obtained between sols 803 and 822 to measure the slopes of the walls and piles formed by scraping and the piles formed by dumping (e.g., Fig. 10). The slopes of the bulldozed soil piles produced by the scrapes are between 42°±2.7° while the walls scraped by the vertical sides of the scoop have slopes of 54.7°±6.6°. At its highest point, the dumped pile on the SEIS tether is ∼3 cm high and the material rests at slopes of 24.1°± 6.1°. The difference in slope angles between the scraped and dumped piles are likely due to the different ways the piles were created. The slope value of 24.1° obtained from the dumped pile is interpreted as a lower bound estimate of the internal friction angle of the soil in a loose state while the value of 42° obtained from the scraped piles corresponds to the internal friction angle of the soil in a denser (remolded) state. In addition, the slopes of the walls left by the scoop's scrapes are larger than the slopes of the piles and slope failure was not observed on these walls. This result can be explained by the presence of some cohesion in the undisturbed soil, which is consistent with the cohesion values reported in Marteau et al. (2021) and Spohn et al. (2022b).

9.6 Burial Results on Glitches

Despite an apparent reduction of the number of glitches per sol at the beginning of the burial activities, the glitches continued to increase in frequency until reaching a maximum near sol 970, well after burial activities were over. As a result, the burial did not produce a major reduction in glitches. Possible reasons include: only a small portion of the tether near SEIS was buried, the soil was not thick enough to attenuate thermal contractions, stresses generated in the non-buried part of the tether were transmitted to the SEIS, and some of the glitches originate within the Sensor Assembly and the Load Shunt Assembly, which were unaffected by the burial of the tether.

10 Solar Array Cleaning Experiments

10.1 Introduction

The InSight lander is equipped with two solar array wings, each roughly 2.2 m in diameter (Fig. 1), and populated with a 5.16 m^2 total area of triple junction solar cells. During Sol 4 on L_s 298, telemetry showed a total peak power capability of around 710 W. The integration of this power telemetry curve over the daytime period of the sol resulted in an estimate of roughly 4750 W hrs of energy collection capability at that time (Fig. 16). After a full martian year, on sol 668, this capability had declined to 190 W and 1088 W hrs, respectively. As of sol 1337, two martian years after landing, this capability had dropped to 69 W and 400 W hrs (roughly 10%), respectively, with the power drop roughly following an exponential (Fig. 16).

From an energy production perspective, both the atmospheric dust opacity (tau) and the accumulated dust on the array (dust factor) combine to limit the total solar irradiance the arrays see on any given sol. Tau, a measure of the amount of dust in the atmosphere (Sect. 3.2), limits the irradiance that reaches the surface and alters the ratio of the direct and diffuse contributions of that irradiance. The dust factor is derived by multiplying the input solar

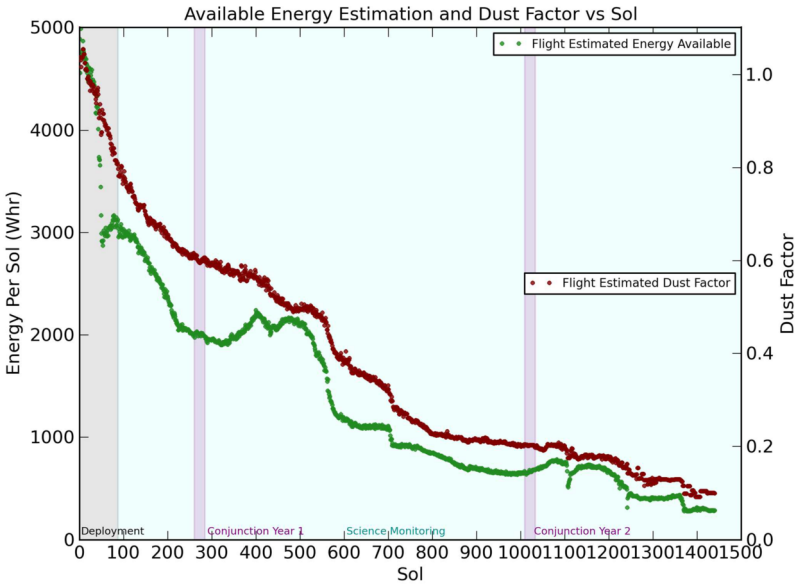

Fig. 16 Plot of energy generated per sol (green) and the dust factor (red) versus time (sol) of the InSight lander. Power decreased exponentially and the dust factor worsened by ∼90% in the roughly 2 Mars years of the mission (1442 sols). Increased rates of change in dust factor (and power production) correlate with periods of higher atmospheric opacity associated with dust storms

irradiance reaching the cells by a loss factor, a value generally between 0 and 1 that limits the amount of that remaining direct and diffuse irradiance the cells receive. The dust factor is derived from a model of the power system based on ground testing data that includes different amounts of dust on the panels and illuminations from various angles. The dust factor is plotted in Fig. 16 and also follows a generally exponential decay from 1 immediately after landing to around 0.13 (13%) on sol 1337 after nearly 2 Mars years.

Changes in the rate of power decay can be most closely correlated to the amount of dust present in the local atmosphere, which controls the rate at which dust falls into the arrays. Observations indicate that the greater the amount of dust in the local atmosphere, the higher the rate of decay of the dust factor with significant drops after sols 50, 550, 710, 1110, and 1250 (Figs. 16 and 17). The amount of dust on the spacecraft has increased through time. Figure 18 show spacecraft selfies obtained on sols 10 and 1211. The deck and solar arrays are almost completely obscured by sol 1211, which corresponds to the 90% drop in power over that time. Close up IDC images of the calibration target obtained on sol 12 and 1238 shows the targets are almost completely obscured by dust at the later sol (Fig. 19).

A variety of ideas were considered by the InSight project to increase power production by removing dust from the solar panels, but most were not feasible or considered to be unlikely to be effective. Some of the ideas considered included using existing hardware such as the IDA and motors to shake the array in an effort to dislodge dust, as well as more drastic ideas such as pulsing the descent engines to shake the entire lander. Pulsing the descent engines was not pursued due to the risk of using hardware that had been exposed to cold temperatures, and the large amount of energy needed to heat the propellant lines and tanks. The IDA could reach the corner of the east array with the tip of the scoop and pluck it, but carefully moving the arm into position would have been difficult and taken a long time, and any resulting shaking of the panel was considered unlikely to dislodge the dust. One

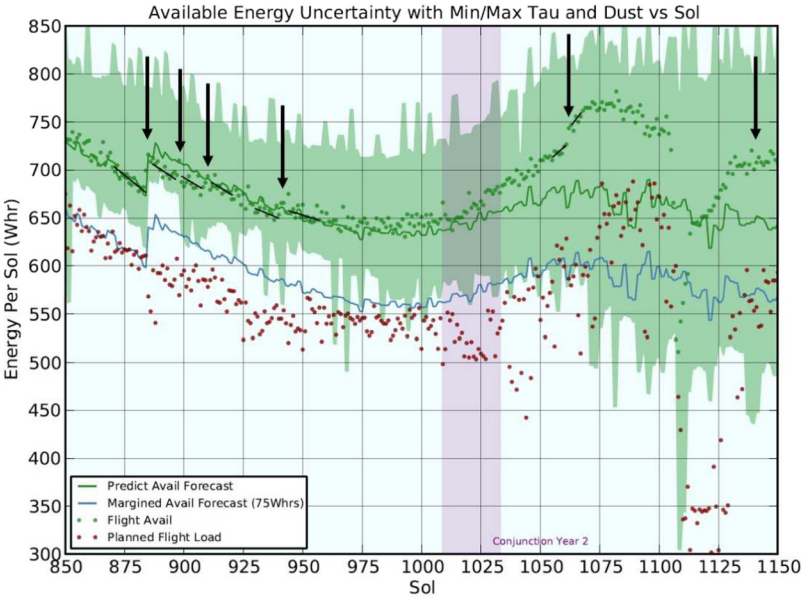

Fig. 17 Plot of InSight energy from sol 850 to sol 1150 with the first six solar array cleaning experiments marked (black arrows). The energy low centered around sol 975 is near aphelion and conjunction (in purple) when the spacecraft was out of communication with Earth. The green shaded region is the power expected bounded by maximum and minimum atmospheric opacity based on the compilation of previously measured and extrapolated tau developed for InSight (Lisano and Bernard 2014). The green dots are the energy per sol produced by the solar cells. The green line is the modeled energy produced by the spacecraft. The red dots are the energy per sol planned to be used by the spacecraft. The blue line is the modeled margined energy provided to the operations team for planning and is 75 W hrs below the modeled energy. Black lines show trends in energy per sol on either side of the first five solar array cleaning events to emphasize the jumps in energy. The largest increases occur from the first and fifth cleaning experiments. More modest increases occur at the others

idea that was implemented on the lander was pulsing the solar array deployment motors as quickly as possible. These motors had only been used on sol 0 during initial solar array deployment right after landing. They could be commanded on and off, but only as fast as once every 0.5 s. During initial deployment, the motors pulled a tape that is connected to one of two panels of the array, moving the panel to unfurl the array until it is latched into position. In this deployed state, the same motors could only provide a small torque about the central (vertical) axis of the array. The solar array deployment motors were pulsed on the east array on Sol 789 with the IDC pointed at the array to collect images during the event. While there was noticeable movement of the array observed in the images, there was no change in solar array output. A second attempt was done on the west array on sol 915. There were two shakes, each lasting about a minute separated by around 7 minutes starting at 11:32 LMST. Winds were relatively high (7-14 m/s) during the shakes. Images acquired before and after the shakes showed no differences and there was no perceptible change in power from either solar array. These negative results were not entirely unexpected given that very high winds are required to lift very small dust particles into motion (see Sect. 7; Charalambous et al. 2021a; Baker et al. 2021).

The rationale for using dispersed sand during soil dumps adjacent to the solar panels to try to clean the solar panels of dust grew out of the observed dispersion of soil and darkening

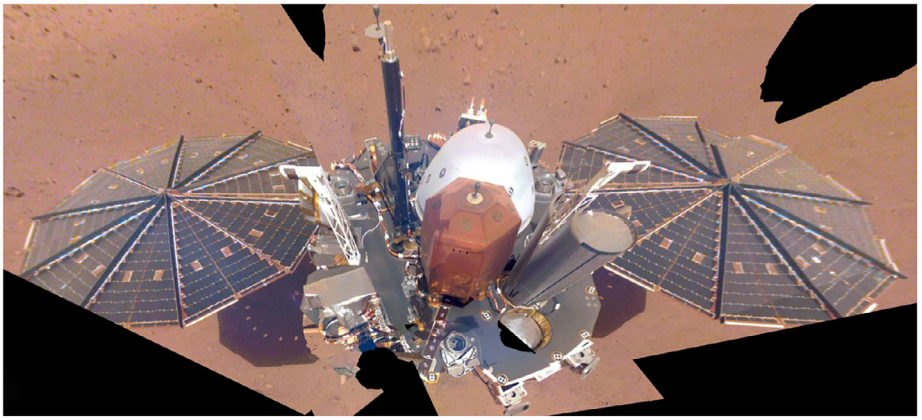

a

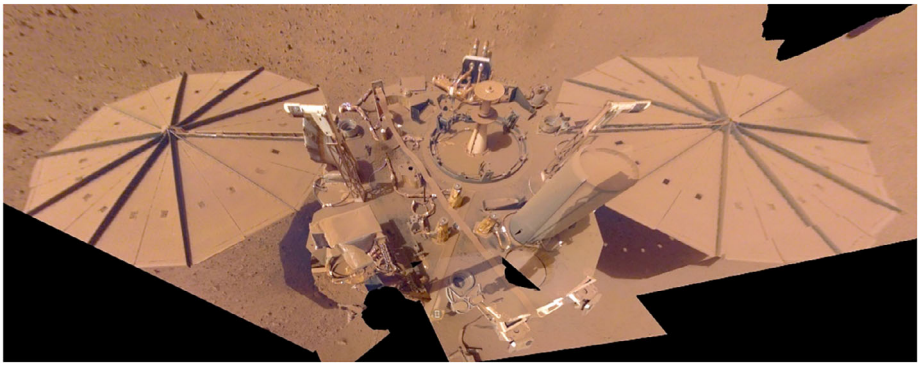

b

Fig. 18 Lander selfies acquired after landing on sol 10 (a) and near the end of the mission on sol 1211 (b) showing the dust that has accumulated on the lander and solar panels over 2 Mars years on the surface. The energy from the solar panels had decreased to about 10% of that at the start by the end of the mission. Note instruments on the deck for (a) and not for (b) and the piles of soil on the northwest portion of the deck from the solar array cleaning experiments

of the surface during the tether burial dumps (Sect. 9.4). After careful review, it was decided to see if sand particles dispersed by the wind during a dump hit the solar panel, lifting the dust off the panel and into suspension in the atmosphere, improved solar array power. This section of the paper includes a review of the lack of natural cleaning events, the rationale for the cleaning experiments, the results of the seven solar array cleaning experiments, and science observations from them.

10.2 Background

10.2.1 Landing Site Thermophysical Properties

During landing site selection, it was recognized that the InSight landing site would be a relatively dusty location (Golombek et al. 2017). The global thermophysical properties of the InSight landing site are generally similar to the Viking, Spirit, Phoenix, and Curiosity landing sites with moderate thermal inertia and intermediate to relatively high albedo (Golombek

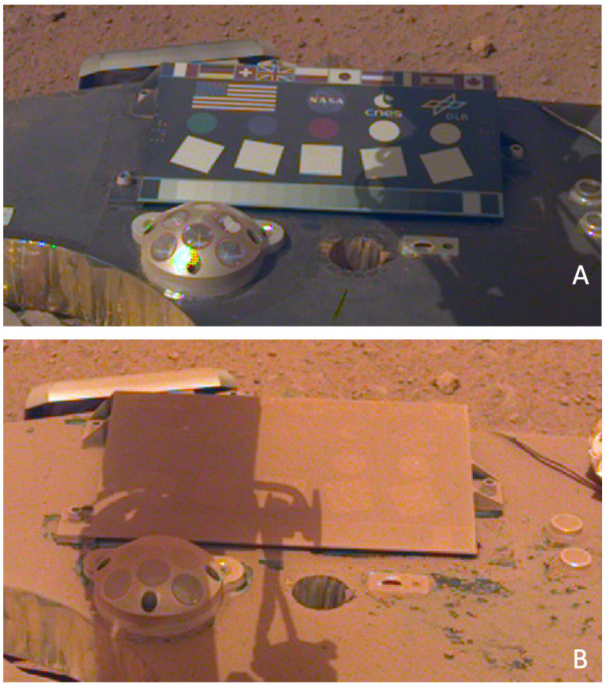

Fig. 19 IDC images of the calibration target on sol 12 (A) and sol 1238 (B) showing the accumulation of dust over the mission that almost completely obscured it

et al. 2008). The thermal inertia and albedo of the InSight landing site is most similar to the Viking Lander 2 (VL2) site, which has slightly higher albedo and slightly lower thermal inertia than the Viking Lander 1, Spirit, and Curiosity landing sites (Golombek et al. 2017), which has been attributed to more dust and drift deposits (Golombek et al. 2008). The InSight landing site has relatively high albedo of 0.24 in TES at 7.5 km/pixel (Christensen et al. 2001) and 0.25 in infrared (IR) thermal mapper (IRTM) at 60 km/pixel (Pleskot and Miner 1981), which argues for a thin coating of dust similar to the VL2 landing site and dusty portions of the Gusev cratered plains (Golombek et al. 2005). The InSight and VL2 landing sites also both have dust cover indices (DCI, given by the high wavenumber emissivity in TES thermal IR data) of 0.94, due to thin surface coatings of dust (Ruff and Christensen 2002). Although the relatively dusty nature of the landing site raised concerns about dust coating the solar arrays as has been observed in all other solar powered missions (e.g., Lorenz et al. 2021b), InSight incorporated larger and higher efficiency solar arrays during development and simulations showed that the lander would last the required one Mars year under worse case tau conditions from an almanac of atmospheric opacity (Lisano and Bernard 2014), even without cleaning events of the type observed by Spirit and Opportunity (Stella and Herman 2010; see next section).

10.2.2 Dust Removal via Dust Devils

Analysis of the recurrence intervals of dust devils near the InSight landing site from HiRISE images suggested that they would be much less frequent than those that likely affected the Spirit rover at the Gusev cratered plains (Reiss and Lorenz 2016). The coincidence of array cleaning events on the Spirit rover with the onset of visual observations of dust devils, and the overall frequency of cleaning events was consistent with the predicted encounter rates

(based on Pathfinder and Phoenix pressure data) of vortices that were intense enough (as judged from laboratory experiments with a vortex generator) to lift dust from smooth metal surfaces (Lorenz and Reiss 2015). This provided strong evidence, for what was already a widely-held suspicion, that dust devils were the primary agent of array cleaning.

Although there are important physical differences, it is obvious that the processes of removing dust from a spacecraft surface such as a solar array, and removing it from the ground to form a dark 'track,' have some similarities, and thus the rate of occurrence of one might inform the rate of occurrence of the other. Some differences may relate to the role of 'sandblasting' in facilitating dust removal from a mixed-particle regolith versus lifting of uniform dust, and the possibility that 'backventing' (the so-called 'delta-Pressure effect') from a porous regolith might similarly dislodge dust on the ground that might otherwise adhere to an impermeable surface like a solar array (with possible electrostatics). These distinctions notwithstanding, Reiss and Lorenz (2016) noted that the area generation rate of dust devil tracks at Elysium (as judged from change detection on orbital images) was about an order of magnitude lower than that at Gusev, and thus that if the interval between solar array cleaning events were correspondingly longer, InSight would only see cleaning events once every decade or so. The track generation rates (which are seasonally-variable) estimated by Reiss and Lorenz (2016) were substantiated and refined after InSight's landing by Perrin et al. (2020).

The dust accumulation on the InSight arrays was essentially unremitting (Lorenz et al. 2021a), with only one or two detectable cleanings of the order of 1% (e.g., Figs. 16). This is in stark contrast to the quasi-regular 30% cleaning events seen on Spirit and Opportunity's solar panels (Stella and Herman 2010), and on optical sensors on Curiosity (Vicente-Retortillo et al. 2018; Lorenz et al. 2021b). One speculation has been that stronger background winds cause shear that suppresses the formation of the largest, most intense vortices which are responsible for the majority of dust lifting. This is supported by the increase in power law slope of the vortex pressure drop (a measure of intensity) in the InSight population measured by the meteorology instruments compared with other missions (e.g., Banfield et al. 2020), and in the character of the dust devil tracks at InSight compared with Gusev. These are both narrower (suggesting an absence of large vortices) and straighter (suggesting advection dominated by background winds) (e.g., Spiga et al. 2021; Chatain et al. 2021) in contrast with the cycloidal, meandering tracks often seen at Gusev.

The relatively small dust devil track generation rate and absence of array cleaning events is mirrored by the lack of visually observed dust devils. While vortices detected by InSight's meteorological and seismological instrumentation are abundant (in the thousands), it is striking that no active dust devils have been detected in imaging from the lander (Lorenz et al. 2021a). Dust lifting has not been completely absent, as a couple of transient shadows of the order of 1% darkening have been detected in solar array data contemporaneous with vortex pressure drops and before and after surface images show some new dust devil tracks (Banerdt et al. 2020; Charalambous et al. 2021a), suggesting some occasional nonzero dust loading, but dust lifting seems overall to be very rare and/or weak.

10.3 Rationale for Cleaning the Solar Arrays with Dispersed Sand

10.3.1 Introduction

Common components of soils on Mars are sand size grains and dust (Christensen and Moore 1992; Golombek et al. 2008). Sand size grains, by definition (Kuenen 1960; Krinsley and Smalley 1972), are 0.0625 mm to 2 mm in diameter and form the bulk of the surface layer on

Mars (~1 m thick). Microscopic imagers on Phoenix, Mars Exploration Rovers, and Mars Science Laboratory found that sand on Mars is typically 0.08 to 0.2 mm in diameter with equant to very equant, sub-rounded to very rounded grains that are basaltic in composition (Yen et al. 2005; Goetz et al. 2010; McGlynn et al. 2011; Minitti et al. 2013; Ehlmann et al. 2017; Weitz et al. 2018). McGlynn et al. (2011) and Golombek et al. (2018b, 2020d) argue that the size-frequency distribution, equant shape and rounding of sand is produced by meteorite impact and aeolian activity.

Dust is very fine grained (~1-5 μm) (e.g., Lemmon et al. 2004, 2015) and appears bright reddish (Maki et al. 2021), in contrast to the dark sand and is composed of slightly chemically altered basalt (Goetz et al. 2005; McGlynn et al. 2012; Berger et al. 2016; Achilles et al. 2017; Ehlmann et al. 2017). Wind moves dust via suspension in the atmosphere, in contrast to sand, which moves via saltation (e.g., Greeley and Iversen 1987; Greeley et al. 1980; Sullivan et al. 2005, 2008). Because of the low atmospheric density and low gravity, high winds are needed to move sand by saltation and the optimal grain size to overcome the threshold friction is around 0.2 mm (Greeley and Iversen 1985; Charalambous et al. 2021a; Baker et al. 2021). The friction of the wind moving across the surface with a particular roughness requires a minimum wind speed to mobilize a sand grain. However, very fine-grained dust requires higher wind speeds to lift them into suspension, so the impact of saltating sand has been invoked to kick dust particles into the atmosphere (Iversen et al. 1976; Greeley and Iversen 1985, 1987; Greeley 2002).

The smooth plains surrounding the InSight lander have few aeolian bedforms that are mostly near relatively fresh impact craters (Golombek et al. 2017, 2018a, 2020a). These bedforms are bright, suggesting a surface layer of dust and relative inactivity, and a surface that is mostly in aerodynamic equilibrium without much active sand motion (see also Sects. 6 and 8). This along with the paucity of dust devils may be responsible for the high dust build up on InSight's solar panels since landing. The observation that all aeolian changes detected from the lander occurred during the passage of daytime convective wind vortices (Charalambous et al. 2021a; Baker et al. 2021) is also in agreement with the lack of removal of dust.

When soil is dumped in the atmosphere above the surface (~50 cm for the tether burial), it provides a means for the sand to be entrained and dispersed by the wind without having to overcome the threshold friction wind speed. Dispersion of sand was also observed by the Phoenix spacecraft in images that recorded individual grains dropping at ~1 m above the ground at up to 70° from vertical from the end of the scoop (Holstein-Rathlou et al. 2010). The dispersion of particles is dependent on the atmospheric drag forces compared to gravity and the transport likely depends on particle size. The basis for trying to remove dust from the solar panels using dispersed sand is that the sand would be dumped adjacent to the solar panels and the wind would blow some of the sand sideways such that when the particles hit the surface, they would kick the dust into suspension, which would reduce the amount of dust on the panel and improve the power produced.

In order for this process to work, individual sand grains must both kick the dust into suspension when they impact the surface, and clean an area of dust that is larger than their diameter. The latter is required because the sand grain would likely eventually come to rest on the panel, blocking sunlight and reducing power production. Several lines of evidence argue that individual sand grains striking a dusty surface remove dust from a substantially larger area than their intrinsic area. The estimates of soil volume in the scoop and darkened area to the west of the soil dumps over the SEIS tether (e.g., Fig. 20) suggest that more area is darkened than covered by a layer of soil one sand particle thick (assuming sand is ~140 μm in diameter as indicated by the thermal inertia) (see Sect. 9). This suggests that

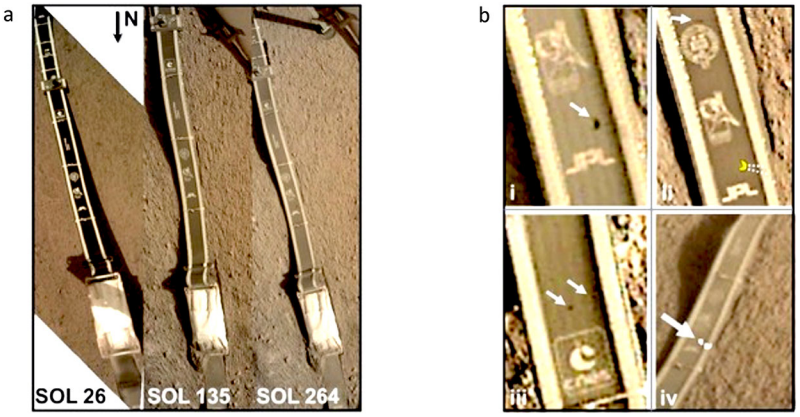

Fig. 20 IDC images of the SEIS tether from Charalambous et al. (2021a). (a) Shows the change in color and accumulation of dust on the tether from sol 26 to sol 135 to sol 264. (b) shows close ups of dark spots on the tether. Individual dark spots (white arrows) are ∼1-2 mm in diameter. A crescent shaped dark spot (yellow) is 0.5 mm by 2.5 mm with rays extending to the southeast, consistent with saltation in the measured wind direction. (b iv) ICC images were differenced between sols 234 and 237 to show the pixels (white) that have changed

individual sand particles remove more dust over a greater area than their size to darken the surface. IDC images of individual dark spots north of the WTS show these spots are roughly 1-2 mm in diameter (Fig. 20), so if they were produced by individual sand grains, the area of the dark spot is of order 100 times larger than the area of a 140 μm sand particle. Finally, individual dark spots ∼1-2 mm diameter on the tether are roughly circular and thus most likely produced by a single sand grain impacting the tether (Fig. 20). These observations argue that a single sand grain ∼140 μm in diameter clears an area covered with dust that is of order 100 times larger. If the dusty areas are produced by a mono layer of individual dust grains 4 μm in diameter, one sand grain removes around 80,000 dust particles. If the dusty areas have two or three layers of dust, the number of dust particles removed would increase to 160,000 to 240,000. These calculations indicated that impacting a dusty surface with sand grains dispersed by the wind (or entrained in wind vortices) could be a very effective tool to remove dust.

10.4 Solar Array Cleaning Experiments

Seven solar array cleaning experiments were carried out by InSight. All included scrapes of soil from the area between the WTS/SEIS and the HP^3 mole. The first four were carried out on sols 884, 897, 911, and 939 prior to the local minimum in expected power centered near sol 975 when Mars was near aphelion and which included conjunction (ending around sol 1030) (Fig. 17). The goal of these cleaning experiments was to improve power sufficiently to keep the SEIS Very Broad Band (VBB) sensors on continuously during this low power period. The first six cleaning experiments were done with dumps of soil on the northwestern side of the spacecraft deck with winds from the east dispersing soil towards the solar panel to the west. The fifth (sol 1061) and sixth (sol 1143) solar array cleaning experiments were done after conjunction before the substantial decrease in power predicted near sol 1225 (Fig. 16). The goal of these two cleaning events was to improve power sufficiently to keep the VBBs on continuously during the seismic quiet period (sols 750 to 1200), when most

Table 6 InSight solar array cleaning experiments

Sol Cleaning event #	Scoop volume cm^3	Wind speed Main avalanche mode & range m/s	Wind direction °clockwise from north	Dispersion: length (m), direction	Portion on solar panel	Instantaneous energy improvement W hr sol^{-1}
884 1st	112.6 ± 10.4	9, 6-13	120-140	$\gtrsim$1-2 NW	All	24
897 2nd	86.2 ± 10.7	10, 6-14	90 or 130	~1 W, NW	All	6
911 3rd	142.8 ± 14.9	7, 2-14	130-170	~1-2 NNW	Third	6
939 4th	101.5 ± 18.8	9, 6-12	140-150	~2-3 NNW	Little	3
1061 5th	155.6 ± 19.1	14, 10-18	100-130	$\gtrsim$1 W	Most	15
1143 6th	135.2 ± 26	1 or 6, 1-8	175, 60	Little SW	Some	7
1238 7th	99.1 ± 15.3	N/A	N/A	Very Little	Very Little	0

Wind speed and direction are from where the winds are coming from. Wind sensor data not available (N/A) during the 7th cleaning experiment. Wind speed reported for the main avalanche

marsquakes were detected (e.g., Giardini et al. 2020). The seventh solar array cleaning experiment dumped soil between the southeast side of the spacecraft deck and the east solar array on sol 1238 before power deceased below the level needed to move the IDA.

Data acquired for each experiment included ICC images and IDC images of the scoop during the scooping of the soil and before and after each dump. TWINS (Temperature and Winds for InSight) wind speed and direction before, during and after the dump were acquired for all but the 7th cleaning attempt. IDC stereo images of the scooped area soil was excavated were used to estimate the volume of the scoop using the same method for the tether burial dumps (Fig. 10). Before and after IDC stereo images of the lander deck, where the dump occurred and before and after images of the solar array were also acquired (although IDC images only covered the eastern edge of the western solar array because of hard stops in the IDA), along with before and after ICC images. Image differencing techniques (Charalambous et al. 2021a) were used to show darkened areas. The timing of the dumps was informed by recent wind direction and speed, although this was increasingly supplemented by the previous year's wind data at the same L_s, due to the increasing limitations on TWINS measurements as power decreased (e.g., Banfield et al. 2020). Many of the dumps also included SEIS VBB data (Lognonné et al. 2019). One further method used to deduce the ideal time window containing peak wind speeds during the day was comodulation. This technique allowed estimations of the daytime wind speeds based on correlations with the ground acceleration induced by the wind and measured continuously by the seismometers (Charalambous et al. 2021b). These predictions were validated from wind measurements taken in nearby sols. A summary of sol, scoop volume, wind speed and direction, dispersed soil length and direction, portion of the dispersed soil on the solar panel and power improvement are included in Table 6.

The first solar array cleaning experiment was conducted on sol 884. A fairly full scoop of soil (~112.6 ± 10.4 cm^3) was dumped on the northwest portion of the lander deck at ~11:40 LMST when strong winds were expected to be from the southeast with dispersion of soil expected onto the western solar panel. The dump of soil was from an elevation of about 35 cm above the lander deck. A portion of the solar array to the northwest of the dump site was visibly darkened and fitting an ellipse to this darkened area suggests soil was dispersed about 1-2 m towards the northwest (Fig. 21). An IDC image of the soil dumped on the spacecraft deck and panel shows a broad pile of soil at least 30 cm across. The soil

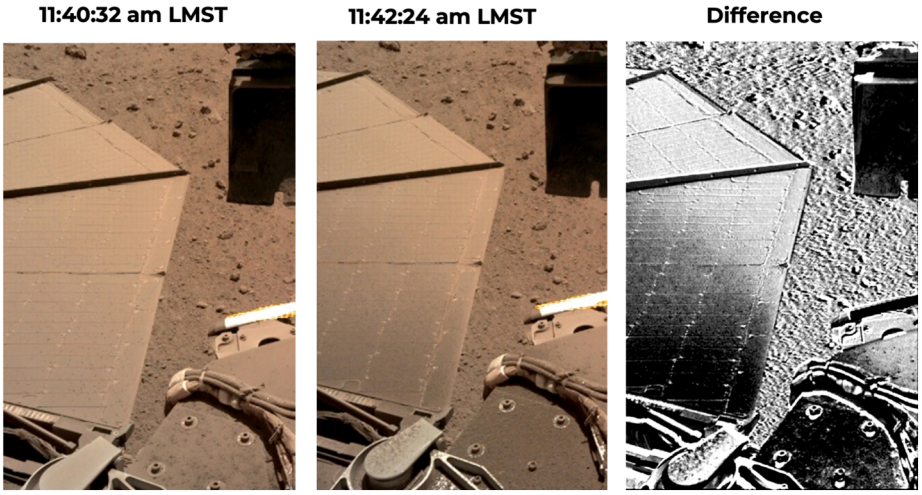

Fig. 21 IDC images before (left) and after (middle) the main avalanche from the dump of soil on the northwestern edge of the lander on sol 884. Right image is the IDC differenced image showing areas where the surface has been darkened from soil that was dumped on the lander deck (right) and where dust has been removed from the west solar panel (left). For scale, the full diameter of the circular solar panels is 2.2 m

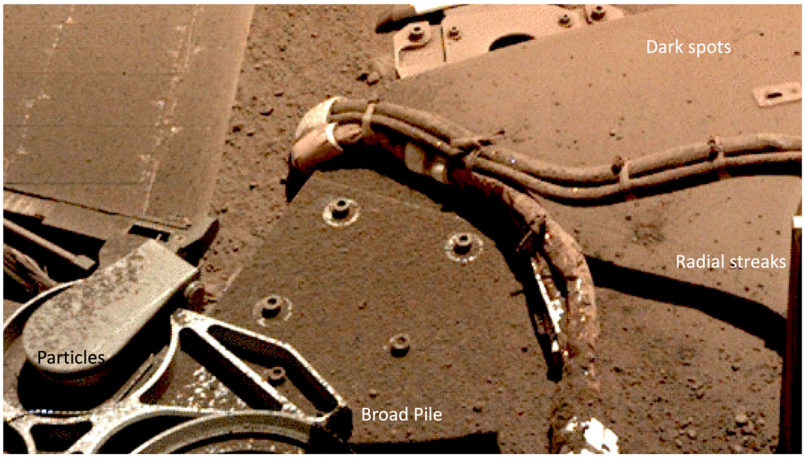

Fig. 22 Close up of the dump site on the northwestern part of the lander deck and the edge of the western solar panel on sol 884. Note some individual granules (of order mm) can be resolved as well as larger clods. Note radial streaks in circular impact site between the cables

in the pile is generally fine grained, although some larger pebbles (∼1 cm) and clods are present (Fig. 22). Much larger clods of soil visible in the scoop are not present on the deck, suggesting they are weakly cemented and broke apart during the dump or impact on the deck. One such clod appears to have impacted the deck to the northeast of the main pile and shows small clods with radial streaks, indicating the soil fragmented on impact and ejecta scoured radial streaks in the dust. Some larger particles are also present northeast of the main pile, but there are also individual dark spots without obvious particles, suggesting that smaller particles were responsible for removing the dust. A similar pattern of smaller particles is present on the spacecraft deck towards the solar panel and on the solar panel (Fig. 21).

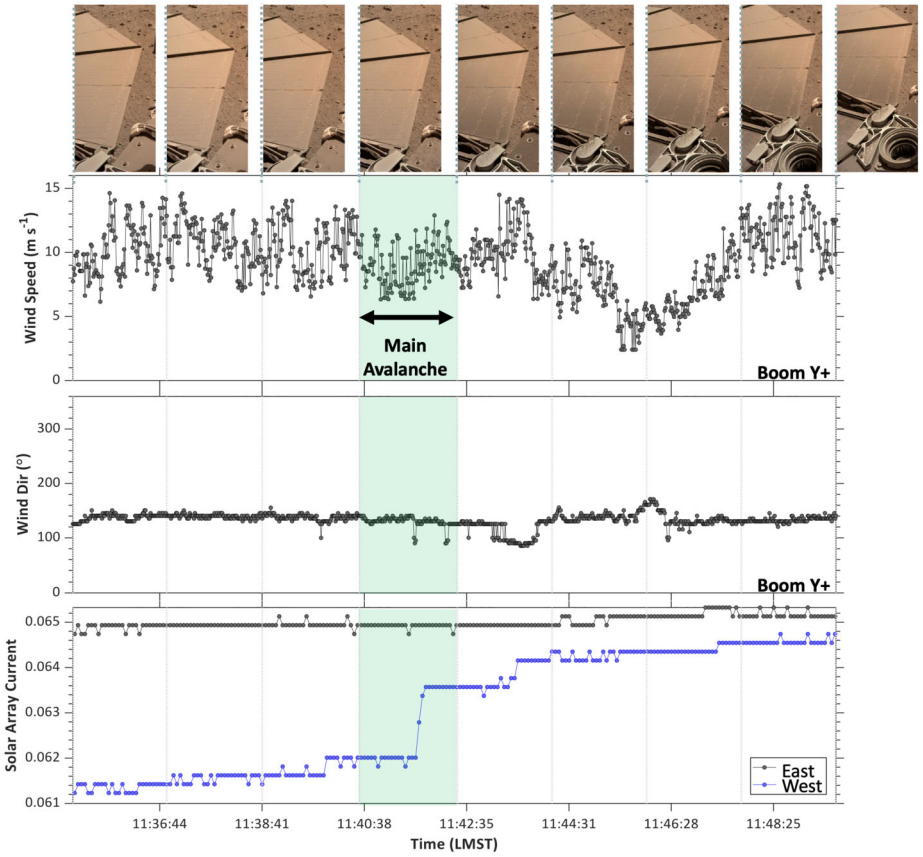

Fig. 23 Progressive IDC images of northwestern edge of the lander and the southeastern edge of the western solar array during the arm motion and dump of soil along with wind speed and direction from the TWINS +Y sensor and the detrended solar array current on both panels. The main avalanche from the scoop occurred between 11:40 and 11:42 LMST on sol 884 and resulted in a 3% increase in solar array current for the west array

However, the darkening of the panel covers a much broader area than the area covered by visible particles, suggesting that dispersed sand-size particles below the resolution of the images also removed dust.

IDC images every ∼2 minutes shows that the main avalanche from the scoop occurred between 11:40 and 11:42 LMST (Fig. 23). During this time, winds varied from 6-13 m/s (averaged ∼9 m/s), and were from a direction of mostly 140°. The dominant wind speed and direction are consistent with the direction and amount of dispersion of the soil in the previous tether dumps. The western solar array current increased by ∼3% and produced a 4 W instantaneous increase in power at the time of the dump and the energy improved by 24 W hr sol^{-1} and produced a long-term improvement of 35 W hr sol^{-1} (Fig. 17). The fact that the solar array power improved indicates the area covered by soil on the panels is less than the dark area, and therefore that soil that impacted the surface of the panel removed a greater area of dust than the area of the soil. If the darkened area of the panel is a 2 m by 1 m half ellipse and the dispersed volume is similar to that of the first dump on the tether, then the area covered by particles is about 1000 times less than the darkened area.

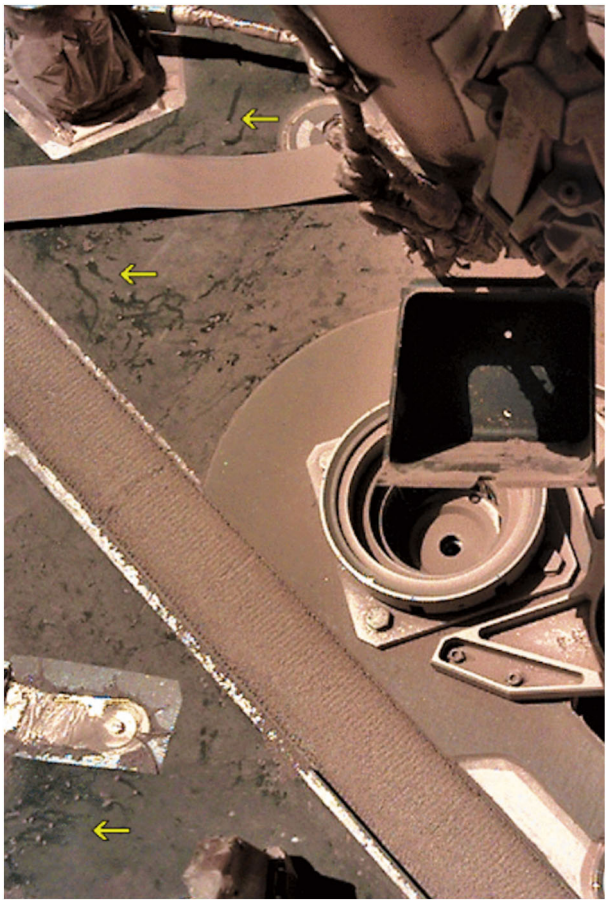

Fig. 24 IDC image from sol 897 showing cm long dark trails left by motion of granules on the deck that removed dust. This type of granule motion on the deck was observed throughout the solar array cleaning experiments. The granules were deposited on the deck during landing

The second solar array cleaning experiment took place on sol 897 and included the smallest scoop of soil (86.2 $\pm$10.7 cm^3). The dump occurred in the same location on the deck as the first dump and the soil was dispersed to the west and/or northwest due to winds of $\sim$10 m/s from the east and/or southeast. The dispersed soil overlapped the solar array already darkened from the first experiment. Even with the relatively small amount of soil dumped and the overlap in where the soil landed on the panel, there was a 1 W instantaneous power improvement and energy improved 6 W hr sol^{-1}. The improvement in power appeared to scale with the amount of soil dumped and there was no indication that it was less effective even though the soil landed in the same location in which soil from the first experiment landed. Images showed that granules (2-4 mm diameter) deposited on the deck during landing moved centimeters to the west and northwest leaving dark tracks where the dust was removed (Fig. 24).

The third solar array cleaning experiment occurred on sol 911 on a new part of the spacecraft deck to the south of the previous two dumps. A large scoop of soil (142.8 $\pm$14.9 cm^3) was dumped during a wind gust of 14 m/s from the south-southeast (170°) producing a large dispersion of soil to the north-northwest that darkened the edge of the solar panel but largely fell on the ground. The current of the west array increased by 1% at the time of the dump, the instantaneous power improved by 1 W, and energy improved by 6 W hr sol^{-1} (Fig. 17).

The fourth solar array cleaning experiment, and last before aphelion and conjunction, occurred on sol 938. A scoop of 101.5 ±18.8 cm^3 of soil was dumped on the same part of the deck as the third experiment. Relatively high winds from the south-southeast produced a large dispersion of soil to the north-northwest, which darkened the edge of the panel (like the third experiment). The instantaneous peak power increased by 2.5 W and energy improved by 3 W hr sol^{-1}; long-term energy improved by 10 W hr sol^{-1}. Granule motion on the deck was again observed between the 3rd and 4th experiments.

The first four solar array cleaning experiments were conducted with the objective of improving power sufficiently to keep the VBBs on continuously during the seasonal energy generation minimum near aphelion and during conjunction when the spacecraft was out of communication with the Earth. The four experiments improved power by around 10% and a total of ∼50 W hr sol^{-1} (Table 6) and were successful in meeting the objective of keeping the VBBs on continuously throughout the power low during aphelion and conjunction (Fig. 17).

The fifth solar array cleaning experiment was conducted on sol 1061 after conjunction. The scoop excavated the largest volume of soil (155.6 ±19.1 cm^3) and the dump occurred on the same part of the deck where the third dump occurred (the southernmost location). The soil was dispersed to the west more than ∼1 m at 15:11 LMST (when the main avalanche occurred), and landed on a portion of the west panel that had not been previously darkened by soil. Winds were ∼14 m/s from the east (90°) in agreement with the darkening of the panel. The instantaneous power improved by 2.5 W and energy improved by 15 W hr sol^{-1}. The long-term improvement in energy was 20 W hr sol^{-1} (Fig. 17).

The sixth solar array cleaning experiment occurred on sol 1143. A relatively large scoop of soil (135.2 ±26 cm^3) was dumped on the deck at the same location as the fifth dump. Differenced images showed some change on the western solar array, with some darkening on the adjacent deck to the southwest (Fig. 25). Winds were low with a velocity of ∼1 m/s from the southeast at the beginning of the avalanche to ∼6 m/s from the northeast later. The instantaneous power improved 1 W and energy improved by 7 W hr sol^{-1}, which is consistent with the limited dispersion of soil. The fifth and sixth solar array cleaning experiments improved energy by ∼25 W hr sol^{-1} (Table 6), which was sufficient to keep the VBBs on continuously through the SEIS quiet period, which was between sols 750 and 1200, with the quietest time between sols 800-1150.

The seventh, and final solar array cleaning experiment occurred on sol 1238 at around 17:00 LMST when winds were expected to be to the east. This was the last chance with sufficient power to support the scooping and dumping activity. This was also the first experiment to dump soil on the east side of the spacecraft deck with dispersion of soil expected onto the east solar array, because winds were no longer predicted to be from the east due to seasonal changes. Winds from the previous martian year were 2-6 m/s from the west-northwest. A small scoop of soil (99.1 ±15.3 cm^3) was dumped at 42 cm over the lander deck near the east TWINS wind sensor. Images showed little darkening of the solar panel, consistent with low winds (although there was not enough power to have TWINS on) and little soil was dispersed. There was no instantaneous change in current and no change in power from the east solar array.

Altogether, the solar array cleaning campaign was able to increase the energy generation capacity of the lander by a total of ∼80 W hr sol^{-1}, or ∼15% of the energy output in that timeframe. This allowed the SEIS instrument to remain powered on continuously throughout the low power period near aphelion and the seasonal seismic quiet period, which was between sols 750 and 1200, with the quietest time between sols 800-1150. It is unlikely that any science operations would have been possible after ∼sol 1200 without this energy boost; the solar array cleaning experiments helped extend the lifetime of InSight by ∼242 sols.

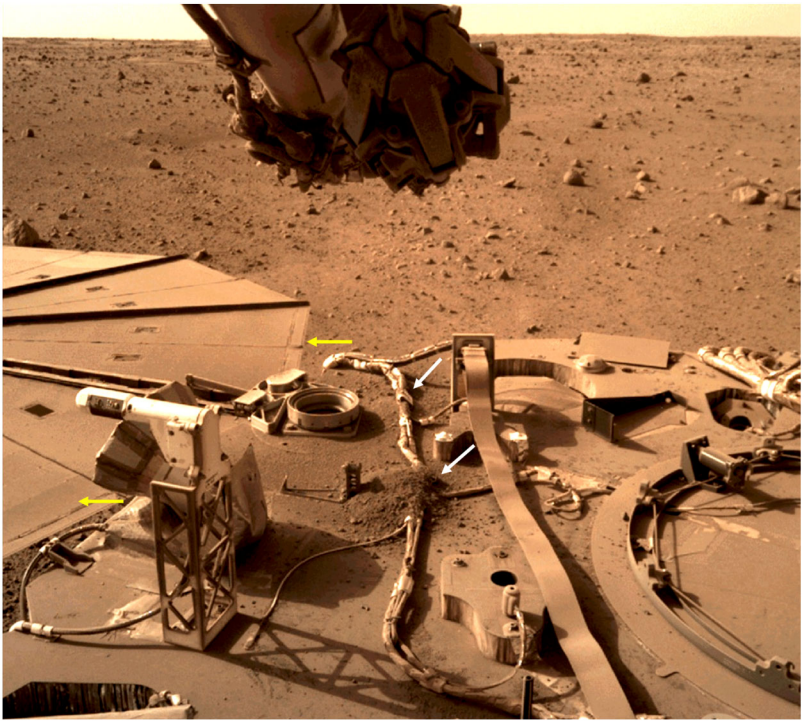

Fig. 25 IDC image acquired on sol 1143 after the sixth solar array cleaning experiment showing the accumulation of soil on the western spacecraft deck (white arrows) from the first six soil dumps and the darkening of the western solar array (yellow arrows) from the dispersion of soil during the dumps

10.5 Solar Array Cleaning Experiment Science Observations Summary

Taken together, the results from the solar array cleaning experiments are the first semi-controlled experiments on Mars that directly address how dust enters into suspension via impact by sand sized grains. Sand, which makes up most of the soil, was dispersed by drag forces from the wind that at least partially overcame gravitational forces, when dumped from ∼1.4 m over the surface. The majority of soil landed on the deck, but about 30% was dispersed by the wind, with higher winds dispersing particles several meters and lower winds dispersing the sand less (and very little in very low winds). Sand size particles that were dispersed impacted the solar panel with sufficient kinetic energy to kick dust into suspension and improving power generation. The area cleaned of dust is ∼100 times the area of a sand particle based on individual dark spots produced by single sand grains and the volume of soil dispersed compared with the area and thickness of observed dark zones, so that power improves even though the sand particle most likely remained on the panel. Repeat soil dumps that dispersed sand over the same part of the solar array did not show a decrease in cleaning, arguing that only a small fraction of the dust was removed during a cleaning attempt. The lack of any change in power during shaking of the solar array during periods of relatively high winds (∼10 m/s) is consistent with the expectation that very fine-grained dust particles (1-5 μm) require very high winds to be moved.

Because wind speeds decrease logarithmically towards the surface, winds at about 1 m above the surface near the lander deck would be expected to be higher than those at the

surface. As a result, it seemed possible that soil left in piles on the spacecraft deck, might be more susceptible to being moved by the wind than soil at the surface. If saltation of sand from the piles on the deck occurred and saltation pathways were large enough and the speed of the grains were high enough, sand grains might continue to impact the solar panels producing additional cleaning in between dumps. However, no cleaning was observed in between dumps, suggesting saltation was no more active at 1 m height than at the surface (Charalambous et al. 2021a). Conversely, larger granules did show motion in between cleaning experiments, indicating winds were high enough to move them, but not the smaller sand sized particles.

11 Arm Activities Late in the Mission

In addition to deploying the instruments, the IDA was used for aiding the mole, burying the tether and solar array cleaning experiments up until the power low near aphelion and spacecraft conjunction (around sol 1025, Fig. 17). It was recognized that there would be about 24 weeks or roughly 12, two-week planning cycles after the spacecraft came out of conjunction in which there would be sufficient power to conduct IDA activities. A list of possible IDA activities was assembled from input from the science working groups and science team. Not counting tether burial, solar array cleaning, and aeolian change activities that had already been conducted, about ten activities were identified that included: filling in the stereo panorama, IDC tau, sky survey, meteor shower imaging, soil indentation and elastic properties experiments, 2.4 Hz resonance investigation, magnetism of rocks and soil, additional high-resolution overlapping stereo imaging, and deep trenching. Each IDA activity was evaluated based on its scientific merit, the difficulty of commanding the arm, and the number of planning cycles needed to carry out the activity.

11.1 IDC Tau

Periodic measurement of tau or optical depth of the atmosphere with the IDC was needed to validate the ICC tau measurements that were made every other sol. The arm was moved to a standard pose with the IDC pointing into the sky in the morning or afternoon to acquire an image, which is then processed to determine tau (see Sect. 3.2). Because of the importance of measuring tau accurately for evaluating power production and the relative ease of acquiring an IDC tau, it was acquired on sol 1033.

11.2 Sky Survey

This activity involves acquiring 5 images of the sky at a broad range of scattering angles from the sun to quantify aerosol properties (including particle size) (e.g., Lemmon et al. 2004). This activity had been run previously on sols 122, 128, and 175 and included 5 IDC images at different azimuths at $30° \pm 15°$ elevation (Sect. 3.2). The imaging sequence could be run anytime it was convenient and it was simple to plan. This activity was performed on sol 1157.

11.3 Fill in Stereo Panorama

Three 360° stereo panoramas (morning, midday, and evening) were acquired with IDC images by moving the arm to different positions above the lander deck early in the mission

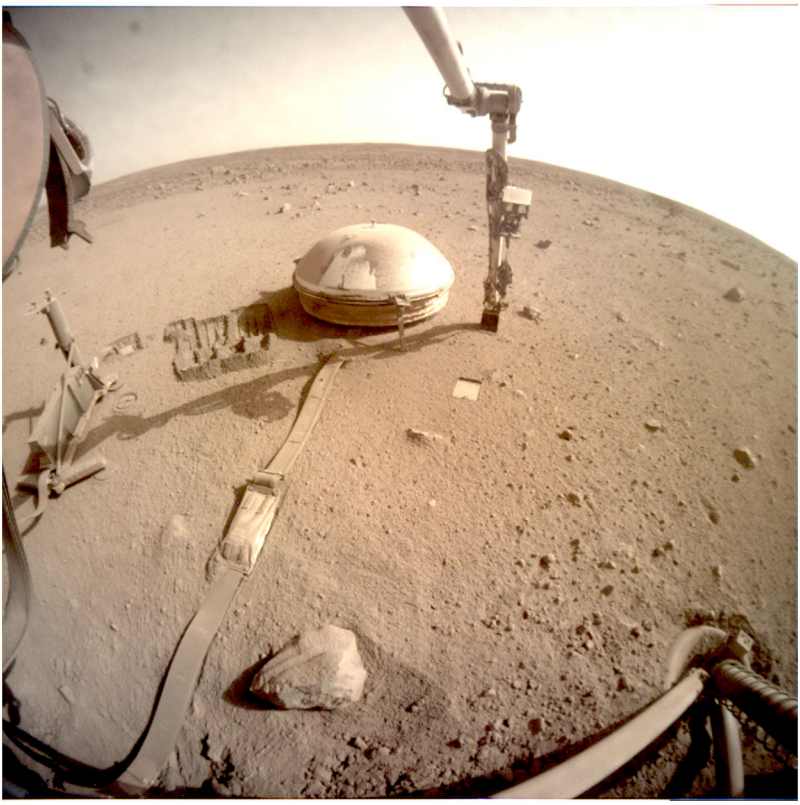

Fig. 26 ICC image on sol 1170 showing the IDA performing the second elastic properties experiment by repeatedly pushing on the ground resulting in a tilt recorded by SEIS. Rectangular smooth patch closer to the lander is the imprint of the back of the scoop from the indentation experiment and the first elastic properties experiment. Note the scrapes in the soil between SEIS and HP^3 showing the surface after tether burial (soil on top of tether near the WTS) and six of the solar array cleaning experiments. Rectangular smooth patch to the left (east) of the scrapes is where the back of the scoop tamped down the soil over the buried mole, with the HP^3 SSA nearby (Sect. 7). Note how dusty the SEIS tether and HP^3 (and spacecraft) are

(Golombek et al. 2020a). Acquisition of IDC images towards the west was complicated because it required folding the arm at the elbow joint over the deck into an inverted position. Further, because stereo images are acquired by rotating the shoulder joint, there were gaps in the stereo panoramas to the northwest and southwest near the hard stops in the shoulder joint between the images to west and the rest of the panorama (e.g., Golombek et al. 2021). After careful evaluation of the IDC image pointing near the gaps in the existing panoramas, it was concluded that additional images could be acquired near the shoulder joint hard stops by relaxing collision avoidance constraints in the flipped arm configuration. This enabled these to gaps to be filled in on sol 1047.

11.4 Indentation Experiment

The indentation experiment designed to measure plastic deformation of the soil was performed on Mars on sols 1074 and 1075. It consisted of using the IDA scoop to repeatedly push on the ground with a (near) vertical force at a defined location (Fig. 26). The IDA cur-

rent and torque limits were set to allow maximum downward force, while still preventing IDA damage. A validated algorithm was used to estimate the force at the scoop given current measurements at the robotic arm joints (Sect. 12). The push moves started approximately 1 cm above the surface and pushed down past the level of the surface. Four pushing depths (from 2.5 cm to 4 cm) were sequentially commanded from the 1 cm standoff. Between each push, images were acquired by the IDC and subsequently used to create DEMs of the scoop imprint from which the penetration depth can be measured. The measurement of the local plastic deformation of the ground underneath the IDA scoop and force applied by the scoop provide information on the regolith load bearing capacity. In particular, for given values of bulk density, cohesion and internal friction angle, the bearing properties can be estimated from Terzaghi's (1943) ultimate bearing capacity equation based on Prandtl's shear failure mechanism, which has direct implications for the regolith strength and subsurface structure. Although further work is needed to develop the relationship between the deformation observed, IDA telemetry, and failure parameters, preliminary results of the force estimates obtained using the JPL testbed at the indentation location are presented in Sect. 12.2.

11.5 Elastic Properties Experiment

The elastic properties of the regolith have an important influence on the seismic wavefield and travel times recorded by the SEIS instrument (Golombek et al. 2018a) (Sect. 7.7). A specific example is the influence of shallow near-receiver structure on seismic recordings, which is well known in terrestrial seismology. Knowledge of the elastic properties of the regolith helps to better understand these effects which need to be considered when analyzing SEIS data.

The elastic properties of the martian regolith are obtained by pressing on the martian ground using the scoop and the robotic arm, which causes the ground to decline slightly towards the scoop generating a tilt of SEIS that is observable on the horizontal component of the seismometer. A quasi-static surface deformation approach as described in Murdoch et al. (2017a, 2017b) can then be used to invert the declination in order to retrieve the mean elastic parameters of the ground between the scoop and SEIS.

The first elastic properties experiment was performed on sol 1156 and involved pressing on the ground with a (near) vertical force. This was to ensure that the tilt signal on SEIS was detectable, to reduce the error in the knowledge of the force applied by the scoop, and allowed the elastic properties experiment to be combined with an indentation experiment that required vertical forcing. The location selected to implement this experiment on Mars was chosen to be suitable for both the indentation and elastic properties experiments, and feasible for the IDA (Fig. 26).

A second elastic properties experiment was performed on sol 1170, with a larger radial force component, in order to further constrain ground properties. Adding radial forcing enables simultaneously solving for both Poisson's ratio and the shear modulus. The location of the second elastic properties experiment, about 48 cm farther out from the first experiment (Fig. 26), was based on experiments done in the InSight testbed. Initial results suggest Poisson's ratio is around 0.25 and the shear modulus is around 2 MPa, which are similar to those derived from SEIS recordings of hammering (Sect. 7.5).

11.6 2.4 Hz Resonance and Imaging

A hypothesis for the 2.4 Hz resonance measured by SEIS is that it is produced by motion of the solar arrays. Initially it was proposed to touch the east solar array with the IDA to steady

it while the resonance was observed. This was not performed because of the difficulty in planning the required IDA motions, but a series of images of the solar arrays were acquired to look for slight motions in the arrays when the 2.4 Hz resonance was expected to occur on sol 1136. No motion of the panel was observed.

11.7 Magnetic Properties of Soil and Rocks

One of the most startling early science results from InSight was that the magnetic field measured at the surface was ten times higher than predicted from satellite measurements and models, indicating strongly magnetized rocks beneath the surface of Noachian and/or Hesperian age, when the martian dynamo was active (Johnson et al. 2020, Mittelholz et al. 2020, Mittelholz and Johnson 2022). Satellite measurements of the crustal magnetic field constrain only the product of magnetization and magnetized layer thickness (e.g., Langlais et al. 2019), and although magnetization of meteorites can be assessed in the laboratory, interpretation of these data is debated due to the origin of the meteorites and their shock history (Mittelholz and Johnson 2022).

New InSight constraints show that magnetizations of at least 1-10 A/m are plausible for crustal rocks beneath the InSight lander, based on the magnetic field amplitude measured at the landing site (Johnson et al. 2020; Knapmeyer-Endrun et al. 2021) and satellite-based models (Mittelholz et al. 2018; Langlais et al. 2019). Although old ($>$3.7 Ga) units lie beneath InSight at $>$170 m depth, and can magnetize overlying material (Volk et al. 2021), the surface units are younger (Amazonian; $<$3.0 Ga) and so it is unclear whether magnetized material at depth would be accessible from the surface. However, the presence of clasts ejected from impact craters that are larger than $\sim$1 km diameter could excavate material from below the younger basalts (Golombek et al. 2017; Warner et al. 2022) and provide the first measurement of rock magnetic properties on the surface of Mars.

The planned experiment was to collect a pebble or a sample of martian soil using the scoop located at the end of IDA and bring it close to the magnetometer located below the east deck of the lander. The magnetic field would have been measured by incrementally moving the arm towards the magnetometer head with stops to distinguish the time varying field. This would have been repeated without material in the scoop. Both arm motions would have been conducted at similar local times, with IDC and ICC imaging to determine the distance of the scoop to the magnetometer. At a 1 nT sensitivity level, a 5 cm diameter sample with a magnetization of 10 A/m, could be detected at 10 cm from the magnetometer and several targets of this size were identified. Even though the potential scientific results were considered very positively, the complexity and number of planning periods required to carry it out were prohibitive and the experiment was not conducted.

11.8 Deep Trench

The pits produced by the retrorockets during landing offered the opportunity to examine the shallow subsurface showing relatively steep sides indicating an unexpected cemented duricrust (Golombek et al. 2020a; Spohn et al. 2022b; Warner et al. 2022). Digging a deep trench, tens of centimeters deep could expose a broader area of the subsurface to examine the shallow stratigraphy. Interaction between the scoop and arm and surface materials would also provide information about the physical properties and soil mechanics of the near surface materials (e.g., Golombek et al. 2018a). Unfortunately, the software for operating the IDA did not include a trenching motion accommodated primarily by the wrist, and rewriting the software to add that capability was beyond the available time or resources. Although a modified scraping motion that used the shoulder and elbow joints could have been conceivably

employed, the number of planning cycles required to dig a deep trench seemed far beyond the remaining possible IDA opportunities and the activity was not pursued.

11.9 Last Arm Activities

Late in the mission (after March 23, 2022), after all the science-based IDA activities had been accomplished and power was still sufficient to perform additional IDA activities a number of final arm activities were considered. The highest priority was sunrise and sunset imaging and movies that showed the sun rise and set. Similar images had been acquired on Sol 145. In both occurrences the arm was prepositioned on the previous sol to the sunrise imaging pose. The camera was later heated to operating temperature to acquire the sunrise images. After sunrise, the arm was moved to the sunset pose later in the day (sol 1198) and the sunset images were acquired at dusk.

A no load actuator characterization, which had been executed periodically throughout the mission, was performed on sol 1198, to gauge the health of the IDA's actuators and its performance over the life of the mission. The IDA current draws show that performance on sol 1198 was almost identical to that on Sol 151, which was executed at a very similar temperature. Two other imaging activities accomplished in the final weeks were final imaging of the HP^3 and calibration target (Fig. 19B). Both activities were intended to characterize dust accumulation and their effect on both color detection as well as fiducial targets. The calibration target was almost completely obscured by dust (Fig. 19B). A $4 \times 4 \times 1$ mosaic of the surface to the southwest of SEIS was acquired on sol 1183 to create a final Structure from Motion DEM (Sect. 3.5).

Fairly early in the mission (within the first 20 sols) (Table 2), the arm reached down under the spacecraft to obtain stereo images, which showed pits that had been excavated by the landing thrusters (Golombek et al. 2020a). These ~10 cm deep pits showed the shallow subsurface stratigraphy. Although motion of some granule-size particles by wind vortices have been documented by InSight (Charalambous et al. 2021a; Baker et al. 2021), aeolian bedforms are sparse, associated with relatively fresh craters, indicating that the surface has largely reached aerodynamic equilibrium with surface winds (Golombek et al. 2020a) (Sect. 6) and net transport of fines is limited (Sect. 8). Re-imaging the area beneath the lander offered an opportunity to see if the pits and surface had changed over ~2 Mars years. Acquiring these images required careful scrutiny of the arm motions to be sure they did not interact with the instruments or tethers. These images were successfully acquired on sol 1211, and they showed a surface largely unchanged from early in the mission.

The IDA and IDC were used to acquire images of the lander and solar arrays (a spacecraft selfie) on sol 10 of landing (Fig. 18a). To document the cumulative changes to the spacecraft from dust deposition as well as dumping soil on the lander deck over 3 Earth years, a repeat spacecraft selfie was acquired on sol 1211 (Fig. 18b). The dust on the spacecraft and solar panels dramatically obscures the original colors.

12 Testbed Calibration

12.1 Testbed Calibration Activities

Calibration tests were performed in the JPL testbed (see Sect. 5.2) to help with the interpretation of the data acquired on Mars during the activities involving interactions between the IDA scoop and the ground (Fig. 27). These activities include the indentation experiment

Fig. 27 Picture of the engineering model lander, robotic arm, and scoop in the JPL testbed. Note the container of simulant below the arm as well as the SEIS and HP^3 models on the surface to the left. The IDC is on the forearm of the IDA and the ICC is mounted beneath the deck to the left (with red around the lens). Note the lander feet were placed on cinder blocks to enable end to end testing of arm activities that assisted the HP^3 mole and interacted with the surface

(Sect. 10.4), elastic properties experiments (Sect. 10.5), and the flat and tip pushes performed as part of the mole recovery activities (Sect. 6). The interpretation of these activities relies on the measurements of the pressure applied by the scoop to the ground and, hence, on knowing the force imparted by the scoop. The scoop can be oriented such that either the flat bottom of the scoop or the tip of the scoop contacts the soil. Because the IDA is not equipped with a force-torque sensor, the force measurements must be inferred from the IDA telemetry (i.e., motor currents and torques). It is worth noting that the force magnitude at the scoop in the x-, y-, and z-direction depends on the arm pose and, thus, different force values are obtained at different locations in the workspace. To estimate the force magnitude and to provide data to validate the force algorithm, calibration tests were conducted in the JPL testbed at locations that matched those that were performed on Mars.

A three-axis force load cell was used to measure the scoop external loads simultaneously in three mutually perpendicular axes (i.e., x, y, and z). The load cell (ATO-LC-MA02) acquires force data at a sampling rate of 0.5 Hz and is wired to a data acquisition system

Fig. 28 Picture of the IDA scoop and multi-axis load cell in the testbed. Flat bottom of the IDA scoop is pressing on the multi-axis load cell setup at the Indentation and Elastic Properties location. Directions of the x-, y-, and z-axis forces are shown. Note the scoop tip to the right and the secondary blade on the bottom left. Note portion of calibration target (white circles on black background) against the wall behind the lander and the lander footpad to the right

(Keysight DAQ34972a). A top plate is mounted on the load cell and designed with a groove to fit the scoop when pushing with its tip or flat bottom. The load cell is also bolted to a base plate that remains parallel to the top plate. Figure 28 shows the IDA scoop pressing with its flat bottom on the multi-axis load cell setup. Tests were run at three different locations to match those done at Mars near the HP^3 hole, at the Indentation and first Elastic Properties location, and at the second Elastic Properties location. Near HP^3, the scoop external loads are measured for both the flat and tip pushes.

12.2 Testbed Calibration Results

To evaluate the force magnitude in the x-, y-, and z-direction, the external loads were measured using the multi-axis load cell setup for multiple scoop pushes at each workspace location of interest. The results are summarized in Fig. 29 for the flat push performed near HP^3 on Sol 240 (Fig. 29a), the tip push performed near HP^3 on Sol 240 (Fig. 29b), the Indentation and first Elastic Properties location (Fig. 29c), and the second Elastic Properties location (Fig. 29d). In Fig. 29, the box and whiskers plots show the distribution of the data points into quartiles, highlighting the mean and spread of the data.

For all locations, the force values in the y-direction, F_y are close to zero with all data points close to the median value, which is consistent with the flat and tip push loading scenarios. For the pushes near HP^3, comparable values of the median forces in the x- and z-directions, i.e., $F_x = 56.3$ N and $F_z = 77.2$ N for the flat push (Fig. 29a) are found, while $F_x = 57.5$ N and $F_z = 73.5$ N for the tip push (Fig. 29b). Nonetheless, the spread of the F_x and F_z values is larger for the flat push than for the tip push.

Figures 29c and 29d present the force measurements at the first indentation and elastic properties experiment location, in which the IDA forearm is in a vertical position, and at the

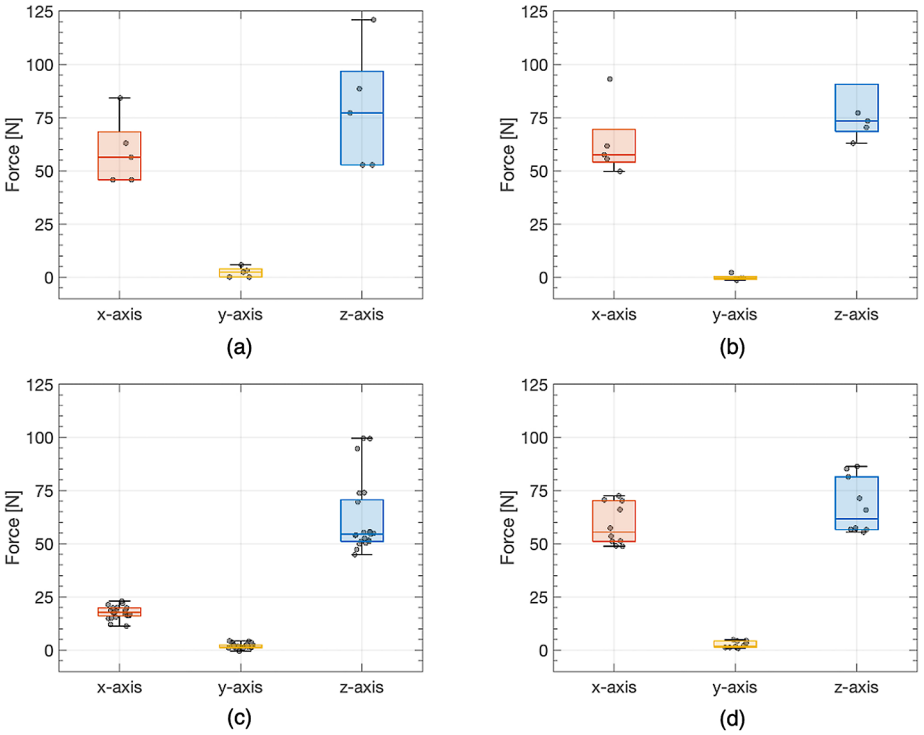

Fig. 29 Summary of the force load cell measurements along the x-, y-, and z-directions for (a) a push with the flat part of the scoop near where the HP^3 was deployed, (b) a push with the scoop tip near the mole hole, (c) a push with the bottom of the scoop where the indentation and first elastic properties experiments were performed, and (d) a push with the bottom of the scoop where the second elastic properties experiment was performed. Grey dots represent individual data points. Box and whiskers plots represent the data distribution for F_x, F_y, and F_z. For each box, the central horizontal line indicates the median, and the bottom and top edges of the box indicate the 25th and 75th percentiles, respectively. The whiskers extend to the most extreme data points not including outliers

second elastic properties experiment location, in which the IDA is extended about 48 cm farther away from the first location. At the first location, the median forces are $F_x = 17.7$ N and $F_z = 54.4$ N, while, in the second location, $F_x = 55.4$ N and $F_z = 61.6$ N. These results indicate that the more the IDA is extended away from the lander, the higher the force in the x-direction F_x, and, hence, the higher the F_x/F_z ratio. This data was used for an initial assessment of the IDA performance on Mars.

When the IDA is commanded and operational, IDA engineering and ancillary data are recorded and available from the Planetary Data System (PDS; http://pds.nasa.gov/). IDA engineering telemetry contains detailed sensor data typically collected every sample period (e.g., motor temperatures, motor currents, motor voltages, end effector location and orientation, joint velocities, joint torques). Additionally, IDA status, IDA history, and IDA parameters are included in this archive as ancillary data. To assist in post-mission analyses of regolith-scoop performance, the IDA motor-current data can be further processed and plotted for comparison with the calibration data presented above. The data are available in the NASA Planetary Data System (PDS) Geosciences Node (InSight IDA Science Team 2019) and include the multi-axis load cell measurements and IDA telemetry science data.

13 Summary

The InSight lander carried an Instrument Deployment System that included an Instrument Deployment Arm with a scoop and grapple, and two cameras, the arm-mounted Instrument Deployment Camera and the lander-mounted Instrument Context Camera. As originally proposed, the IDS was designed only to image the workspace in black and white and to place the instruments onto the surface, and had no science objectives or expectation to be used after instrument deployment (>90 sols). However, during development and operations on Mars, the cameras were upgraded to color and IDS evolved into an invaluable tool for both mission support and science. It assisted the HP^3 mole in penetrating below the surface, buried the SEIS tether in an attempt to ameliorate seismic noise, and partially cleaned the solar panels, substantially increasing the lifetime and scientific output of the mission. It was able to undertake scientific investigations of its own using the camera systems in focused imaging campaigns with the arm to interact with the soil in previously unplanned ways. No other Mars surface mission has engaged in such a sustained and varied campaign of arm and scoop activities directed at such a diverse suite of objectives. The contribution of the IDS to our understanding of geology, aeolian processes and soil properties and mechanics on Mars has been substantial, and the rich experience from InSight can be used to design robotic experiments on Mars and other planetary surfaces.

The IDA and IDC carried out a wide variety of imaging campaigns including: stereo panoramas at three different times of day, imaging of the workspace at two different resolutions for selecting the sites to place the instruments, stereo imaging beneath the lander to document the alteration of the surface by the retrorockets, regular measurement of the sky to get optical depth for power management and solar array performance, dust devil searches, cloud imaging and sky surveys, astronomical imaging, and closely spaced stereo images to create high-resolution DEMs.

The Instrument Site Selection Working Group used mosaics of the workspace and radiometer data from the HP^3 immediately after landing, to evaluate requirements and desirements related to slope, rocks, material properties and IDA capabilities for deploying the SEIS, WTS and HP^3 onto the surface. The workspace was benign and selected sites for both instruments were near their preferred locations with both instruments as far away from each other and from the lander to reduce noise with SEIS to the west. Deploying the instruments with the IDA was tested extensively within a JPL testbed and was accomplished within the allotted first 90 sols.

The geology investigation was enabled by multiple stereo panoramas, imaging underneath the lander and close-up images of the area immediately adjacent to the lander. The landing site in view is characterized by smooth to slightly rocky terrain with relatively low rock abundance and craters in a wide range of states of degradation. Images beneath the lander and in the mole pit showed a cemented duricrust, overlain by unconsolidated sand and a thin dust layer. Sandy regolith near the surface grades with depth into brecciated and fractured Early Amazonian to Hesperian basalt, underlain at >170 m by Noachian sedimentary rocks. The plains on which InSight landed can be considered a type example of a Hesperian lava plain on Mars, which were shaped predominantly by impact and aeolian processes and cover vast portions of its surface.

The IDA was used extensively for ~22 months to assist the HP^3 mole in penetrating into the subsurface, which was inhibited by the cohesive duricrust that limited friction needed for the mole to penetrate. IDC images and movies showed the state (tilt and depth) of the mole and the open pit that developed during the mole recovery activities. The IDA also removed the support structure to expose the mole and uncover the open pit that developed around

it. The scoop was used to push on the mole during hammering to assist in penetration. Finally, when the mole had penetrated to where its back cap was just below surface level, soil was scraped from adjacent areas to fill the depression around the mole and tamped down, which enabled the mole to collect thermal conductivity measurements. Interactions with the surface allowed derivation of soil mechanics parameters (cohesion and angle of internal friction), that when combined with thermal conductivity and seismic velocities from hammering yielded the most detailed physical and elastic properties of near surface materials on Mars.

The combination of IDC images with the arm pointed down close to the ground for extended periods and continuous meteorology measurements provided the most detailed investigation of threshold friction wind speeds and pressure drops needed to initiate observed saltation and surface creep during wind vortices. Concurrent seismic and magnetic changes observed during wind vortex events appear associated with ground tilt acceleration and perturbations in the magnetic field strength, consistent with charged-particle motion. The vortices were sand-poor and lifted little dust suggesting little sediment flux through the area, in agreement with limited aeolian activity and dusty, sparse, inactive aeolian bedforms.

Soil was scraped into piles, excavated into the scoop by the arm, and dumped onto the SEIS tether six times in an attempt to reduce noise recorded by SEIS. The first soil dump was from 55 cm above the ground onto the edge of the WTS. The soil that fell on the WTS cleaned yellowish brown dust off a portion of the WTS, added brownish soil (mostly sand) around the edges, deposited a shallow pile of soil on the SEIS tether adjacent to the WTS. Soil was also dispersed to the west almost 1 m by the wind as shown by darkened areas in differenced ICC images. The volume of soil in the scoop and pile was determined by subtracting DEMs before and after the scoop and dump and the difference between them indicated that $\sim$30% of the soil was entrained into and dispersed by the wind. The darkening of the surface was produced by entrained sand grains impacting the surface and kicking the dust into suspension (i.e., removing the dust) and by the deposition of darker sand grains on the surface. The first four dumps occurred with moderate to low wind speeds and produced similar dispersions in the direction of the measured wind. The last two dumps were moved to midday times of high wind speed and produced much larger soil dispersions (1-2 m) in the down wind direction. Computational fluid dynamic models that include gravity and wind drag indicate fine sand ($\sim$0.1-0.2 mm diameter) would be transported in the observed winds. Scraped and dumped piles, and walls produced by the scrapes yield estimates of the angle of internal friction of the soil. About 93% of the SEIS tether within 20 cm of the WTS was covered by $>$1 cm of soil, but there was no reduction in noise.

Power generated by the two solar arrays on InSight was reduced exponentially by $\sim$90% in the $\sim$2 martian years after landing (from 4750 W hrs to $\sim$400 W hrs) due to deposition of dust on the panels (dust factor). Images of the calibration target are completely obscured by dust, which fully coats the solar arrays. The dusty nature of the landing site is consistent with its orbital thermophysical properties and the possible removal of dust by wind vortices (as observed by previous solar powered spacecraft) was estimated to be rare from the analysis of dust devil tracks. Few obvious practical options could be found to remove the dust.

Seven solar array cleaning experiments were conducted between sols 884 and 1238 by dumping soil from 35 cm above the spacecraft deck adjacent to a solar panel during windy times of the sol. Some of the soil, composed mostly of sand size grains was dispersed onto the panel by the wind and impacted the surface to kick the dust on the panel into suspension and improve the power generated by the solar arrays. The first four solar array cleaning experiments were conducted at midday with strong winds from the east that dispersed sand $\sim$1-3 m to the west onto the western solar array and improved power sufficiently ($\sim$10%, $\sim$40 W hr sol^{-1}) to keep the SEIS VBBs on continuously throughout the low power period

during aphelion and conjunction. The fifth and sixth solar array cleaning experiments were conducted after conjunction on sols 1061 and 1143, respectively, and improved energy by 22 W hr sol^{-1}, which was sufficient to keep the VBBs on continuously through the SEIS quiet period (when most marsquakes have been observed), between sols 750 and 1200. The solar array cleaning campaign increased the energy generation of the lander by a total of $\sim$80 W hr sol^{-1}, or $\sim$15% of the energy output in that timeframe and extended the lifetime of the lander and continued science operations after sol 1200 to sol 1442.

The results from the solar array cleaning experiments are the first semi-controlled experiments on Mars that directly address how dust gets into suspension via impact by sand size grains. Sand size grains, which make up most of the soil, were entrained and dispersed by drag forces from the wind that at least partially overcame gravitational forces, when dumped from >0.45 m over the surface. Sand size particles that were dispersed impacted the panel and kicked the dust into suspension, which removed the dust from the solar array and improved power generation. The area cleaned of dust is $\sim$100 times the area of each sand particle, so that power improves even though the sand particle most likely remained on the panel. These observations agree with the expected very high threshold friction wind speeds needed to get dust on the surface into suspension and support models in which saltating sand is an effective mechanism to lift dust off the surface and into suspension. The observation that no cleaning occurred in between dumps, suggests that wind speed, saltation pathways or particle velocities were not high enough for sand in piles on the deck to clean the solar panels.

After conjunction around sol 1025, power models indicated about 24 weeks remained in which power could support IDA activities. Final IDA imaging included an IDC tau to calibrate the ICC tau measurements, a sky survey to investigate aerosol properties, stereo images to fill in gaps in the stereo panorama, sunrise-sunset images, and final imaging of the HP^3, spacecraft, and calibration target. An indentation experiment was conducted using the IDA scoop to repeatedly push on the ground with a (near) vertical force with stereo images between each push to measure the plastic deformation of the soil to derive its bearing strength. Two elastic properties experiments were conducted by repeatedly pressing on the ground using the scoop on the robotic arm, which caused the ground to decline slightly towards the scoop, generating a tilt of SEIS and the derivation of Poisson's ratio and the shear modulus.

Calibration tests were performed in the JPL testbed to enable the derivation of three-dimensional forces from arm motor currents and torques for the indentation and elastic properties experiments, and the flat and tip pushes performed as part of the mole recovery activities. The testbed was set up to use a load cell to measure the x-, y-, and z-forces at the locations where these activities were performed on Mars, which enable the derivation of the physical properties of the soil where these interactions occurred.

Acknowledgements A portion of the work was supported by the InSight Project at the Jet Propulsion Laboratory, California Institute of Technology, under a contract with the National Aeronautics and Space Administration (80NM0018D0004). Thanks to E. Eelkema Stough and E. Barrett for helping to track down when some events occurred. A portion of the work was supported by grants 80NSSC18K1625 to J. Grant, 80NSSC18K1624 to N. Warner, and 80NSSC18K1626 to R. Lorenz from the National Aeronautics and Space Administration InSight Participating Scientist program. Data returned by InSight are archived in the NASA Planetary Data System (PDS), with image data in the Imaging Node and IDA data in the Geosciences Node. This paper is InSight Contribution Number 244.

Declarations

Competing Interests The authors have no conflicts of interest to report.

References

Abarca H, Deen R, Hollins G, Zamani P, Maki J, Tinio A et al (2019) Image and data processing for InSight lander operations and science. Space Sci Rev 215(2):22. https://doi.org/10.1007/s11214-019-0587-9

Achilles CA et al (2017) Mineralogy of an active eolian sediment from the Namib Dune, Gale Crater, Mars. J Geophys Res, Planets 122:2344–2361. https://doi.org/10.1002/2017JE005262

Ali KS (2021) InSight Mars lander Instrument Deployment Arm flight software. In: IEEE aerospace conference, 06 March 2021

Arvidson RE et al (2009) Results from the Mars Phoenix lander Robotic Arm experiment. J Geophys Res 114:E00E02. https://doi.org/10.1029/2009JE003408

Bailey P, Sorice C, Trebi-Ollennu A, Ali K, Myint S, Kim W (2020) Deployed instrument monocular localization on the InSight Mars lander. In: Proceedings of the IEEE aerospace conference, March 7-14, 2020, 01 March 2020

Baker MM, Newman CE, Lapotre MGA, Sullivan R, Bridges NT, Lewis KW (2018a) Coarse sediment transport in the modern Martian environment. J Geophys Res, Planets 123(6):1380–1394

Baker MM, Lapotre MGA, Minitti ME, Newman CE, Sullivan R, Weitz CM et al (2018b) The Bagnold dunes in southern summer: active sediment transport on Mars observed by the Curiosity rover. Geophys Res Lett 45(17):8853–8863. https://doi.org/10.1029/2018gl079040

Baker M, Newman C, Charalambous C, Golombek M, Spiga A, Banfield D et al (2021) Vortex-dominated aeolian activity at InSight's landing site, Part 2: local meteorology, transport dynamics, and model analysis. J Geophys Res, Planets 126(4):e2020JE006514. https://doi.org/10.1029/2020JE006514

Balme M, Hagermann A (2006) Particle lifting at the soil-air interface by atmospheric pressure excursions in dust devils. Geophys Res Lett 33(19):L19S01. https://doi.org/10.1029/2006GL026819

Banerdt WB, Smrekar SE, Banfield D, Giardini D, Golombek M, Johnson CL et al (2020) Early results from the InSight mission: mission overview and global seismic activity. Nat Geosci 13(3):183–189. https://doi.org/10.1038/s41561-020-0544-y

Banfield D, Spiga A, Newman C, Forget F, Lemmon M, Lorenz R et al (2020) The atmosphere of Mars as observed by InSight. Nat Geosci 13:190–198. https://doi.org/10.1038/s41561-020-0534-0

Berger JA et al (2016) A global Mars dust composition refined by the Alpha-Particle X-ray Spectrometer in Gale Crater. Geophys Res Lett 43:67–75. https://doi.org/10.1002/2015GL066675

Bonitz RG, Nguyen TT, Kim WS (2000) The Mars Surveyor '01 Rover and robotic arm. In: IEEE aerospace conference, proceedings (Cat. No. 00TH8484), vol 7, pp 235–246. 2000

Bonitz RG, Shiraishi L, Robinson M, Arvidson RE, Chu PC, Wilson JJ et al (2008) NASA Mars 2007 Phoenix lander robotic arm and icy soil acquisition device. J Geophys Res 113:E00A01. https://doi.org/10.1029/2007JE003030

Brinkman N, Schmelzbach C, Sollberger D, Pierick JT, Edme P, Haag T et al (2022) In situ regolith seismic velocity measurement at the InSight landing site on Mars. J Geophys Res, Planets 127:e2022JE007229. https://doi.org/10.1029/2022JE007229

Charalambous C, McClean JB, Baker M, Pike WT, Golombek M, Lemmon M et al (2021a) Vortex-dominated aeolian activity at InSight's landing site, Part 1: multi-instrument observations, analysis and implications. J Geophys Res, Planets 126(6):e2020JE006757. https://doi.org/10.1029/2020JE006757

Charalambous C, Stott AE, Pike WT, McClean JB, Warren T, Spiga A et al (2021b) A comodulation analysis of atmospheric energy injection into the ground motion at InSight, Mars. J Geophys Res, Planets 126(4):e2020JE006538. https://doi.org/10.1029/2020JE006538

Chatain A, Spiga A, Banfield D, Forget F, Murdoch N (2021) Seasonal variability of the daytime and nighttime atmospheric turbulence experienced by InSight on Mars. Geophys Res Lett 48:e2021GL095453. https://doi.org/10.1029/2021GL095453

Christensen PR, Moore HJ (1992) The Martian surface layer. In: Kieffer HH, Jakosky BM, Snyder CW, Matthews MS (eds) Mars. University of Arizona Press, Tucson, pp 686–727

Christensen PR, Bandfield JL, Hamilton VE, Ruff SW, Kieffer HH, Titus TN et al (2001) Mars Global Surveyor Thermal Emission Spectrometer experiment: investigation description and surface science results. J Geophys Res 106(E10):23,823–23,871. https://doi.org/10.1029/2000JE001370

Daubar I, Lognonne P, Teanby NA, Miljkovic K, Stevanović J, Vaubaillon J, Kenda B et al (2018) Impact-seismic investigations of the InSight mission. Space Sci Rev 214:132. https://doi.org/10.1007/s11214-018-0562-x

Delage P, Karakostas F, Dhemaied A, Belmokhtar M, Lognonné P, Golombek M, De Laure E, Hurst K, Dupla JC, Kedar S, Cui YJ, Banerdt B (2017) An investigation of the mechanical properties of some Martian regolith simulants with respect to the surface properties at the InSight mission landing site. Space Sci Rev 211:191–213. https://doi.org/10.1007/s11214-017-0339-7

Delage P, Marteau E, Vrettos C, Golombek MP, Ansan V, Banerdt WB, Grott M, Hurst K, Lognonné P, Murdoch N, Piqueux S, Schmelbach C, Spohn T, Warner N, Widmer-Schnidrig R, Brinkman N, Caicedo-Hormaza B, Castillo-Betancourt JP, Edme P, Kedar S, Lange L, Lemmon M, Mueller N, Onodera K, Robertsson J, Sollberger D, Stähler S, Verdier N, Williams NR (2022) The mechanical properties of the Martian soil at the InSight landing site. In: Proc. 20th int. conf. on soil mechanics and geotechnical engineering, Sydney, Australia, May 2022. HAL Id: hal-03706564, https://hal.archives-ouvertes.fr/hal-03706564

Domokos A, Bell JF III, Brown P, Lemmon MT, Suggs R, Vaubaillon J, Cook W (2007) Measurement of the meteoroid flux at Mars. Icarus 191:141–150. https://doi.org/10.1016/j.icarus.2007.04.017

Ehlmann BL et al (2017) Chemistry, mineralogy, and grain properties at Namib and High dunes, Bagnold dune field, Gale crater, Mars: a synthesis of curiosity rover observations. J Geophys Res, Planets 122:2510–2543. https://doi.org/10.1002/2017JE005267

Folkner WM, Dehant V, Le Maistre S, Yseboodt M, Rivoldini A, Van Hoolst T et al (2018) The rotation and interior structure experiment on the InSight mission to Mars. Space Sci Rev 214:100. https://doi.org/10.1007/s11214-018-0530-5

Garvin JB, Dotson R et al (2019) Micro-topography of the Mars InSight landing site: geological implications. In: 50th lunar and planetary science conference abstract # 1705. Lunar Planet Inst, Houston

Giardini D, Lognonné P, Banerdt WB, Pike WT, Christensen U, Ceylan S et al (2020) The seismicity of Mars. Nat Geosci 13(3):205–212. https://doi.org/10.1038/s41561-020-0539-8

Goetz W, Bertelsen P, Binau CS, Gunnlaugsson HP, Hviid SF, Kinch KM et al (2005) Indication of drier periods on Mars from the chemistry and mineralogy of atmospheric dust. Nature 436:62–65

Goetz W, Pike WT, Hviid SF, Madsen MB et al (2010) Microscopy analysis of soils at the Phoenix landing site, Mars: classification of soil particles and description of their optical and magnetic properties. J Geophys Res 115:E00E22. https://doi.org/10.1029/2009JE003437

Golombek M, Arvidson RE, Bell JF III, Christensen PR et al (2005) Assessment of Mars Exploration Rover landing site predictions. Nature 436:44–48. https://doi.org/10.1038/nature03600.

Golombek MP, Crumpler LS, Grant JA, Greeley R, Cabrol NA, Parker TJ, Rice JW Jr, Ward JG, Arvidson RE, Moersch JE, Fergason RL, Christensen PR, Castaño A, Castaño R, Haldemann AFC, Li R, Bell JF III, Squyres SW (2006a) Geology of the Gusev cratered plains from the Spirit rover traverse. J Geophys Res, Planets 110:E02S07. https://doi.org/10.1029/2005JE002503

Golombek MP, Grant JA, Crumpler LS, Greeley R, Arvidson RE, Bell JF III, Weitz CM, Sullivan R, Christensen PR, Soderblom LA, Squyres SW (2006b) Erosion rates at the Mars Exploration Rover landing sites and long-term climate change on Mars. J Geophys Res, Planets 111:E12S10. https://doi.org/10.1029/2006JE002754

Golombek MP, Haldemann AFC, Simpson RA, Fergason RL, Putzig NE, Arvidson RE, Bell JF III, Mellon MT (2008) Martian surface properties from joint analysis of orbital, Earth-based, and surface observations. In: Bell JF III (ed) The Martian surface: composition, mineralogy and physical properties. Cambridge University Press, Cambridge, pp 468–497, Chap. 21

Golombek MP, Warner NH, Ganti V, Lamb MP, Parker TJ, Fergason RL, Sullivan R (2014) Small crater modification on Meridiani Planum and implications for erosion rates and climate change on Mars. J Geophys Res, Planets 119:2522–2547. https://doi.org/10.1002/2014JE004658.

Golombek M, Kipp D, Kipp D, Warner N, Daubar IJ, Fergason R et al (2017) Selection of the InSight landing site. Space Sci Rev 211(1!4):5–95. https://doi.org/10.1007/s11214-016-0321-9

Golombek M, Grott M, Kargl G, Andrade J, Marshall J, Warner N et al (2018a) Geology and physical properties investigations by the InSight lander. Space Sci Rev 214:84. https://doi.org/10.1007/s11214-018-0512-7

Golombek MP, Charalambous C, Pike WT, Sullivan R (2018b) The origin of sand on Mars (expanded abstract). In: 49th lunar and planetary science, abstract #2319. Lunar Planet Inst, Houston

Golombek M, Warner NH, Grant JA, Hauber E, Ansan V, Weitz CM et al (2020a) Geology of the InSight landing site on Mars. Nat Commun 11(1):1014. https://doi.org/10.1038/s41467-020-14679-1

Golombek M, Williams N, Warner NH, Parker T, Williams MG, Daubar I et al (2020b) Location and setting of the Mars InSight lander, instruments, and landing site. Earth Space Sci 7:e2020EA001248. https://doi.org/10.1029/2020EA001248

Golombek M, Kass D, Williams N, Warner N, Daubar I, Piqueux S, Charalambous C, Pike WT (2020c) Assessment of InSight landing site predictions. J Geophys Res, Planets 125:e2020JE006502. https://doi.org/10.1029/2020JE006502

Golombek M, Charalambous C, Pike WT, Sullivan R (2020d) The origin of sand and dust on Mars: evidence from the InSight landing site. 51st lunar and planetary science, abstract #2744. Lunar Planet Inst, Houston

Golombek MP, Trussell A, Williams N, Charalambous C, Abarca H, Warner NH et al (2021) Rock size-frequency distributions at the InSight landing site, Mars. Earth Space Sci 8:e2021EA001959. https://doi.org/10.1029/2021EA001959

Grant JA, Warner NH, Weitz CM, Golombek MP, Wilson SA, Baker M et al (2020) Degradation of Homestead hollow at the InSight landing site based on the distribution and properties of local deposits. J Geophys Res, Planets 125:e2019JE006350. https://doi.org/10.1029/2019JE006350

Grant JA, Wilson SA, Golombek M, Trussell A, Warner NH, Williams N et al (2022) Degradation at the InSight landing site, Homestead hollow, Mars: constraints from rock heights and shapes. Earth Space Sci 9(2):e2021EA001953. https://doi.org/10.1029/2021EA001953

Greeley R (2002) Saltation impact as a means for raising dust on Mars. Planet Space Sci 50(2):151–155. https://doi.org/10.1016/S0032-0633(01)00127-1

Greeley R, Iversen JD (1985) Wind as a geological process on Earth, Mars, Venus and Titan, vol 4. Cambridge University Press, Cambridge

Greeley R, Iversen JD (1987) Measurements of wind friction speeds over lava surfaces and assessment of sediment transport. Geophys Res Lett 14(9):925–928. https://doi.org/10.1029/GL014i009p00925

Greeley R, Leach R, White B, Iversen J, Pollack J (1980) Threshold windspeeds for sand on Mars: wind tunnel simulations. Geophys Res Lett 7(2):121–124. https://doi.org/10.1029/GL007i002p00121

Greeley R, Balme MR, Iversen JD, Metzger S, Mickelson R, Phoreman J, White B (2003) Martian dust devils: laboratory simulations of particle threshold. J Geophys Res, Planets 108(E5):5041. https://doi.org/10.1029/2002JE001987

Greeley R, Whelley PL, Arvidson RE, Cabrol NA, Foley DJ, Franklin BJ, Geissler PG, Golombek MP, Kuzmin RO, Landis GA, Lemmon MT (2006) Active dust devils in Gusev crater, Mars: observations from the Mars Exploration Rover Spirit. J Geophys Res, Planets 111(E12):E12S09. https://doi.org/10.1029/2006JE002743

Grott M, Spohn T, Knollenberg J, Krause C, Hudson TL, Piqueux S et al (2021) Thermal conductivity of the Martian soil at the InSight landing site from HP^3 active heating experiments. J Geophys Res, Planets 126(7):e06861. https://doi.org/10.1029/2021JE006861

Hartman FR, Cooper B, Leger C, Maxwell S, Wright J, Yen J (2005) Data visualization for effective rover sequencing. In: 2005 IEEE international conference on systems, man and cybernetics, Waikoloa, HI, pp 1378–1383. https://doi.org/10.1109/ICSMC.2005.1571339

Hobiger M, Hallo M, Schmelzbach C, Stähler S, Fäh D, Giardini D et al (2021) The shallow structure of Mars from inversion of high-frequency ambient noise Rayleigh wave ellipticity at the InSight landing site. Nat Commun 12:6756. https://doi.org/10.1038/s41467-021-26957-7

Holstein-Rathlou C, Gunnlaugsson HP, Merrison JP, Bean KM, Cantor BA, Davis JA et al (2010) Winds at the Phoenix landing site. J Geophys Res 115:E00E18. https://doi.org/10.1029/2009JE003411

Imken T, Ali K, Bailey P, Mishra P, Penrod J, Sorice C, Sundgaard M, Williams M (2020) Preparation and execution of the InSight instrument deployment phase. In: Proceedings of the IEEE aerospace conference, March 7-14, 2020

InSight IDA Science Team (2019) Mars InSight Lander Instrument Deployment Arm (IDA) Data Archive. PDS Geosciences (GEO) Node. https://pds-geosciences.wustl.edu/missions/insight/ida.htm

Iversen JD, Greeley R, Pollack JB (1976) Windblown dust on Earth, Mars and Venus. J Atmos Sci 33(12):2425–2429. https://doi.org/10.1175/1520-0469(1976)033<2425:WDOEMA>2.0.CO;2

Johnson CL, Mittelholz A, Langlais B, Russell CT, Ansan V, Banfield D, Chi PJ, Fillingim MO, Forget F, Haviland HF, Golombek M (2020) Crustal and time-varying magnetic fields at the InSight landing site on Mars. Nat Geosci 13(3):199–204

Kim D, Davis P, Lekić V, Maguire R, Compaire N, Schimmel M, Stutzmann E, Irving JCE, Lognonné P, Scholz JR, Clinton J (2021) Potential pitfalls in the analysis and structural interpretation of seismic data from the Mars InSight mission. Bull Seismol Soc Am 111(6):2982–3002

Knapmeyer M, Stähler SC, Daubar I, Forget F, Spiga A et al (2021) Seasonal seismic activity on Mars. Earth Planet Sci Lett 576:117171. https://doi.org/10.1016/j.epsl.2021.117171

Knapmeyer-Endrun B, Panning MP, Bissig F, Joshi R, Khan A, Kim D, Lekić V, Tauzin B, Tharimena S, Plasman M, Compaire N (2021) Thickness and structure of the Martian crust from InSight seismic data. Science 373(6553):438–443

Krinsley D, Smalley I (1972) Sand. Am Sci 60:286–291
Kuenen PhH (1960) Sand. Sci Am 202(4):21–34
Langlais B, Thébault E, Houliez A, Purucker ME, Lillis RJ (2019) A new model of the crustal magnetic field of Mars using MGS and MAVEN. J Geophys Res, Planets 124(6):1542–1569
Lemmon MT, Wolff MJ, Smith MD, Clancy RT, Banfield D, Landis GA, Ghosh A, Smith PH, Spanovich N, Whitney B, Whelley P, Greeley R, Thompson S, Bell JF III, Squyres SW (2004) Atmospheric imaging results from the Mars Exploration Rovers: spirit and opportunity. Science 306:1753–1756. https://doi.org/10.1126/science.1104474
Lemmon MT, Wolff MJ, Bell JF III, Smith MD, Cantor B, Smith PH (2015) Dust aerosol, clouds, and the atmospheric optical depth record over 5 Mars years of the Mars Exploration Rover mission. Icarus 251:96–111. https://doi.org/10.1016/j.icarus.2014.03.029
Lemmon MT, Daubar IJ, Banks M, Vaubaillon J, Sansom E, Maki J (2020) The InSight Mars lander's meteor search. In: EPSC abstracts, p 14. EPSC2020-499
Lisano M, Bernard D (2014) An almanac of Martian dust storms for InSight project energy system design. In: Aerospace conference. https://doi.org/10.1109/AERO.2014.6836269. IEEE XPlore, 15 pp
Lognonné P, Gagnepain-Beyneix J, Banerdt WB, Cacho S, Karczewski JF, Morand M (1996) An ultra-broad band seismometer on InterMarsnet. Planet Space Sci 44:1237–1249. https://doi.org/10.1016/S0032-0633(96)00083-9
Lognonné P, Banerdt WB, Giardini D, Pike WT, Christensen U, Laudet P et al (2019) SEIS: insight's seismic experiment for internal structure of Mars. Space Sci Rev 215(1):12. https://doi.org/10.1007/s11214-018-0574-6
Lognonné P, Banerdt WB, Pike WT, Giardini D, Christensen U, Garcia RF et al (2020) Constraints on the shallow elastic and anelastic structure of Mars from InSight seismic data. Nat Geosci 13:213–220. https://doi.org/10.1038/s41561-020-0536-y
Lorenz RD, Reiss D (2015) Solar panel clearing events, dust devil tracks, and in-situ vortex detections on Mars. Icarus 248:162–164
Lorenz R, Lemmon M, Maki J (2021a) First Mars Year of Observations with the InSight Solar Arrays: winds, dust devil shadows, and dust accumulation. Icarus 364:114468. https://doi.org/10.1016/j.icarus.2021.114468
Lorenz R, Martínez GM, Spiga A, Vicente-Retortillo A, Newman CE, Murdoch N, Forget F, Millour E, Pierron T (2021b) Lander and rover histories of dust accumulation on and removal from solar arrays on Mars. Planet Space Sci 207:105337. https://doi.org/10.1016/j.pss.2021.105337
Maki JN, Lorre JJ, Smith PH, Brandt R, Steinwand DJ (1999) The color of Mars: spectrophotometric measurements at the Pathfinder landing site. J Geophys Res 104:8781–8794
Maki J, Thiessen D, Pourangi A, Kobzeff P, Litwin T, Scherr L, Elliott S, Dingizian A, Maimone M (2012) The Mars science laboratory engineering cameras. Space Sci Rev 170:77–93. https://doi.org/10.1007/s11214-012-9882-4
Maki JN, Golombek M, Deen R, Abarca H, Sorice C, Goodsall T et al (2018) The color cameras on the InSight lander. Space Sci Rev 214(105). https://doi.org/10.1007/s11214-018-0536-z
Maki J, Trebi-Ollennu A, Banerdt B, Sorice C, Bailey P, Khan O, Kim W, Ali K, Lim G, Deen R, Abarca H, Ruoff N, Hollins G, Andres P, Hall J, the InSight Operations Team (2019) Imaging from the InSight lander. In: Proceedings of 21st EGU general assembly, EGU2019, 01 January 2019
Maki JN, Golombek M, Banerdt W, Smrekar S, Deen R, Abarca H et al (2021) Color properties at the Mars InSight landing site. Earth Space Sci 8:e2020EA001336. https://doi.org/10.1029/2020EA001336
Maki J, Deen R, Abarca H, Zamani P (2022) InSight cameras data bundle. NASA planetary data system. https://doi.org/10.17189/1510484
Marteau E, Golombek M, Vrettos C, Garvin JB, Williams NR (2021) Soil mechanical properties at the InSight landing site, Mars. In: 52nd lunar and planetary science, abstract #2067. Lunar Planet Ins, Houston
Marteau E, Golombek M, Vrettos C, Delage P, Williams NR, Ansan V (2022) Soil strength properties derived from scraping and dumping activities at the InSight landing site on Mars. In: 53rd lunar and planetary science conference. abstract #1523
Marteau E, Golombek M, Delage P, Vrettos C, Hurst K, Gomez A, Williams NR, Bailey P, Mishra P (2023) Initial results from the Insight lander robotic arm soil mechanics experiments on Mars. 54th lunar and planetary science, abstract #1597. Lunar Planet Inst, Houston
McGlynn IO, Fedo CM, McSween HY Jr (2011) Origin of basaltic soils at Gusev crater, Mars, by aeolian modification of impact-generated sediment. J Geophys Res 116:E00F22. https://doi.org/10.1029/2010JE003712
McGlynn IO, Fedo CM, McSween HY Jr (2012) Soil mineralogy at the Mars Exploration Rover landing sites: an assessment of the competing roles of physical sorting and chemical weathering. J Geophys Res 117:E01006. https://doi.org/10.1029/2011JE003861

Minitti ME, Kah LC, Yingst RA, Edgett KS, Anderson RC, Beegle LW et al (2013) MAHLI at the Rocknest sand shadow: science and science-enabling activities. J Geophys Res, Planets 118:2338–2360. https://doi.org/10.1002/2013JE004426

Mittelholz A, Johnson CL (2022) The Martian crustal magnetic field. Front Astron Space Sci 9:895362. https://doi.org/10.3389/fspas.2022.895362

Mittelholz A, Johnson CL, Morschhauser A (2018) A new magnetic field activity proxy for Mars from MAVEN data. Geophys Res Lett 45:5899–5907. https://doi.org/10.1029/2018GL078425

Mittelholz A, Johnson CL, Feinberg JM, Langlais B, Phillips RJ (2020) Timing of the Martian dynamo: new constraints for a core field 4.5 and 3.7 Ga ago. Sci Adv 6(18):eaba0513

Moore HJ, Hutton RE, Clow GD, Spitzer CR (1987) Physical properties of the surface materials of the Viking landing sites on Mars. US Geol Surv Prof Pap 1389:222pp., 2plates

Mueller N, Piqueux S, Lemmon M, Maki J, Lorenz RD, Grott M et al (2021) Near surface properties of Martian regolith derived from InSight HP^3-RAD temperature observations during Phobos transits. Geophys Res Lett 48:e2021GL093542. https://doi.org/10.1029/2021GL093542

Murdoch N, Mimoun D, Garcia RF, Rapin W, Kawamura T, Lognonné P (2017a) Evaluating the wind-induced mechanical noise on the InSight seismometers. Space Sci Rev 211:419–455. https://doi.org/10.1007/s11214-016-0311-y

Murdoch N, Kenda B, Kawamura T, Spiga A, Lognonné P, Mimoun D, Banerdt WB (2017b) Estimations of the seismic pressure noise on Mars determined from Large Eddy Simulations and demonstration of pressure decorrelation techniques for the InSight mission. Space Sci Rev 211:457–483. https://doi.org/10.1007/s11214-017-0343-y

Olson E (2011) AprilTag: a robust and flexible visual fiducial system. https://april.eecs.umich.edu/media/pdfs/olson2011tags.pdf

Pan L, Ehlmann BL, Carter J, Ernst CM (2017) The stratigraphy and history of Mars' northern lowlands through mineralogy of impact craters: a comprehensive survey: stratigraphy of Mars' Northern Lowlands. J Geophys Res, Planets 122(9):1824–1854

Pan L, Quantin-Nataf Q, Tauzin B, Michaut C, Golombek MP, Lognonne P et al (2020) Crust stratigraphy and heterogeneities of the first kilometers at the dichotomy boundary in Western Elysium Planitia and implications for InSight lander. Icarus 338:113511. https://doi.org/10.1016/j.icarus.2019.113511

Pavlis T, Mason K (2017) The new world of 3D geologic mapping. GSA Today 27:4–10. https://doi.org/10.1130/GSATG313A.1. Also see https://www.geosociety.org/gsatoday/science/G313A/GSATG313A.pdf

Perrin C, Rodriguez S, Jacob A, Lucas A, Spiga A, Kawamura T, Murdoch N, Pan L, Lorenz R, Daubar IJ, Lognonne P, Banfield D, Banks ME, Garcia RF, Newman C, Ohja L, Widmer-Schnidrig R, Banerdt WB (2020) Monitoring of dust devil tracks around the InSight landing site, Mars, and comparison with in-situ atmospheric data. Geophys Res Lett 47:e2020GL087234. https://doi.org/10.1029/2020GL087234

Peters GH, Abbey W, Bearman GH, Mungas GS, Smith JA, Anderson RC, Douglas S, Beegle LW (2008) Mojave Mars simulant—characterization of a new geologic Mars analog. Icarus 197:470–479. https://doi.org/10.1016/j.icarus.2008.05.004

Piqueux S, Müller N, Grott M, Siegler M, Millour E, Forget F et al (2021) Soil thermophysical properties near the InSight lander derived from 50 sols of radiometer measurements. J Geophys Res, Planets 126:e2021JE006859. https://doi.org/10.1029/2021JE006859

Pleskot LK, Miner ED (1981) Time variability of Martian bolometric albedo. Icarus 45(1):179–201. https://doi.org/10.1016/0019-1035(81)90013-0

Reiss D, Lorenz R (2016) Dust devil track survey at Elysium Planitia, Mars: implications for the InSight landing sites. Icarus 266:315–330

Ruff S, Christensen PR (2002) Bright and dark regions on Mars: particle size and mineralogical characteristics based on Thermal Emission Spectrometer data. J Geophys Res 107(E12):5127. https://doi.org/10.1029/2001JE001580

Scholz J-R, Widmer-Schnidrig R, Davis P, Lognonné P, Pinot B, Garcia RF, Hurst K, Pou L, Nimmo F, Barkaoui S et al (2020) Detection, analysis, and removal of glitches from InSight's seismic data from Mars. Earth Space Sci 7(11):e2020EA001317

Sorice C, Bailey P, Trebi-Ollennu A, Kim WS, Myint S (2020) Catenary model of InSight SEIS tether for instrument deployment. In: 2020 IEEE aerospace conference, pp 1–8. https://doi.org/10.1109/AERO47225.2020.9172783

Sorice C, Ali K, Trebi-Ollennu A, Mishra P, Lim G, Bailey P, Hudson TL, Marteau E, Kim J (2021) InSight robotic arm testing activities for HP3 mole anomaly recovery on Mars. In: IEEE aerospace conference, 06 March 2021

Spiga A, Murdoch N, Lorenz R, Forget F, Newman C, Rodriguez S et al (2021) A study of daytime convective vortices and turbulence in the Martian planetary boundary layer based on half-a-year of InSight atmospheric measurements and large-eddy simulations. J Geophys Res, Planets 126:e2020JE006511. https://doi.org/10.1029/2020JE006511

Spohn T, Grott M, Smrekar SE, Knollenberg J, Hudson TL, Mueller N et al (2018) The heat flow and physical properties package (HP3) for the InSight mission. Space Sci Rev 214(5):96. https://doi.org/10.1007/s11214-018-0531-4

Spohn T, Hudson TL, Witte L, Wippermann T, Wisniewski L, Kedziora B, Vrettos C, Lorenz RD, Golombek M, Lichtenheldt R, Grott M, Knollenberg J, Krause C, Fantinati C, Nagihara S, Grygorczuk J (2022a) The InSight-HP^3 mole on Mars: lessons learned from attempts to penetrate to depth in the Martian soil. Adv Space Res 69:3140–3163. https://doi.org/10.1016/j.asr.2022.02.009

Spohn T, Hudson TL, Marteau E, Golombek M, Wippermann T, Ali KS, Schmelzbach C, Kedar S, Hurst K, Trebi-Ollennu A et al (2022b) The HP^3 penetrator (mole) on Mars: Soil properties derived from the penetration attempts and related activities. Space Sci Rev 218(72). https://doi.org/10.1007/s11214-022-00941-z

Stamnes K, Tsay S-C, Wiscombe W, Jayaweera K (1988) Numerically stable algorithm for discrete-ordinate-method radiative transfer in multiple scattering and emitting layered media. Appl Opt 27:2502–2509. https://doi.org/10.1364/AO.27.002502

Stella PM, Herman JA (2010) The Mars surface and solar array performance. In: 35th IEEE photovoltaic specialists conference, Honolulu, 20–25 June 2010, pp 002631–002635. https://doi.org/10.1109/PVSC.2010.5617185

Sullivan R, Banfield D, Bell JF III, Calvin W, Fike D, Golombek M et al (2005) Aeolian processes at the Mars Exploration Rover Meridiani Planum landing site. Nature 436:58–61. https://doi.org/10.1038/nature03641

Sullivan R, Arvidson R, Bell JF III, Gellert R, Golombek M, Greeley R et al (2008) Wind-driven particle mobility on Mars: insights from MER observations at "El Dorado" and surroundings at Gusev crater. J Geophys Res 113:E06S07. https://doi.org/10.1029/2008JE003101

Sweeney J, Warner NH, Ganti V, Golombek MP, Lamb MP, Fergason R, Kirk R (2018) Degradation of 100-m-scale impact craters at the InSight landing site on Mars with implications for surface processes and erosion rates in the Hesperian and Amazonian. J Geophys Res, Planets 123:2732–2759. https://doi.org/10.1029/2018JE005618

Terzaghi K (1943) Theoretical soil mechanics. Wiley, New York

Trebi-Ollennu A, Kim W, Ali K, Khan O, Sorice C, Bailey P et al (2018) InSight Mars lander robotics instrument deployment system. Space Sci Rev 214:93. https://doi.org/10.1007/s11214-018-0520-7

Trebi-Ollennu A, Kim W, Ali K, Khan O, Sorice C, Bailey P et al (2020) Robotics instrument deployment system surface operations for the InSight Mars lander. In: Proceedings of the SpaceOps 2020 Conference, 01 May 2020

Verdier N, Ansan V, Delage P et al (2023) Using wind dispersion effects during the InSight tether burial activities to better constrain the regolith grain size distribution. J Geophys Res, Planets, in press

Vicente-Retortillo A, Martínez GM, Renno N, Newman CE et al (2018) Seasonal deposition and lifting of dust on Mars as observed by the Curiosity Rover. Sci Rep 8:17576. https://doi.org/10.1038/s41598-018-35946-8

Viúdez-Moreiras D, Newman CE, Forget F, Lemmon M, Banfield D, Spiga A, Lepinette A, Rodriguez-Manfredi JA, Gomez-Elvira J, Pla-Garcia J, Muller N, Grott M (the TWINS/InSight team) (2020) Effects of a large dust storm in the near-surface atmosphere as measured by InSight in Elysium Planitia, Mars. J Geophys Res 125:e2020JE006493. https://doi.org/10.1029/2020JE006493

Volk MW, Fu RR, Mittelholz A, Day JM (2021) Paleointensity and rock magnetism of Martian nakhlite meteorite Miller range 03346: evidence for intense small-scale crustal magnetization on Mars. J Geophys Res, Planets 126(5):e2021JE006856

Warner NH, Golombek MP, Sweeney J, Fergason R, Kirk R, Schwartz C (2017) Near surface stratigraphy and regolith production in southwestern Elysium Planitia, Mars: implications for Hesperian-Amazonian terrains and the InSight lander mission. Space Sci Rev 211(1):147–190

Warner NH, Grant JA, Wilson SA, Golombek MP, DeMott A, Charalambous C et al (2020) An impact crater origin for the InSight landing site at Homestead hollow, Mars: implications for near surface stratigraphy, surface processes, and erosion rates. J Geophys Res, Planets 125(4):e2019JE006333. https://doi.org/10.1029/2019JE006333

Warner NH, Golombek MP, Ansan V, Marteau E, Williams N, Grant JA et al (2022) In situ and orbital stratigraphic characterization of the InSight landing site—a type example of a regolith-covered lava plain on Mars. J Geophys Res, Planets 127(4):e2022JE007232

Weitz CM, Sullivan RJ, Lapotre MGA, Rowland SK, Grant JA, Baker M, Yingst RA (2018) Sand grain sizes and shapes in eolian bedforms at Gale crater, Mars. Geophys Res Lett 45:9471–9479. https://doi.org/10.1029/2018GL078972

Weitz CM, Grant JA, Golombek MP, Warner NH, Hauber E, Ansan V et al (2020) Comparison of InSight Homestead hollow to hollows at the Spirit landing site. J Geophys Res, Planets 125(7):e2020JE006435

Wippermann T, Hudson TL, Spohn T, Witte L, Scharringhausen M, Tsakyridis G, Fittock M, Krömer O, Hense S, Grott M, Knollenberg J, Lichtenheldt R (2020) Penetration and performance testing of the HP^3 Mole for the InSight Mars mission. Planet Space Sci 181:104780. https://doi.org/10.1016/j.pss.2019.104780

Wolfe CA (2016) Using engineering cameras on Mars rovers and landers to retrieve atmospheric dust loading. Master's thesis, Texas a & M University. Available electronically from http://oaktrust.library.tamu.edu/handle/1969.1/158130

Yen AS et al (2005) An integrated view of the chemistry and mineralogy of Martian soils. Nature 436:49–54. https://doi.org/10.1038/nature03637

Authors and Affiliations

M. Golombek[1] · T. Hudson[1] · P. Bailey[1] · N. Balabanska[1] · E. Marteau[1] · C. Charalambous[2] · M. Baker[3] · M. Lemmon[4] · B. White[5] · R.D. Lorenz[6] · T. Spohn[7,8] · J. Maki[1] · P. Kallemeyn[5] · J.B. Garvin[9] · C. Newman[10] · K. Hurst[1] · N. Murdoch[11] · N. Williams[1] · W.B. Banerdt[1] · P. Lognonné[12] · P. Delage[13] · R. Lapeyre[14] · E. Gaudin[14] · C. Yana[14] · N. Verdier[14] · M. Panning[1] · A. Trebi-Ollennu[1] · K. Ali[1] · A. Mittelholz[15] · C. Johnson[16,17] · B. Langlais[18] · N. Warner[19] · J. Grant[3] · I.J. Daubar[20] · V. Ansan[18] · C. Vrettos[21] · A. Spiga[22] · D. Banfield[23] · A. Gomez[24] · P. Mishra[1] · R. Dotson[25] · C. Krause[26] · G. Sainton[11] · T. Gabsi[11]

✉ M. Golombek

1 Jet Propulsion Laboratory, California Institute of Technology, Pasadena, CA, USA

2 Imperial College, London, UK

3 National Air and Space Museum, Smithsonian Institution, CEPS, Washington, DC, USA

4 Space Science Institute, Boulder, CO, USA

5 Lockheed Martin Space Systems Company, Littleton CO, USA

6 Johns Hopkins Applied Physics Laboratory, Laurel, MD, USA

7 International Space Science Institute, Bern, Switzerland

8 German Aerospace Center (DLR), Institute of Planetary Research, Berlin, Germany

9 NASA Goddard Space Flight Center, 8800 Greenbelt Road, Greenbelt, MD, USA

10 Aeolis Research, Chandler, AZ, USA

11 Institut Supérieur de l'Aéronautique et de l'Espace (ISAE-SUPAERO), Université de Toulouse, Toulouse, France

12 Institut de Physique du Globe de Paris-Sorbonne Paris Cité, Université Paris Cité, Paris, France

13 Ecole des Ponts Paris Tech, Laboratoire Navier/CERMES, CNRS, Marne la Vallée, France

14 Centre National d'Études Spatiales, Toulouse, France

15 Department of Earth and Planetary Sciences, Harvard University, Cambridge, MA, USA

16 Department of Earth, Ocean and Atmospheric Sciences, The University of British Columbia, Vancouver, Canada

17 Planetary Science Institute, Tucson, AZ, USA

18 CNRS, UMR 6112, Laboratoire de Planétologie et Géosciences, Nantes Université, Nantes, France

19 Department of Geological Sciences, SUNY Geneseo, 1 College Circle, Geneseo, NY, USA

20 Earth, Environmental, and Planetary Sciences, Brown University, Providence, RI, USA

21 Technical University of Kaiserslautern, Kaiserslautern, Germany

22 Laboratoire de Météorologie Dynamique/Institut Pierre-Simon Laplace (LMD/IPSL), Centre National de la Recherche Scientifique (CNRS), Sorbonne Université, Paris, France

23 NASA Ames Research Center, Moffett Field, CA USA

24 California Institute of Technology, Pasadena, CA, USA

25 Quantaero, 1 E. Liberty St., Ste 600, Reno, NV, USA

26 German Aerospace Center (DLR), Microgravity User Support Center (MUSC), Cologne, Germany